UNIVERSITÀ DI PARMA

UNIVERSITA' DEGLI STUDI DI PARMA

DOTTORATO DI RICERCA IN SCIENZE E TECNOLOGIE DEI MATERIALI

CICLO XXXIV

3D Electron Diffraction of Complex Functional Materials

Coordinatore:
Prof. Enrico Dalcanale

Tutore:
Dr. Mauro Gemmi
Prof.ssa Lara Righi

Dottorando: Andrea Griesi

Anni Accademici 2019/2022

Contents

1. *Introduction*

The enduring challenge in modern materials science is to disclose the relationship between materials structure and properties. The design of materials with improved efficiency in exploiting the intrinsic properties is one of the most important purposes of a new generation of smart materials. Multiferroic compounds, perovskites with giant magnetoresistance effect, magnetoelectric materials, ionic conductors and magnetic hybrid organic-inorganic porous frameworks are often characterized by the mutual interactions of physical and chemical properties. Hence, the structural characterization, being physical and chemical properties intrinsically related to the crystal structure, represents a fundamental aspect in this scenario. However, these kinds of materials are often characterized by complex structures. The development of innovative tools for the structural investigation of materials is continuously growing and new diffraction techniques have been implemented in the last decades. In this context the novel approach based on the collection of 3D electron diffraction (ED) data is revolutionizing the structural analysis of nanocrystalline and complex materials. The classical structural information retrieved from a transmission electron microscope (TEM) was essentially two-dimensional, with data derived by zone axis diffraction patterns. The recent development of novel technique and protocols[1,2] of data collection implemented on a conventional TEM allows to convert the instrument as a single-crystal diffractometer. The principal limitations in the application of ED for the crystal structure determination are derived by strong dynamical effects that suppress the relations between structure factors and reflections intensity in the reciprocal space.

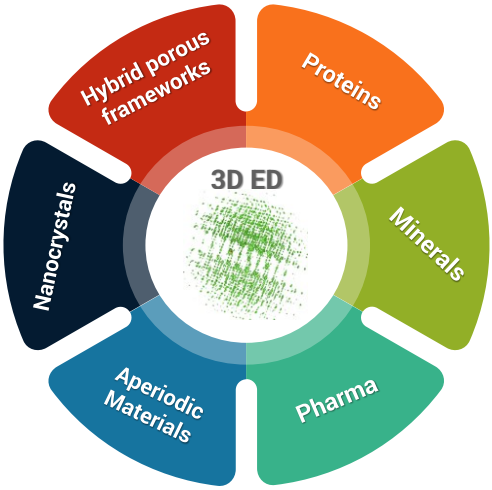

Figure 1: *Scheme resuming the representative structures solved by 3D-ED method in several classes of materials reported in literature.*

This fundamental drawback was tackled by introducing two experimental solutions represented by the precession of primary electron beam[3] and the reciprocal space collection through the automated sequence of non-oriented patterns, i.e. electron diffraction tomography (ADT)[4]. The combined use of these two techniques provides quasi-kinematical ED intensities that were adopted to solve crystal structures in several fields. In Figure 1 it is schematically indicated the different materials whose crystal structures was successfully solved by the application of the 3D ED analysis specially in absence of single crystals suitable for the classical X-ray diffractometry. In this rapidly evolving context, the main purpose of this thesis is represented by the study of the fundamental concepts supporting the electron crystallography and by the application of this novel structural analysis to study complex crystals structure featuring different types of materials. In Chapter 1 the physical theory of this new diffraction technique is explained. The exposure of the physical characteristics of this technique starts from the fundamental principles of diffraction that are common to all diffraction techniques, to then evaluate the differences between the diverse techniques and expose the benefits of 3D ED. In Chapters 2, 3 and 5 are also exposed the technological evolutions and the different techniques developed in the last

decade that have made electron diffraction reliable and applicable in the field of materials science and explains in detail how structural information is extracted from a standard 3D ED data collection.
In Chapter 4 and 6 practical examples of the application of 3D ED on latest generation materials are exposed. The fourth chapter is dedicated to the resolution and refinement of doubly ordered perovskite structures showing incommensurate structural modulation; the modulated structure of these phases have been solved for the first time with the application of superspace approach on 3D-ED sets. In the sixth chapter, we pursuit the structural analysis of some magnetic MOFs in which two different metal cations are present. In this section, the synthesis methods, the structural and magnetic analysis are exposed. In both case studies, it is shown that the conceptual and technological developments of 3D ED have made this diffraction technique a stunning structural analysis of new generation materials.

References

1. Gemmi M. *et al.* 3D electron diffraction: The nanocrystallography revolution. *ACS Central Science* vol. 5 1315–1329 (2019).
2. Palatinus, L. *et al.* Specifics of the data processing of precession electron diffraction tomography data and their implementation in the program PETS2.0. *Acta Crystallographica Section B: Structural Science, Crystal Engineering and Materials* **75**, 512–522 (2019).
3. Vincent, R. *et al.* Double conical beam-rocking system for measurement of integrated electron diffraction intensities. *Ultramicroscopy* **53**, 271–282 (1994).
4. Kolb, U. *et al.* Towards automated diffraction tomography: Part I-Data acquisition. *Ultramicroscopy* **107**, 507–513 (2007).

1. Electron Crystallography

1.1 Basic Crystallography

The diffraction techniques allow to identify the atomic arrangement inside a crystal and allows to establish the physical properties of the material both of an inorganic and organic nature. In this thesis we determine the crystalline structures of different materials using crystallographic methods with different sources (X-ray, electron, and neutrons) that have common principles. The common physical principle is the interference of scattering waves usually known as diffraction. Diffraction is an interference phenomenon that arises when a series of scattering objects are placed at distanced of the order of the wavelength of the scattered radiation. In the case of crystals, the scattering objects are the atoms, and the distances involved are the interatomic distances which are of the order of 0.1 nm (1Å). For this reason, if we want to exploit an electromatic wave as scattering radiation we should use x-ray. Alternatively, electrons and neutrons with a proper kinetic energy can have associated De Broglie wave lengths shorth enough to produce diffraction phenomena by interacting with the atoms of a crystal. X-ray, electron and neutron diffraction are then the election methods to investigate the crystal structure.

1.1.1 Bragg's law

Without entering in the details on the interaction mechanism between the atoms and one of these “radiation” types we can say that once a X-ray, electron or neutron wave (remember in that case with wave we mean the electromagnetic wave or the quantum mechanical wave in case of the particles) interacts with atoms, each of those becomes a source of a spherical wave of the same radiation. All these waves interfere with each other giving rise to the diffraction phenomenon. If the material crossed by the radiation is a crystal its atoms form a regular and periodic arrangement in three dimensions. The location of the scattering centers (atoms) in a lattice produces a very peculiar diffraction in which the scattered radiation interferes in a destructive way almost everywhere except along some specific directions

arranged in a regular way. The crystal becomes a three-dimensional diffraction grating for the incoming radiation. W.H. Bragg and W.L. Bragg gave the first phenomenological explanation to X-ray diffraction in 1913 during their X-ray scattering studies[1] . They considered the crystals as made by atoms located at the vertex of a three-dimensional lattice and proposed that the lattice planes formed by those atoms can reflect as mirrors the incoming radiation. If the radiation impinges a set of parallel planes with an angle that assure a constructive interference between the radiation reflected by adjacent planes, a diffraction maximum is observed in the direction corresponding to the reflected radiation. Since the difference in the path between reflected rays of adjacent planes is $2d \sin\theta$ (see fig.1) where d is the interplanar distance between the atomic planes inside the crystal and θ is the angle between the incident rays and the plane normal, the condition of diffraction becomes:

$$2d \sin\theta = n\lambda$$

where λ is the wavelength and n is a positive integer. This law works perfectly fine and explains the entire geometry of diffraction. However, the reflective nature of the lattice plane is an indirect effect of the scattering nature of the atoms. The very same formula can be derived by considering the interference of the radiation scattered by all the atoms inside the unit cell.

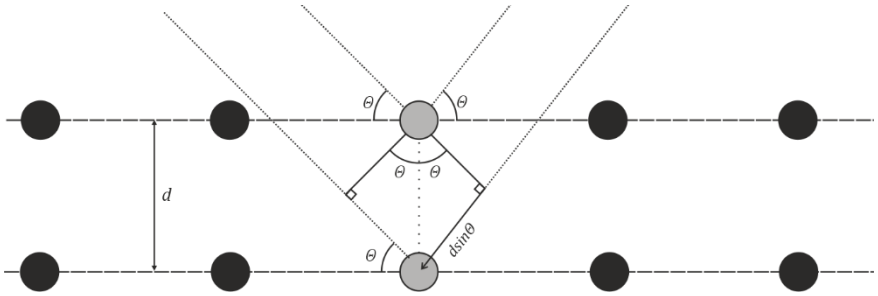

Fig.1: Diagram of the Bragg's law. Spheres indicate atoms in two atomic planes with a distance d. Dotted lines show two waves with the same wavelength and with the same angle of incidence.

To demonstrate this, is assumed a kinematic approach in which the incident waves produce secondary waves for each volume of crystal affected by the radiation, with an intensity proportional to the scattering power $S(r)$ of the

elements within the volume. The $S(r)$ of a crystal depends on the incident radiation: in case of electrons it is the electrostatic potential φ(r), for the X-Ray the electron density $\varrho(r)$ and for the neutrons it depends on the "nuclear density" $\delta(r)$. Therefore, the scattering power of an infinitesimal volume dv_r of a crystal is proportional to $S(\vec{r})dv_r$ where $\vec{r}$ represents the scattering vector of the volume, defined in figure 2:

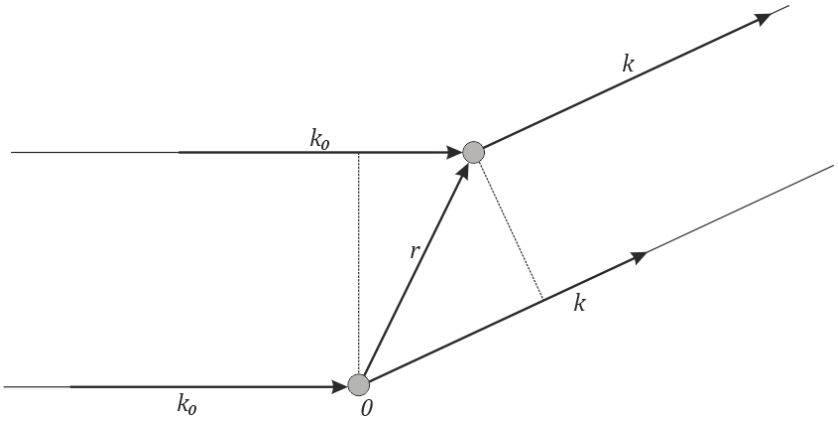

Fig.2: The origin of the difference of the phase on the direction k, from two different dv_r.

If we consider an infinitesimal volume dv_r at the position r of a crystal hit by an incident wave $\exp(i\vec{k}_0 \cdot \vec{r})$ (defined with the Euler formalism) with a wave vector $\left|\overrightarrow{k_0}\right| = 2\pi/\lambda$ it will produce secondary waves $S(\vec{r})\exp(i\vec{k} \cdot \vec{r})dv_r$ with the same wavelength ($\left|\vec{k}\right| = \left|\vec{k}_0\right|$). The phase shift between the secondary waves produced by this volume and by an analogous volume located in the origin is related to the directions of the exiting wave vectors $\vec{k}$ and is equal to $\left(\vec{k} - \vec{k}_0\right) \cdot \vec{r}$. This can be easily demonstrated by calculating the path difference between the incoming and the exiting waves, as can be seen from Figure 2.

To calculate the total scattering amplitude exiting from the crystal, it is necessary to sum all the infinitesimal scattered waves $S(\vec{r})\exp(i\vec{k} \cdot \vec{r})dv_r$ over the entire crystal volume (integration). Substituting $\vec{k} - \overrightarrow{k_0} = \vec{s}$ the total integral is:

$$f(\vec{s}) = K \int \varphi(\vec{r}) \exp(i\vec{s} \cdot \vec{r})\, dv_r \quad (1)$$

where K is a proportionality factor and depends on the nature of the radiation, which will be omitted later for simplicity, and we have inserted the electrostatic potential as scattering power since we deals with electrons. This integral can be used for a distribution of atoms or molecules and for any source using the correct scattering factor. Interestingly, from the mathematical expression (1) it can be seen that the total scattering amplitude is the Fourier transform of the scattering power calculated in $\vec{s} = \vec{k} - \vec{k}_0$,

$$F\{\varphi(\vec{r})\} = f(\vec{s}) \quad (2)$$

where $\vec{s}$ which is usually known as the scattering wave vector.

1.1.2 Diffraction of a Crystal

A crystal is a periodic distribution of matter along the three dimensions, therefore the crystal electrostatic potential is a periodic function in three dimensions. The Fourier theory says that an integral of the type (1), requires that the values of the function $f(s)$ become discrete. In one dimension, a function $\varphi(x)$ periodic with period a is described by a series of Fourier coefficients Φ_h (amplitude of the structure) calculated as:

$$\Phi_h = \frac{1}{a}\int_0^a \varphi(x)\, exp\left\{i\left(\frac{2\pi h}{a}\right)x\right\} dx \quad (3)$$

with h getting only integer values. The magnitude $2\pi h\ /\ a$ in the previous equation corresponds to the value of $\vec{s}$ defined for equation (1).

For a periodic function with a period a, the values of $f(\vec{s})$ other than zero occur only for values of $s\ =\ 2\pi h\ /\ a$, and spaced with a distance of $2\pi h\ /\ a$, therefore:

$$f(\vec{s}) \sim \Phi_h = \Phi(2\pi h/a)$$

Passing in three dimensions the period a is substituted by a minimal volume repeated periodically in space called unit cell. This volume is a parallelogram

delimited by 3 basis vectors usually called $\vec{a}$, $\vec{b}$ and $\vec{c}$, which forms that basis vectors of the crystal lattice. In three dimensions the Fourier coefficients become:

$$\Phi_{hkl} = \frac{1}{a \cdot b \cdot c} \int_0^a \int_0^b \int_0^c \varphi(xyz)\, exp\{2\pi i(hx/a + hy/b + hz/c)\}\, dx\, dy\, dz$$
$$= 1/\Omega \int \varphi(r) \exp(2\pi i r \cdot H)\, dv_r \quad (4)$$

Where h, k and l are integers, and $2\pi h/a$, $2\pi k/b$ and $2\pi l/c$ are the components of the vector $\vec{s}$ along the three main directions of periodicity in 3D Fourier space related to the unit cell basis vectors. Therefore, the scattering amplitude is different from zero only for those values of the vector $\vec{s}$ in which h, k, l are integers and therefore there exists a distribution of points in which the scattering amplitude Φ_{hkl} is different from zero, this distribution is periodic in Fourier space and constitutes the so-called reciprocal lattice (figure 3), since it is the reciprocal of the crystal lattice. The Fourier space is usually called reciprocal space.

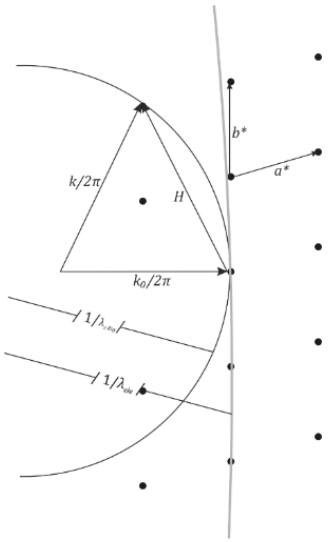

Fig.3: In gray the Ewald sphere electronic, in black the Ewald sphere of X-Ray and the points are the reciprocal space where $\Phi_{hkl} \neq 0$

1.1.3 Reciprocal Space and Ewald Sphere

In order to understand the geometry of the reciprocal lattice we rewrite eq. (4) as:

$$\Phi_{hkl} = \frac{1}{a \cdot b \cdot c} \int_0^a \int_0^b \int_0^c \varphi(xyz)\, exp\{2\pi i(hx/a + hy/b + hz/c)\}\, dx\, dy\, dz$$

$$= 1/\Omega \int \varphi(r) \exp(2\pi i r \cdot H)\, dv_r)$$

$$= \iiint_0^1 \varphi(r)\, exp\big(2\pi i\, (xa + yb + zc) \cdot (ha^* + kb^* + lc^*)\big)\, d_x d_y d_z \quad (5)$$

where the integration is now carried out on the unit cell, $\vec{r}$ is expressed in terms of coordinates relative to the unit cell basis vectors ($\vec{a}$, $\vec{b}$ and $\vec{c}$) and the scattering vector is now expressed as an integer linear combination of three new basis vectors which are the reciprocal lattice base: $\vec{a}^*, \vec{b}^*$and $\vec{c}^*$. The eq. (6) defines $\vec{a}^*, \vec{b}^*$and $\vec{c}^*$, this new basis vectors $\vec{a}^*, \vec{b}^*$and $\vec{c}^*$ must satisfy the following relation:

$$\vec{a}^* \cdot \vec{a} = 1, \qquad \vec{a}^* \cdot \vec{b} = 0, \qquad \vec{a}^* \cdot \vec{c} = 0$$

$$\vec{b}^* \cdot \vec{a} = 0, \qquad \vec{b}^* \cdot \vec{b} = 1, \qquad \vec{b}^* \cdot \vec{c} = 0$$

$$\vec{c}^* \cdot \vec{a} = 0, \qquad \vec{c}^* \cdot \vec{b} = 0, \qquad \vec{c}^* \cdot \vec{c} = 1$$

which is the defining relation of the reciprocal basis vectors. In the reciprocal space each point hkl (Formalism of Miller) of reciprocal lattice is defined by a vector:

$$\frac{\vec{s}}{2\pi} = \vec{H} = h\vec{a}^* + k\vec{b}^* + l\vec{c}^* \quad (6)$$

That in our new formalism is a reciprocal lattice vector. So, the conditions for having diffraction from a crystal become:

$$\vec{k} = \overrightarrow{k_0} + \vec{s} = \overrightarrow{k_0} + 2\pi\vec{H} \quad (7) \quad \vec{s} = 2\pi\vec{H}$$

These relations define the directions of the beams diffracted by the crystal, which are produced when there is an intersection between the points of the reciprocal lattice and the Ewald sphere. Given a certain incoming radiation beam defined by $\vec{k}_0$ and a certain crystal orientation, defined by the corresponding relative orientation of the reciprocal lattice with respect to $\vec{k}_0$, any scattered radiation can be represented by a vector $\vec{k}$ that will lay on a sphere of radius k_0(known as Ewald sphere). If we identify the origin of the reciprocal lattice with the tip of $\vec{k}_0$, which will lay on the Ewald sphere surface, eq. (5) and (6) tell us that only when a reciprocal lattice node is on the Ewald sphere, the corresponding $\vec{k}$ scattered radiation give raise to constructive interference and a diffraction spot is visible (see figure 3). Changing the direction of the vector $\vec{k}_0$ (changing the angle of incidence of the ray or the position of the crystal) changes the orientation of the sphere with respect of the reciprocal lattice and the reciprocal lattice nodes that lay on the sphere. Therefore, as expected this will change the visible diffracted beams. The size of the Ewald sphere is related to the wavelength of the source used (λ)

$$R_{ewald} = \left|\vec{k}\right| = \left|\vec{k}_0\right| = 2\pi/\lambda$$

The wavelength of the X-rays is about $\lambda_X \sim 1$ Å comparable to the size of the unit cells which are in the order of $5 - 10$ Å, therefore the sphere has a great curvature with respect to the planes of the reciprocal lattice, this implies that an X-ray diffraction on a static crystal will only measure a few reflections at the same time. The accelerated electrons have a much smaller wavelength in the order of $\lambda_e = 0.01$ Å and therefore the electronic Ewald sphere has a very large radius and is almost flat compared to the reciprocal lattice planes. Therefore, in electron diffraction is common to have several diffraction spots simultaneously excited and in certain geometrical configurations (zone axis condition) an entire reciprocal lattice plane can be observed (figure 3).

The exponent of equation (5) $(hx/a + hy/b + hz/c)$, is the expanded form of the scalar product between the vector $\vec{r}$ and the vector $\vec{H}$ (5), where the vector $\vec{r}$ indicates an exact position of a point $\vec{r}(x, y, z)$ inside the unit cell.

If $\vec{r}$ is equal to an axial vector $\vec{a}$, $\vec{b}$ or $\vec{c}$ the vector H in the reciprocal space is:

$$\vec{H}_{hkl} \cdot \frac{\vec{a}}{h} = 1, \qquad \vec{H}_{hkl} \cdot \frac{\vec{b}}{k} = 1, \qquad \vec{H}_{hkl} \cdot \frac{\vec{c}}{l} = 1 \quad (8)$$

these conditions are also known as the "three Laue conditions".

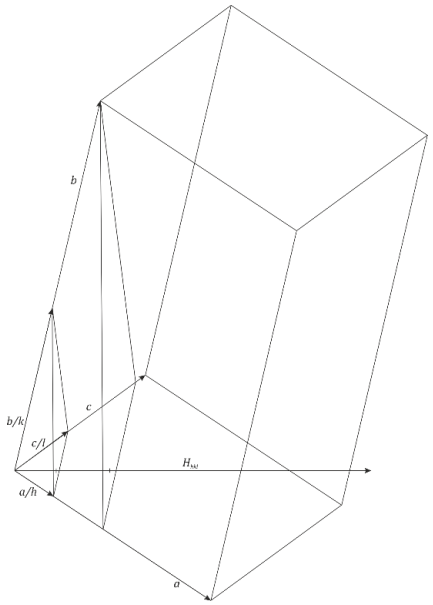

Fig. 4: Relation between the reciprocal lattice and vector H_{hkl}, the axial vectors a,b,c of the unit cell.

If subtract the relations (8) in pairs obtain scalar products of the type:

$$\left(\vec{a}/h - \vec{b}/k\right) \cdot \vec{H}_{hkl} = 0$$

So $\vec{H}$ is perpendicular to the vectors that form the sides of the triangle (fig. 4) that are in the plane (hkl). The distance between the origin of the coordinates and this plane or with respect to another adjacent plane is the interplanar distance d_{hkl}. From formulas (6) or directly analyzing figure 4 it can be deduced that to have a diffraction from a crystal the condition must be satisfied:

$$\frac{\sin\theta}{\lambda} = \frac{\vec{H}}{2} = \frac{1}{2d}$$

Then Brag's law was derived by considering the interference of the radiation diffused by all the atoms inside the unit cell.

1.1.4 Structure Amplitude and the Fourier Series

In the previous chapters it has been shown that the scattering amplitude by a crystal is different from zero only at the points of the reciprocal lattice. How much it differs from zero is determined by equation (4), which however differs dimensionally from the Fourier integral due to the presence of Ω, to avoid this difference, in structural analyzes formula (4) is used without the denominator, which represents the volume of the cell, therefore:

$$\Phi_{hkl} = \Phi_H = \int_{\Omega} \varphi\,(\vec{r}) \exp\left(2\pi i \vec{r} \cdot \vec{H}\right) dv_r \quad (8)$$

In general, the electrostatic potential $\varphi(\vec{r})$ can be found using the inversion theorem (explained with formulas (1) and (2)) once the set of amplitudes Φ_H are known. The amplitudes are discrete quantities since $\varphi(\vec{r})$ is periodic, and therefore the inversion operation does not produce an integral but a Fourier series:

$$\varphi(\vec{r}) = \sum_{H} \Phi_H \exp\,(-2\pi i \vec{r} \cdot \vec{H})$$

The modulus of $|\Phi_H|$ is found experimentally from the square root of the diffraction intensities, and once it phases are known we can obtain the distribution of $\varphi(\vec{r})$, which is related to the distribution of matter that will scatter inside the unit cell. The scattering capacity $\varphi(\vec{r})$, has the maximum values in the positions of the atoms, so the peaks in a map as in figure 5 correspond to the single scattering atoms. Starting from the maxima and their shape, the interatomic distances inside the cell are determined.

1.1.5 Atomic Amplitude

The equation that defines the scattering amplitude $f(\vec{s})$ (1), describes the diffusion of a single atom, through the atomic potential $\varphi(\vec{r})$ which is usually approximated to a spherical symmetric function. Therefore, $\varphi(\vec{r})$ depends exclusively on the scalar r and not on the vector $\vec{r}$ and therefore the atomic amplitude f in the reciprocal space is real and depends only on the modulus of $|\vec{s}| = s$, these considerations allow a simplification of equation (1):

$$f(s) = \int_0^\infty \varphi(r) 4\pi r^3 \left\{\frac{(sinsr)}{sr}\right\} dr \quad (9)$$

Thus, it has been shown that it is possible to calculate the scattering by a unit cell of a crystal starting from the atomic amplitudes and the distribution of the atoms. The total $\varphi(r)$ can be obtained by superimposing all the atomic $\varphi_i(\vec{r})$ of the atoms inside the unit cell defined through the vectors $\vec{r_i}$:

$$\varphi(\vec{r}) = \sum_i \varphi_i(\vec{r} - \vec{r_i}) \quad (10)$$

Therefore, the Fourier integral over the entire cell, i.e. the amplitude of the structure calculated with equation 8, can be calculated as the sum of the phase factor exp $(2\pi i r_i \cdot H)$ of each atom which takes into account the position r_i of the i-th atom with respect to the origin of the coordinates multiplied by the corresponding atomic scattering amplitude $f_i(\vec{s})$:

$$\Phi_H = \int \sum_i \varphi_i(r - r_i) \exp(2\pi i r \cdot H)\, dv_r = [\dots]$$
$$= \sum_i f_i \exp(2\pi i r_i \cdot H) \quad (11)$$

1.1.6 Real Crystal

The scattering produced by a crystal, which is an infinite three-dimensional periodic distribution of matter, produces an amplitude $f(\vec{s})$ which is different from zero in a set of discrete points of the reciprocal lattice, each with a module expressed by the Φ_H. The structure amplitude Φ_H is known as structure factor. This representation of the scattering is a simplified model, in fact a real crystal has finite dimensions with a finite number of elementary cells, therefore, strictly speaking, is not an infinite three-dimensional periodic object. To describe a real crystal, it is necessary to insert the form factor[2] $S(\vec{r})$, which describes a limited solid body, by assuming a value of zero outside the crystal and a unity value inside the crystal. Then by calculating the Fourier transform of the periodic distribution $\varphi(\vec{r})$ multiplied by the form factor $S(\vec{s})$ we will obtain the scatterig amplitude for a real crystal:

$$\Phi_{cry} = F\{\varphi(\vec{r})S(\vec{s})\} = \int \varphi(\vec{r})S(\vec{r}) \exp(i\vec{s} \cdot \vec{r})\, dv_r = f(\vec{s}) * D(\vec{s}) \quad (11)$$

where * indicates the convolution and $D(\vec{s})$ is the Fourier transformed of the form factor, known also as "shape transform" or "crystalline form factor". It is estimated that $D(\vec{s})$ is a "point" only for large crystals (crystals with a size of 1 μm are already considered infinite).

The convolution operation states that the amplitude Φ_H is spread around the corresponding reciprocal lattice node by the shape transform $(\vec{s})$. Since in case of electrons the crystals that we observe are thin, especially in the direction crossed by the beam, the resulting $D(\vec{s})$ is elongated in the same direction. This causes that we can have diffraction also if the Ewald sphere is close to a reciprocal lattice node, not only when it touches it.

In conclusion, if we deal with a real crystal the electron diffraction intensities will be proportional to the square modulus of the diffracted amplitude. In case of a certain reflection h, this intensity is:

$$I_h(\vec{s}) = \left|\Phi_{cry}\right|^2 = |\Phi_H D(\vec{s})|^2$$

where is the distance in reciprocal space from the exact Bragg condition also known as excitation error. Unfortunately, this formula is just an approximation, since it relies on the assumption that the probability of multiple scattering is negligible (kinematical scattering). For real crystals used in diffraction experiment, this is true only for X-ray and neutron scattering, while for electrons crystals of several tens of nanometers exhibits already a measurable multiple scattering (dynamical effects). The equation states that, even if we neglect the dynamic effects and are close to the Bragg condition, there is a diffuse intensity that can be different from the square modulus of the structure factor.

1.1.7 Electron vs. X-ray and Neutrons

The biggest difference of diverse technique are the interaction between matter and the incident beam. If we compare the ratio of intensity between the incident ray J_0 on the sample and the diffracted ray J among the three techniques, and if we consider equal to one the ratio between the incident ray and the diffracted ray in the case of electrons, we obtain that:

$$\frac{J_0^{ele}}{J} = 1,\ \frac{J_0^{X-Ray}}{J} = -10^{-3},\ \frac{J_0^{Neutro}}{J} = -10^{-4}$$

This difference exists because incoming radiations interact with matter in different ways: electrons interact with electrostatic potential $\varphi(\vec{r})$, X-rays with electron density $\varrho(\vec{r})$ and neutrons with "nuclear density" $\delta(\vec{r})$. From

the numbers it is clear that electrons interact with matter much stronger that X-ray and neutrons. This has two main consequences:

1) X-ray diffraction and neutron diffraction in order to have a signal intensity comparable to the intensity of electron diffraction require a larger amount of sample, which means either larger crystals to exploit single crystal diffraction or powder diffraction if the crystals are small (<1micron). Instead, electron diffraction is able to measure a diffraction signal on single crystals with a size in the order of hundreds of nanometers or even less. This is also possible because the electron beam can be easily focused on small volume by magnetic lenses because the electrons are charged particles. Thanks to this ability to produce an intense diffraction signal on small volumes, electron diffraction has been used in this thesis on doubly ordered perovskite, and on metal-organic framework, to investigate the modulation the presence of guest inside the channels.

2) The stronger interaction between matter and electrons causes dynamic effects, beacause electrons scatter several time inside the same crystal. Each scattered electron can act as a new "primary beam" and be scattered again, causing multiple diffraction, these problems cause a distribution of intensities completely altered and making them very similar (figure 5). Therefore, the cinematic theory valid for X-ray does not fully explain the electronic diffraction in the case of strong dynamic effect, and the use of electron diffraction for solving crystal structures became problematic.

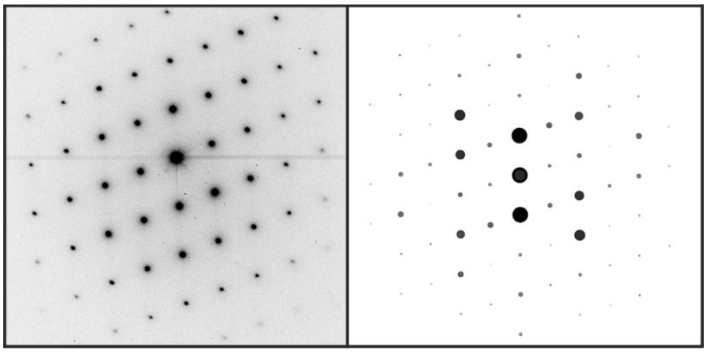

Fig.5: Experimental pattern of electron diffraction on left same pattern calculated with the kinematic approximation on the right.

2.2 3D Electron Diffraction Methods

2.2.1 Drawbacks of 3D-ED

From the previous paragraph electron diffraction has a series of problems that limit the ability to solve crystal structures using ED data. The main drawbacks that have to be faced to use electron diffraction as a routinary structure solution technique are:

- Excitation error: the reflection conditions in the reciprocal space have a non-negligible volume and if they are measured not exactly under the Bragg conditions there is a great underestimation of the intensity due to the shape transform function.

- Dynamical Scattering: which prevents applying the kinematic approximation on ED data. This effect implies the violation of the linear relationship between the reflection intensity and the square modulus of the structure factor.

- Coverage: with common transmission electron microscopes it is not always possible to collect enough diffraction data to solve a structure due to hardware limitation.

- Beam damage: some samples, especially of organic or semi-organic, undergo decomposition or amorphization due to the high energy to which they are subjected by the electron beam.

The excitation error is correlated to the non-zero dimensions of the reflections conditions in the reciprocal space due to the size of the diffraction area and to the mosaicity of the crystals. If we consider a crystal as a platelet of thickness t, the shape transform results in a sinc function so within the kinematic approximation the intensity of the reflection can be calculated as:

$$J(\vec{r}) \sim \left|\Phi_{cry}(\vec{H})\right|^2 \left[\frac{sin^2(\pi t s_h)}{s_h^2}\right]$$

Where $s_h = \vec{r} - \vec{H}$ is the excitation error, defined as the distance between the point of the reciprocal lattice g and a point on the Ewald sphere.

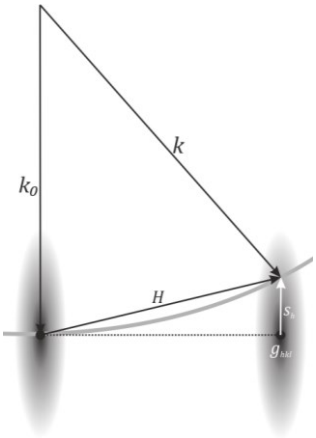

Fig. 6: Scheme of the excitation error on a point g_{hkl} of the reciprocal space. The color density indicates the decrease in diffraction intensity measured as s_h increases due to the shape transform.

When the Bragg condition is satisfied, the value of s_h is zero, if the excitation occurs outside the Ewald sphere, s_h is positive, while if it occurs inside the Ewald sphere, the value of s_h is negative.

As can be seen from the graph (figure 8), if the $sinc^2$ function is plotted for different thicknesses, it is possible to estimate the real dimension of the reflection in the reciprocal space and how the intensity decreases as s_h increases. To have an estimate of the effect of the excitation error on the amplitude of the structure factor, it is necessary to calculate how far from a perfect Bragg condition the intensity drops by 50%.

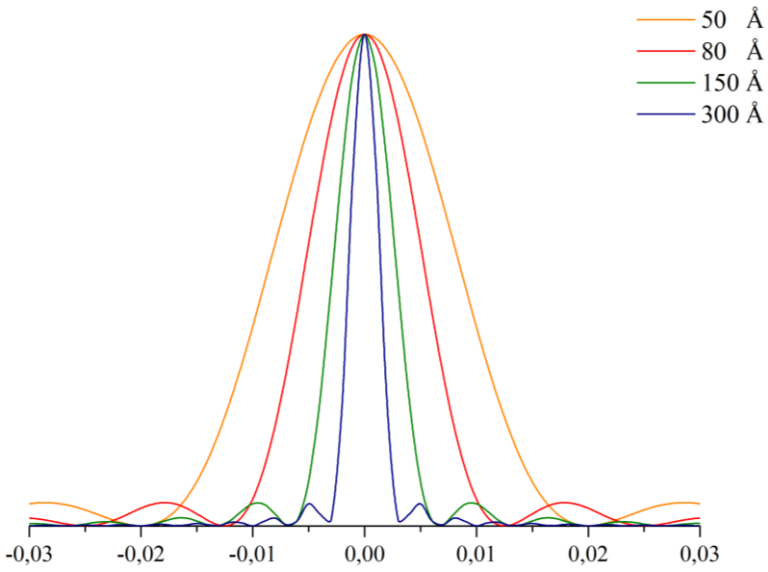

Fig. 7: Plot of the function $sinc^2$. *For* 4 *different thicknesses of* 50 Å, 100 Å, 200 Å *and* 500 Å. S_h *is in* $Å^{-1}$ *unit.*

For example, for a thickness of $t = 200$ Å, an ideal thickness for electron diffraction, the amplitude of the structure factor drops by 50% for a $s_h = 0.0022$ Å, and the same error occurs for an inclination inaccuracy of 0.35° respect to the perfect Bragg condition for a reflection corresponding to a periodicity of 3 Å. The inclination which produces the same error on the amplitude of the structure factor decrease with the resolution of the reflection and increase with the thickness of the crystal. Hence, estimating the amplitude of the structure factor from individual patterns is very difficult, because a difference of even a fraction of a degree between the expected orientation causes completely different diffraction intensities. This problem is absent in X-ray and Neutron diffraction because excitation errors are empirically corrected using different functions to fit and integrate the profile, instead of summing the partial intensity measurements. At the beginning, the technique of electron crystallography consisted in the acquisition of diffraction patterns along the zone axes of the crystal[3] (Figure 8).

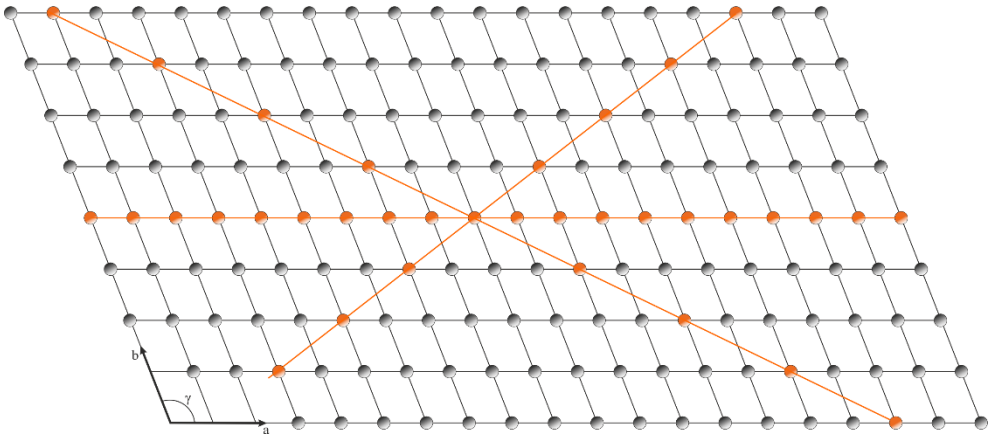

Fig. 8: Scheme of the ED data collection made along single zone axes. The nodes of reciprocal space in black and the direction of the Ewald sphere in orange.

A 3D data set of intensities formed by merging the intensities measured in different zones are of scarce quality, because the single zone axis patterns are affected by all the problems mentioned above. Since along the zone axes there are numerous reflections that are close to Bragg the possibility of multiple scattering is increased, making more problem. Moreover, small inaccuracies on the orientation of the crystal produce large deviations on the estimate of $|\Phi_H|^2$ even if the dynamic scattering is negligible. Last but not least, it is extremely time consuming to have a complete data set in this way, since it requires a relevant number of zone axes. The development of the electron diffraction technique in the last decade has focused on solving the problems discussed above. The various developments of the technique have been oriented towards:

- Collect the electron diffraction away from the zone axes.
- Maximize the sampling of the reciprocal space and thus solve the excitation error.
- Minimize the dynamical scattering.

2.2.2 Precession Electron Diffraction – PED

A great development has been obtained with the invention of the precession electron diffraction (PED)[4,5], which was invented to reduce dynamic scattering, but which also solved the excitation error problem. PED was initially implemented on ED zone axis patterns. The pattern is collected usually in SAED (selected area diffraction) mode with the parallel incident electron beam precessing around the optical axis on a cone surface which has the vertex fixed on the sample plane. To avoid the beam movement on the diffraction plane (all the spots would become circles) the precession movement is compensated after the sample by a descan system of lenses. In the resulting PED pattern, each diffracting reflection is integrated over a set of diffracting conditions corresponding to the precession movement of the Ewald sphere. In case of a zone axis pattern, this diffraction geometry assures that at every instant, during the precession movement, fewer reflections are simultaneously excited, thus reducing a dynamical effects. At the same time, the Ewald sphere movement guarantees that each reflection is integrated over a certain excitation error, reducing the problem of the reflection spreading in the reciprocal space due to the crystal shape. This second effect acts independently if the pattern is in zone axis or not. Interestingly zone axis PED intensities are so close to the kinematical approximation that they are reliable in the definition of the symmetry of the crystal, because the systematic absences characteristic of translational symmetry element are respected.

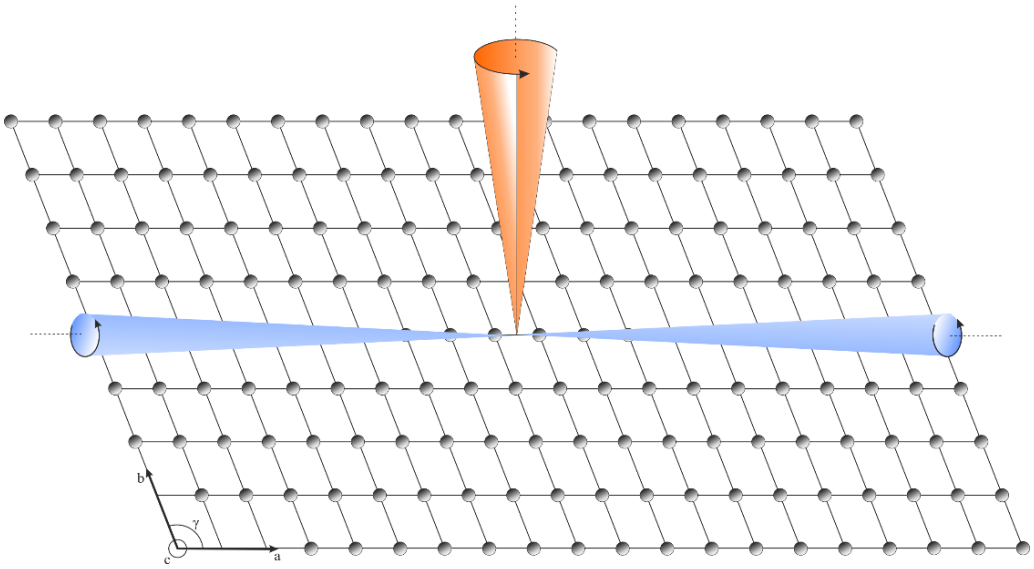

Fig. 9: Scheme of the precession motion of the incident ray in orange with consequent conical motion of the Ewald sphere in the crystalline plane in blue.

In order to use a set of PED zone axis patterns to solve a crystal structure, the reflections intensities should be merged into a 3D date set[6]. This step is on one hand critical because the residual dynamical effect can make the determination of the scaling difficult, on the other end a lot of patterns must be collected to have an acceptable reciprocal space coverage. Unfortunately, orienting the crystal in a large number of zone axes is a long and difficult job that requires an experienced microscopist. Furthermore, to merge the data collected on different crystals it is often necessary to suite a sufficient reciprocal space coverage, thus further complicating the merging procedure. Beside some remarkable success [7–13], these difficulties prevented the zone axis PED from becoming a routine crystallographic technique for structure solution.

2.2.3 Automatic Diffraction Tomography – ADT

The simplest solution to the problem of a limited reciprocal space coverage is to collect a sequence of diffraction patterns by tilting the sample around the axis of goniometer of the TEM: the same data collection procedure employed in single crystal x-ray diffraction with area detector. The first application of this method was carried out in 2007[14] and was called by their inventors automatic diffraction tomography (ADT) (figure 11). This data collection method guarantees the maximum coverage of the reciprocal space which is limited only by the space between the objective pole pieces of the TEM (so by the microscope model) and by type of sample holder. Generally, the maximum angular range varies between 60° and 120°.

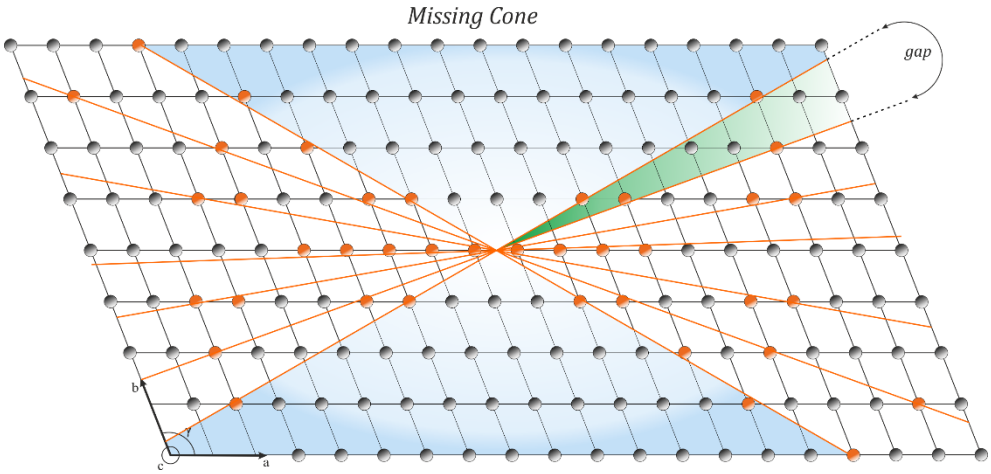

Fig. 10: Scheme of the ADT data collection; the gap in green is the reciprocal space non-integrated between two patterns; the part of reciprocal space non-integrated called the missing cone is indicate in blue.

The advantage of this technique is that the collection of most of the patterns occurs along a random direction of the crystal and usually away from the main zone axis. These conditions guarantee a minimization of dynamic scattering. The central problem of this method concerns the tracking of the crystal position: in fact in most microscopes there is a movement of the crystal during the rotation of the goniometer (especially for long rotation of several degrees like in this case), even if the eucentric height has been defined with great

accuracy. To solve this problem, the rotation was originally carried out in steps of 1° and the position of the crystal was checked after each rotation of the goniometer and the crystal was re-centered under the electron beam. Even with this expedient, the collection of diffraction data remains very simple and can be successfully carried out even by a standard TEM user in a much shorter time than the crystal orientation of several zone axes. The sequence of patterns collected with this method must necessarily be analyzed through specific software, designed for ED data, so as to be able to carry out the three-dimensional reconstruction of the reciprocal space and the data reduction method. Ad hoc software for ED data are ADT3D[15], PETS[16], EDTProcess[17] and RED[18]. Others have been developed starting from software to manage X-ray data: DIALS[19] MOSFLM[20] and XDS[21]. With a sequence of diffraction patterns collected at each degree and a correct software, it is possible to obtain the parameters of the unit cell and the extinction rules[22], but the crystalline structure can rarely be found[23,24] because the problem of excitation error. In fact, if the data are collected in steps, there is a portion of non-integrated reciprocal space between a diffraction pattern along one direction and the next (the gap, indicated in green in Figure 11). This unintegrated reciprocal space causes an underestimation of the intensities on all reflections and makes it difficult to find the crystal structure from these diffraction data.

2.2.4 Precession-assisted electron diffraction tomography – PEDT

A possible solution to the excitation error problem for the ADT technique was proposed for the first time in 2009[25] and is based on the union of the ADT technique with the PED technique. In this technique, the diffraction patterns are collected exactly as in the ADT (off-zone) technique but with the beam in precession mode in a sort of "precession-assisted electron diffraction tomography" (PEDT)[26]. The diffraction patterns are usually collected with a 1 degree step (as in ADT), with a precession half angle comparable to this angular step. In this way, the Ewald sphere sweeps in the reciprocal space and integrates the missing wedge between one pattern and the next solving the excitation error problem (figure 11).

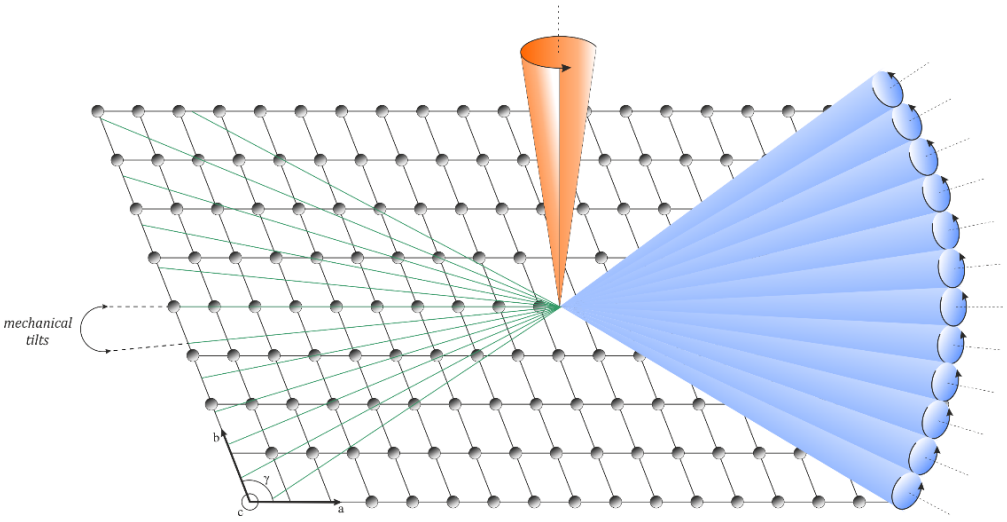

Fig.11: Scheme of the PEDT collection: the precession motion of the incident electron beam is displayed in orange, while the consequent conical motion of the Ewald sphere in the crystalline plane is depicted in blue for each tilt step of the goniometer.

The intensities recorded in this way have a great coverage of the reciprocal space and their intensities is correctly integrated over the excitation error. Thanks to this and to the peculiar geometry of off zones patterns, the PEDT intensities are very close to a kinematical approximation[26], therefore they can be successfully used in the *ab initio* structures solution, using methods such

as direct methods or charge flipping[16]. Furthermore, these data can be modeled considering the residual dynamic effects and the structure can be refined with a precision still not comparable to single crystal X-ray data but vary close, and it is possible to define and refine the positions of light atoms such as hydrogen[27].

2.2.5 Rotation Electron Diffraction – RED

An alternative to the PEDT technique, which also solves the problem related to the excitation error, is the rotation electron diffraction (RED), proposed for the first time by Zhang et al. in 2010[28]. This technique consists in sampling the reciprocal space very closely using very small angular steps, without the assistance of precession. This method only requires software that synchronizes the beam tilt with the hardware of the TEM and of the detector. This synchronization is necessary because for a correct sampling of the reciprocal space it is necessary an angular step less than 0.1° which is well beyond the mechanical precision of TEM goniometers. Such small angular tilts can be implemented only through the inclination of the electron beam induced by the microscope lenses. Therefore, to have the entire angular range of the goniometer covered, the data collection is a combination of mechanical steps of 1° or 3° and an small electrical tilt of the electron beam figure 12.

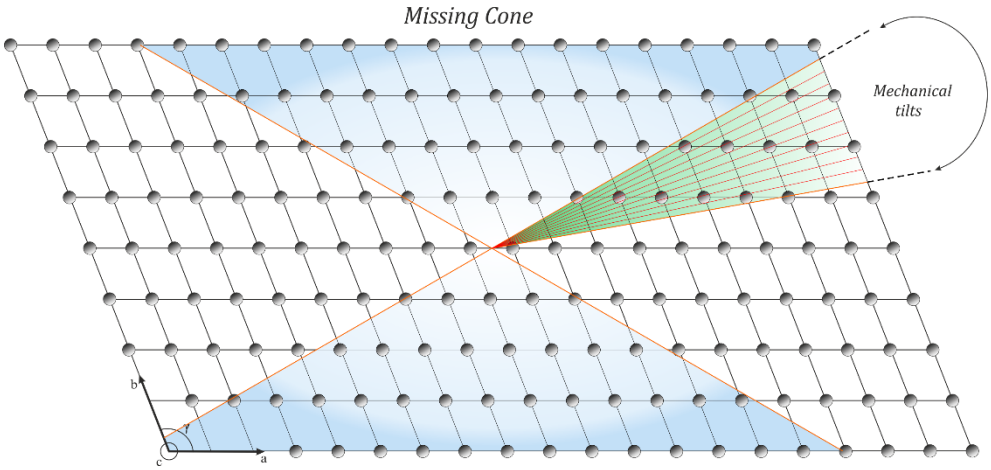

Fig.12: RED method scheme, the electric tilts in red.

The total angular interval sampled by the inclination of the beam is slightly greater than the angle covered by the mechanical movement of the goniometer to avoid any missing area. During the electrical tilt of the beam, since there are no mechanical movements of the holder, it is not necessary to re-center the crystal if the microscope lenses are properly aligned. A data collection in RED is made up of about 1000 patterns vs. the 100 of the PEDT. Since the geometry is the same as in PEDT and the reciprocal space is correctly sampled in RED, the kinematic approximation is also valid and the intensities collected can be used for structure solution with direct methods and for structural refinement[29]. The advent on the scene of RED and PEDT completely changed the scenario in electron crystallography. Both techniques allowed to solve crystalline structures of different nature such as: inorganic crystal (with PEDT[30] or RED[31,32]) mesoporous materials (with PEDT[33,34] or RED[35]), metal-organic frameworks (with PEDT[36]), covalent organic frameworks (with RED[37,38]), modulated structure (with PEDT[16]), new minerals (with PEDT[39–43]), organic crystals (with PEDT[44]) and biominerals (with PEDT[45]).

2.2.6 Centering Methods and Illumination Conditions

There are two types of illumination that can be used during diffraction collection with PEDT and RED techniques: selected area electron diffraction (SAED) mode and nano-diffraction mode. In SAED mode the area from ED is selected by putting a diaphragm in the image plane and the movement of the crystal during the rotation of the goniometer can be controlled by switching between diffraction mode and the image mode. If the crystal movement is large, it can be necessary to remove the SAED aperture to find the crystal position[16,18,40]. SAED mode is the simplest mode to implement in a standard TEM, however the illuminated area is larger than the area over which the diffraction is measured, therefore in case of beam-sensitive samples, the beam damage goes beyond the area visible through the aperture. Another drawback is the spherical aberration of the objective lens used, which affects the image and the location of the crystal. This error becomes significant for small SAED diaphragms and limits their use in the case of

small areas. In nano-diffraction, on the other hand, the diffraction area is selected by illuminating the sample with a parallel beam with a dimension between 50 and 200 nm. Only the selected area is illuminated and so damaged by the beam and there is no error induced by the spherical aberration. With such a small beam it is very difficult to center the crystal in standard "TEM imaging" mode, so two alternatives are followed. The first is to defocus the ED pattern until the crystal image is visible within the central diffraction spot[18]. The second is to use the electron microscope in STEM (scanning transmission electron microscopy) mode to view the position of the crystal after each rotation step[14]. This modality can be implemented without modifying the optical configuration of the TEM, creating a blurred image with the parallel nanobeam or with a converging beam (standard STEM mode)[46]. Imaging in STEM mode strongly reduces the total dose compared to TEM mode imaging since only one scan is enough to locate the crystal position. After this scan the image is frozen, and the beam is blanked and the operator can select the area of the crystal where to collect the diffraction on the “frozen image”, so that specimen is not exposed to the beam before the next pattern recording. The efficacy of the STEM modality on ray-sensitive samples is confirmed by the structural determination of a new polymorph of the lysozyme by PEDT[47].

2.2.7 The challenge of automating 3D-ED

PEDT and RED techniques made it possible to use ED data to solve crystal structures. The most critical aspect of both techniques is the difficulty of keeping the crystal under the electron beam during rotation, and, for beam sensitive samples, the extra dose necessary for the re-centering procedures. To avoid these drawbacks, the continuous rotation collection method is used. This method is very simple, but its effectiveness completely relies on the mechanical stability of the goniometer. Generally, the sample stages of the TEM do not have this stability and the crystal can move a lot during the rotation, so that it is possible to collect continuous rotation diffraction data only for limited angular intervals. According to the model of the microscope and the type of sample holder and goniometer, angular intervals of a few tens

of degrees up to 120 or more can be covered. With continuous rotation, the excitation error problem is solved by sampling the reciprocal space during the exposure time (t_{exp}) while the sample is rotating. The data set of this technique is therefore formed by a sequence of patterns which are the integration of the reciprocal space over an angle of $\eta_{exp} = \omega \cdot t_{exp}$ (where ω is the angular speed of the goniometer). For this technique it is vital that the readout time (t_{dead}) of the detector is minimal, so that the missing wedge between the pattern, equal to $\eta_{dead} = \omega \cdot t_{dead}$ is negligible. Luckily, the t_{dead} value is practically negligible in modern revelators, but this technique can also be used with slow detectors such as old CCD, provided they work in binned mode [48].

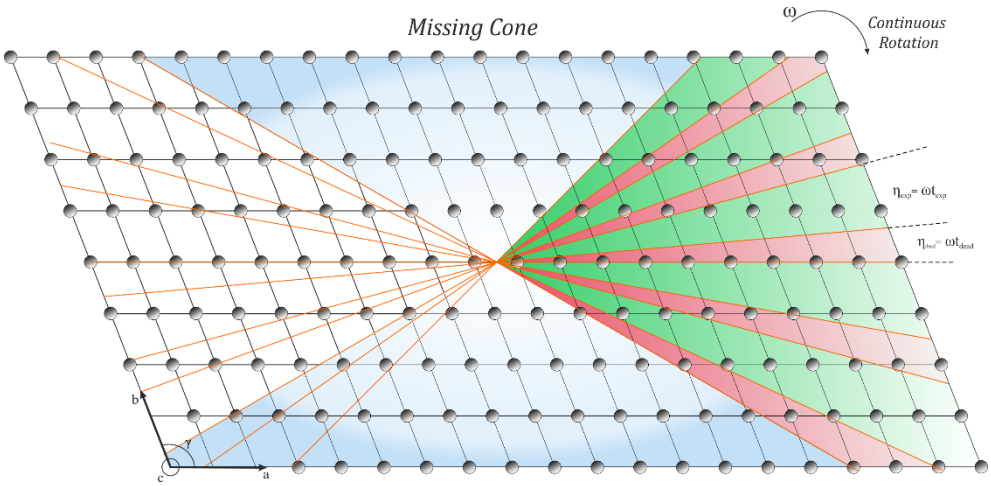

Fig. 13: Scheme of the continuous data collection. In green the sectors of the reciprocal space integrated during the period of exposure to the detector (η_{exp}). The sectors in red are the sectors lost during the detector readout time (η_{dead}).

This data collection method was first applied in 2013 on protein crystals[49] and is called with different acronyms: MicroED[50], IEDT[48] and cRED[51]. The invention of continuous data collection method has been a second huge development for 3D ED, because it made it possible to solve crystal structures of very beam sensitive samples that have an intrinsic nanocrystalline nature, such as zeolites[52], pharmaceutical products[53], organic[54] and proteins[55,56].

2.2.8 Future Developments

All the different methods of electron diffraction data collection demonstrate that 3D ED is a mature technique to be used for the structure solution of micro and nanocrystalline samples. As explained above the different techniques can be implemented on any transmission electron microscope. The points to be optimized to build a TEM specifically designed for 3D ED would be the stability of the goniometer and specific low-energy procedures for searching the sample on the grid. The goniometer of any future electron diffractometer should be able to reduce the movement of the crystal to a few hundred nanometers during the rotation phase and its movement must be synchronized with the exposure time of the detector. The illumination system must be able to create nanobeams of variable size (from $10\,nm$ to $\sim 100\,nm$) and of variable intensity with doses down to $0.01\,el\,s^{-1}A^{-2}$. Possibly, the crystal search phase must be carried out in STEM mode, but the STEM detector also needs development to allow the imaging phase e performed even with weak beams, so as to reduce the dose during the search phase. An electron diffractometer with these characteristics and equipped with a single electron detector would be used on samples of different nature, ranging from inorganic to macromolecules. Waiting for this technical development, 3D ED has allowed the study of crystallography at the nanoscale. We expect in the future that it will have more and more impact where crystallization is a difficult, as crystals that are invisible in optical microscopes can be analyzed as single crystals with the 3D ED technique. The fields that will have the most advantages in the development of this technique will be the chemistry of materials, macromolecular chemistry and pharmaceutical chemistry. Furthermore, 3D ED will allow to study the nucleation and growth of a crystal with structural details at atomic resolution at the different stages of growth.

2.3 Processing of 3D-ED Data

In this chapter are explained the necessary steps in the treatment of 3D-ED data collected with one of the previous methods. The 3D ED data are very similar to the data collected with a single crystal X-ray diffractometer but have some peculiar characteristics that require specific data reduction software. While a single zone axis pattern is informative per se, a 3D ED data collection needs to be treated with a data reduction software to extract any basic structural information such as the unit cell parameters or the crystal symmetry. This is carried out from a three-dimensional reconstruction of the reciprocal space from which to derive the indexing of each collected electron diffraction spot. For the treatment of 3D ED data in the years various software have been developed starting from software created for X-ray diffraction. One of the first software was ADT3D[22] then RED[18] and Pets[57] followed. Recently, the data collection format of 3D ED was adapted to work with X-ray diffraction software such as DIALS[19] and XDS[21]. The program used for the treatment of the PEDT diffraction data collected during this thesis was PETS 2.0, which allows, among other, to optimize the orientation of each diffraction pattern with respect to the incident beam. Below are shown all the steps that in PETS2.0 led to the extraction of intensities starting from raw diffraction patterns.

2.3.1 Peak Hunting

Once the collected patterns have been put in the right order, the diffraction pattern are read by PETS2.0, which first search for the local maxima. The criterion of identification of a maximum is through a I/sigma threshold, where sigma is estimated through a background estimation. If the intensity of the detected maximum is higher than the number of sigma given by the user, the peak is retained, otherwise it is rejected.

Fig. 14: Different values for $I/I(\sigma)$: higher (left) lower (right). With the lowest value it is possible to consider the intensities of the satellites in the case of modulated crystals.

The $I/I(\sigma)$ value that the user defines for peak choice is generally between 5 and 10, but it can be tuned to different values depending on the data quality. For example, if the diffraction intensities are very weak, it must be reduced to have enough peaks to identify the unit cell. If diffuse scattering is present, to avoid the detection of wrong peaks, it should be increased instead.

2.3.2 Refinement of the Rotation Axis

In this step, the position of the rotation axis of the crystal is refined, which can differ greatly from one data set to another, because it depends on the microscope settings. This step is performed because finding the right rotation axis allows the software to correctly orient each pattern so as to be able to perform the 3D reconstruction of the reciprocal space. The procedure that Pets 2.0 performs is similar to the procedure followed by Kolb[58] et al. This step is also necessary because a misaligned inclination axis causes a distortion of the diffraction volume, and can lead to an error up to the impossibility of defining the correct unit cell, and consequently an incorrect indexing of the reflections and their integration. To refine the axis, the software calculates the difference vector space for all the diffraction spots. These difference vectors are sorted along their directions in 3D space and plotted on a sphere, but for convenience the sphere is projected onto a plane with angular coordinates with the angular range of $\theta = 0^{\circ} - 180^{\circ}$ and $\varphi = 0^{\circ} - 360^{\circ}$ Figure 15.

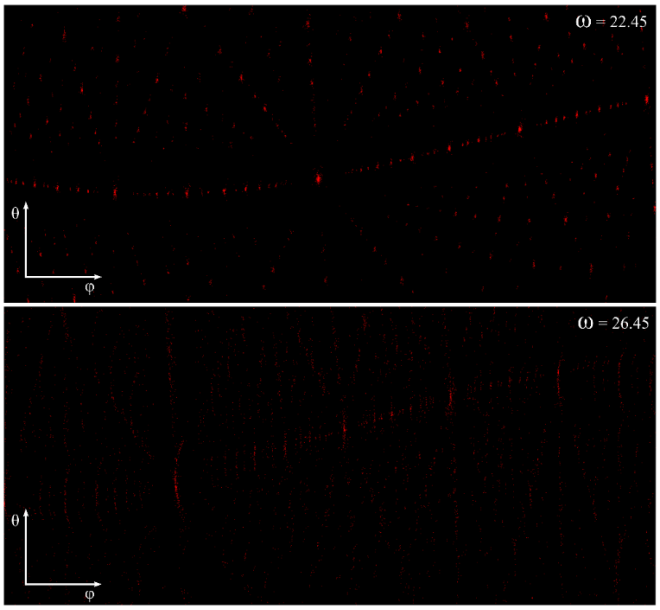

Fig. 15: Projections of the sphere of the difference vector space along the plane respect the angular coordinates[58]. At the top the projections with the rotation axis refined from the software at the bottom with a misaligned tilt axis of 4°.

To evaluate if the refinement of the inclination axis is correct, the criterion of "sharpness" is used, that is the variance of the map. This procedure finds the correct position of the ab initio axis for all data sets, with an accuracy of up to 0.1°. Once this refinement is finished, the software is allowed to perform the 3D reconstruction of the reciprocal space.

2.3.3 Peak processing and analysis

On the list of peak positions found in the phase called peak hunting, it is not possible to do other actions, in particular for data collected with active precession movement. The next step aims to establish which peaks of the list belong to the same rocking curve (we define later), and which reflection collected in different patterns is really the same. For these reasons, in this phase some elaborations are carried out:

1- *Clustering of adjacent peaks*: The diffraction peaks that are very close in consecutive patterns are considered as a single peak with coordinates determined calculating the intensity-weighted center of all the peaks belonging to that reflection.

2- *Calculation of the vector space of differences (DVS) and clustering in DVS*: It is an optional step which, however, produces a more complete reciprocal lattice. This step is based on the algorithm of Kolb[22] et al., and its result is a filtered autoconvolution of the lattice, which emphasizes the periodicity and completes the reciprocal space.

Is good to use this algorithm only in case of diffraction data with low noise and small disorder, because DVS can produce artifacts that are difficult to interpret. This procedure has also been implemented in the PETS 2.0 suite to cancel the distortions in the EDT data, and therefore lead to the definition of more accurate lattice parameters.

2.3.4 Lattice parameters

The software automatically defines the Cartesian coordinates of each pattern by positioning the positive x-axis parallel to the rotation axis of the goniometer. The z-axis is instead positioned towards the source of the radiation and the y-axis is positioned completing the right-handed system. The lattice parameters can be determined in two ways, either using the software's automatic algorithm, or using a manual approach. The automatic algorithm is based on the spatial difference (DVS) of Kolb[22] et al., as mentioned in the previous paragraph.

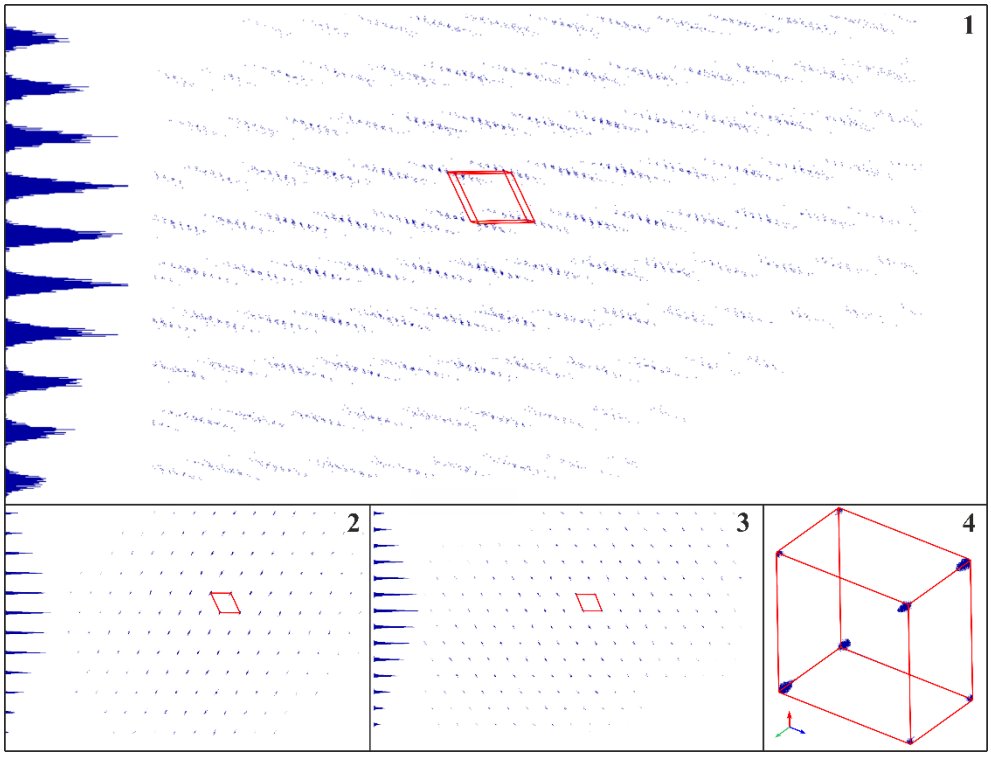

Fig. 16: Tools for searching the elementary cell: in figure 1 the diffraction spots in 3D with the cell in red; in 2 the projection of the cell along c; in 3 the projection of the cell along a; in 4 the diffraction spots folded from the software in the vertex of cell.

Instead, the manual determination of the cell parameters is based on the approach developed for the software JANA 2006[59]. With this method, the 3D reconstruction of the reciprocal space carried out by the software is manually rotated along main zone-axes and the interplanar distances in the reciprocal space are manually defined. In this way, a reciprocal cell indexing all the spots is manually derived. It is a very powerful method in the case of low-quality data.

2.3.5 Extraction of Intensities on Individual Frames

After the unit cell determination, the intensities of the diffraction patterns are extracted. The standard extraction method is the peak-background method. In this method, it is assumed that the circle whose diameter is defined by the user in the initial phase contains the complete intensity of the diffraction spot. The background value is calculated by fitting the pixels surrounding the peak, and therefore containing only the background, using the least squares method. Additionally, a correction is implemented in the software that allows small shifts of the integration position towards the center of the diffracted intensity, so as to take into account possible inaccuracies in the reflection location. Mathematically, the intensity is extracted as:

$$I = \sum_{peak\ area} p_i - \sum_{peak\ area} b_i$$

Where p_i are the counts on the i-pixels and b_i are the background calculated with least-square method.

The standard uncertainty (s.u.) on the intensity value is obtained as:

$$\sigma^2(I) = \sum_{peak\ area} \sigma^2(p_i) - \sum_{peak\ area} \sigma^2(b_i)$$

where $\sigma^2(b_i)$ is the standard uncertainty on the coefficients of the least squares method, and $\sigma^2(p_i)$ is a function of p_i and the characteristics of the detector. The uncertainty $\sigma^2(p_i)$ on the i-pixel can be approximated with an excellent accuracy according to Waterman & Evans[60] using the formula:

$$\sigma^2(p_i) = G\gamma p_i + \psi$$

where G is the detector gain, ψ is the detector cascade factor, which indicates how much noise is added to the physical Poisson noise by the detector due to its electronic system. The G and ψ parameters should be estimated for each detector before the electron diffraction data can be used for a quantitative determination.

2.3.6 Rocking curve fitting

The intensities in the PED diffraction data are very different from the intensities of the data where precession motion is not used. In fact, in the PED data, the maximum intensity is not obtained when the reflection is in the perfect Bragg condition, but is obtained when the reflection remains in the Bragg condition for a longer time during the precession cycle. Consequently, the intensity graph of a diffraction peak looks like double-peaked rocking curve, defined as "the camel"[57] (in figure 18).

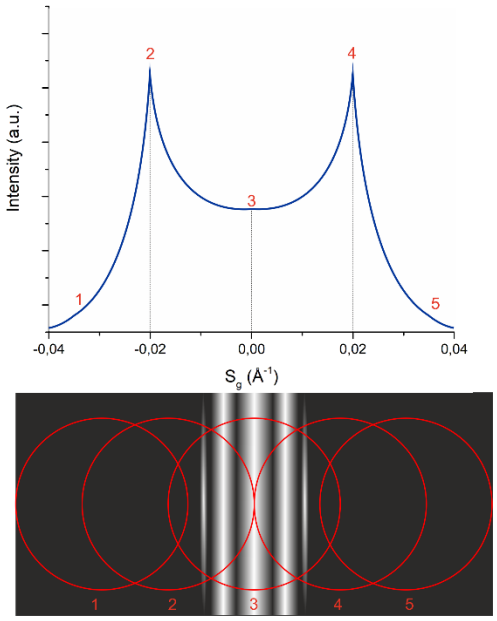

Fig.17: Explanation of the rocking curve in a PED collection. The PED intensity can be understood as a circular integral (schematically shown as red circles) over a CBED pattern. When the reflection is in t Brag position (circle 3), the measured diffraction intensity is lower than in the case the reflection is far from the exact Bragg position (circle 2 and 4).

To integrate the intensity of a PED diffraction, various geometric corrections and approximations were necessary[57]. Instead, the correction that the PETS 2.0 software operates is a correction that is carried out for the integration of the intensities on all the diffraction patterns collected off-zone. The approximation is beyond the subject of this thesis, but it is sufficient to know

that the software fitting the rocking curve, using two parameters: the reflection width and the mosaicity. The reflection width defines the shape of the base of the Lorentzian curve. Mosaicity, on the other hand, defines the enlargement of the rocking curve as a consequence of the increase in the diffraction angle. The rocking curve fitting is very useful for PED data as each reflection is integrated multiple times.

2.3.7 Optimization of Frame Orientation

The orientation of the diffraction pattern obtained from the orientation matrix and the angle of the TEM goniometer may be affected by inaccuracies. The software at this point operates an optimization of the orientation on each single frame. Pets 2.0 generates a simulated diffraction pattern and finds the optimal orientation by minimizing the differences between the pixels of the simulated pattern and those of experimental one with the least squares method. The parameters that are refined are:

1. The overall scale,
2. The three angles of rotation:
   α: angle of rotation around the main axis of the protractor.
   β: angle of rotation around the axis perpendicular to the first (it is the second angle of inclination in a double-tilt holder)
   ω: is the rotation of the pattern around the incident ray.

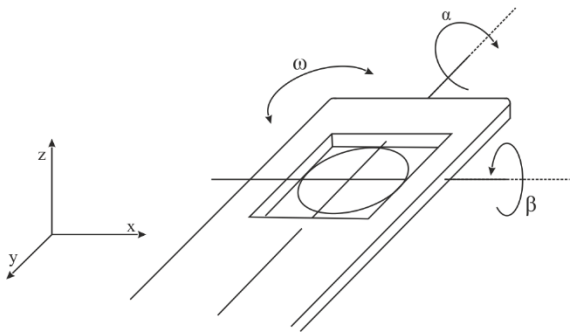

Fig.18: The three corners that the software refines to improve integration extraction.

3. The position of the diffraction center x_{cen}, y_{cen}
4. The rocking curve width ξ or the mosaics μ (only one of these can be refined because the two parameters are correlated)
5. The size of the reflections in the image plane; its shape is approximated to a Gaussian curve by one variance of σ_{ip}^2.

The calculated counts p_i^{calc} on the i-th pixel in the simulated pattern are calculated as:

$$p_i^{cal} = k \sum_g I_g \times N\left[\Delta(UB, \alpha, \beta, \omega, x_{cen}, y_{cen}), \sigma_{ip}^2\right] \times c(\alpha, \beta, \omega, \xi, \mu)$$

where k is a scale factor, I_g is the overall reflection intensity (kinematic intensity), $N(\dots)$ is the normal distribution, $\Delta(\dots)$ is the distance between the pixel I of the calculated position with respect to the corrected values of the variables $(UB, \alpha, \beta, \omega, x_{cen}, y_{cen})$ and $c(\dots)$ is the value of the normalized rocking-curve which is a function of the current orientation angles and rocking curve parameter. The $k, \alpha, \beta, \omega, x_{cen}, y_{cen}, \xi, \mu$ and σ_{ip} parameters are adjusted to minimize the function:

$$S = \sum (p_i^{obs} - p_i^{cal})^2$$

where p_i^{obs} is the count of pixel I in the experimental pattern subtracted of the background. This summation operates exclusively on the pixels that have a value of p_i^{cal} different from zero. One of the quantities that weigh the most in optimization is I_g, that is the overall reflection intensities. To a more accurate result, it is advisable to provide the software with an approximate set of integrated intensities (if the data allows it), so an iterative approach is recommended. Once the intensities have been integrated (step that will be explained in the next paragraph), it is possible to optimize the orientations of the patterns and then redo all the steps from the beginning, processing the peaks, research and refinement of the unit cell, connection of the rocking

curve and a new integration of the intensities, in order to obtain a better result on the intensities.

2.3.8 Integration of Intensities

In this step we arrive at the extraction of the diffraction intensities, if PEDT data are used, two different integration approaches can be used: kinematic approach and dynamic approach. In the kinematic approach the dynamic scattering is completely ignored, and electron diffraction data are treated as X-ray diffraction data. To operate the extraction of the intensity, the integration of a specific reflection on different patterns is considered as the same reflection and combined to have the best possible estimate of the intensity of the reflection. The kinematic approximation is therefore considered valid and such that the intensity is proportional to the square of the amplitude of the structure factor:

$$I(\vec{r}) = \left|\Phi_{cry}(\vec{H})\right|^2$$

For dynamic approach, in the integration phase, the dynamic effects are explicitly taken into consideration [57]. The integration of the reflection intensities is carried out according to the orientation of the single pattern. Then, each single pattern is treated separately, and the intensities are not combined with each other. So, with this method of integration the intensity depends not only on the structure factor of the single reflection but also on the structure factor of all the other reflections that are in a condition of diffracting. The result of this step is a standard file containing the intensities and for each reflection with their hkl indices, a file suitable to be imported for any crystallographic resolution software.

2.3.9 Generate Reciprocal Space-Sections and 3D Map

After extracting the intensities of the reflections, the Pets 2.0 software provides two very useful tools for establishing the symmetry group of the crystals. The first is the reciprocal space generation tool, which with standard settings produces twelve images (in TIF format) along the directions $hk0$, $hk1$, $hk2$, $hk3$ $h0l$, $h1l$ etc. with which it is possible to visually establish the extinction rules and define the symmetry or, as in the case of this thesis, the superspace symmetry of the crystal. The second tools provided by the software to help the user in establishing the symmetry, is the generation of a *3D*-map of the reciprocal space. With this the software will calculate the intensity distribution in a cube or a parallelepiped with the edges parallel to the reciprocal space vectors, to allow an orientation of the 3D map along the main directions to determine the extinctions rules figure.

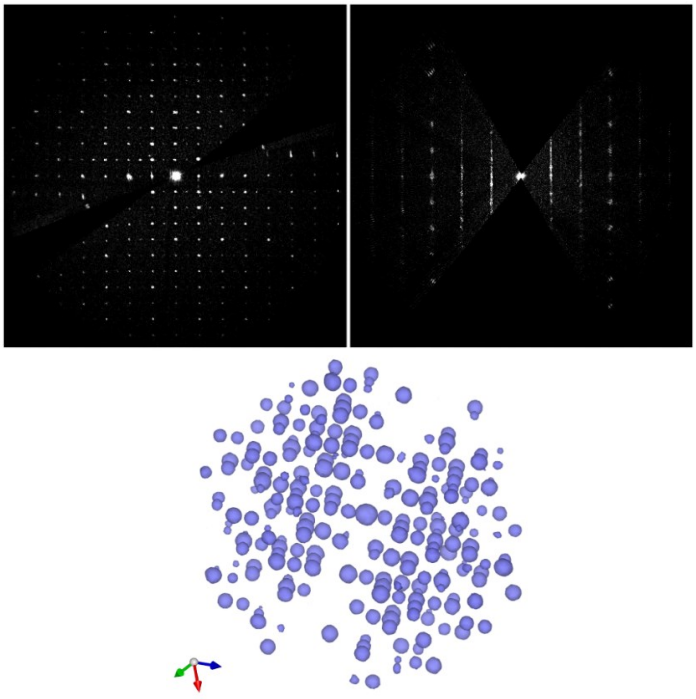

Fig. 19: Left: reciprocal space section hk0 of $Sr_5Nb_5O_{16}$; Rigth: the 0kl section of Na_3Ni_2BiO doped with Ca. Note the disorder along l direction. Bottom: example of 3D reconstruction of reciprocal space.

In many fields of physics exist the so-called "phase problem", and it is a loss of information that occurs when a physical measurement is made, and it is a limit due to the intrinsic nature of the measurement in quantum mechanics [61]. This effect is found both in the diffraction experiments and in the signal processing in the imaging experiments[62]. The detectors used in the diffraction experiments only measure a signal proportional to the number of electrons that are hitting them. This means that they measure a signal which is proportional to the square amplitude of the electron wave function, while any information about the wave function phase is lost [62]. As we have already explained, the waves diffracted by a crystal produce diffraction point and each of them corresponds to a point of the reciprocal lattice and represents a wave component having an amplitude and a phase. The overall diffusion of a crystal or the total scattering amplitude is a complex number and is the Fourier transform of the scattering power S($\vec{r}$) calculated in $\vec{s} = \vec{k} - \vec{k}_0$.

$$F\{S(\vec{r})\} = f(\vec{s})$$

Therefore, the scattering amplitudes are calculated as the Fourier transform of the electrostatic potential φ(r) in electron diffraction, of the electron density $\varrho(r)$ in X-ray diffraction and of the "nuclear density" $\delta(r)$ in neutron diffraction. An important property of the Fourier transform is that it is reversible:

$$F^{-1}\{f(\vec{s})\} = S(\vec{r})$$

If the Fourier anti-transform is applied to total scattering amplitude, information on the φ(r), $\varrho(r)$ and $\delta(r)$ can be calculated. However, as stated above, the phase of the structure factor is lost in a diffraction experiment. The loss of this information constitutes the fundamental problem of diffraction experiments known as “the phase problem in crystallography” and over the years many approaches have been developed to recover this lost information. Phase information is acquired with the help of phasing algorithms. The theory behind these algorithms is beyond the subject of this thesis, so we just mention briefly those used in this work. The main phase recovery methods employed in this thesis are those known as Direct Methods, which are widely

used for the structure solution of inorganic and small molecules[63]. As Direct Methods software we employed JANA2006[64] for the structure solution of perovskites and SHELXL[65] for the solution of MOF. Another valuable algorithm for the solution inorganic structures, embedded in Jana2006[64] software, is Charge flipping[59] that is particularly effective in case of incommensurately modulated structures.

2.4 Aperiodic Crystals

2.4.1 Type of Aperiodic Crystals

In the structural analysis of organic and inorganic compounds it has been observed the existence of the so-called "aperiodic crystals" (this term seems an oxymoron, because the crystalline state is characterized by structural periodicity). There are three types of aperiodic crystals:

- ***Quasi crystals***: They are those crystals that fill the space with translations of elements having a five, seven or ten-fold symmetry operators, prohibited by the theory of crystallography. These materials can therefore have an icosahedral, decagonal, dodecagonal etc. symmetry. However, these crystals have a long-range periodicity, a very sharp diffraction and are fully explained with a superspace approach. Generally, binary or ternary Al-based alloys can show this type of aperiodic crystals.

- ***Composite Crystals***: These incommensurate structures are formed by two distinct sub-structures, each one having its own three-dimensional symmetry. The intergrowth of the two independent subsystems gives rise to a crystal and generates a structural modulation.

- ***Incommensurable modulated structures***: In these crystals there is a perturbation of the basic crystalline structure. This perturbation has a translational symmetry that overlaps the periodicity of the mean (or base) structure in a non-commensurate way. This incommensurable perturbation can cause distortions in the structure in several ways:

  Displacive Modulations: Atomic positions are periodically shifted relative to the mean atomic coordinates within the basic structure.

  Occupational modulation: In this case there is a modulated and incommensurable sequence of occupied sites and vacancies inside the entire crystal.

Thermal modulation: It is the rarest type of distortion and concerns an incommensurable modulation on atomic vibrations which are referred to a tensor and is connected to the atomic displacement factors (ADP).

In this section, the basic information of the superspace approach will be provided along with the main characteristics of the diffraction patterns and the reconstructions of the reciprocal space in the case of modulated structure.

2.4.2 Superspace Approach

The first example of a modulated crystal was found in 1964 by Brouns, Visser and de Wolff by measuring the diffraction on a single crystal of γ-Na_2CO_3[66]. The diffraction patterns are composed by two sets of reflections, one indexed with a classical unit cell belonging to the Laue class and the other unindexed with the same cell. The only way to index the entire diffraction pattern is the introduction of a fourth vector that is related to the additional Miller index indicated with the m letter. The generic diffraction domain in the reciprocal space H, is indexed as follows:

$$H = ha^* + kb^* + lc^* + mq^* \quad (1)$$

$$q^* = \alpha a^* + \beta b^* + \gamma c^* \quad (2)$$

where q is the modulation vector and is a linear combination of the reciprocal lattice vectors. The parameters α, β, and γ can be rational (commensurate modulation) or irrational (incommensurate modulation) numbers. The Bragg peaks of the first group indexed with the classic three Miller indices are defined as main reflection; the second group, the reflections that need the fourth index and the modulation vector to be indexed, are called satellites. This distinction is very important because it is possible to define a basic structure, which describes the nature of the non-modulated crystal, and a periodic deviation, i.e. the structural modulation, causing the appearance of satellites in the diffraction patterns. The mathematical description of modulated and composite crystals is called superspace and was first formulated by Janner and Janssen[67,68] and de Wolf[68,69] in the '80. This approach is based on the definition of a space $(3 + n)D$, in which all the n-

dimensions following the third dimension serves to describe the modulated functions. In this thesis we studied $(3+1)D$ structures, so it was sufficient to add a fourth dimension $\vec{d}^*$ perpendicular to the $3D$ space. In figure 20 we see how from a row of reflections $1D$ with satellites due to an incommensurate modulation, it is possible to construct a reciprocal space $(1+1)D$ by introducing a direction d^* perpendicular to the initial direction $1D$.

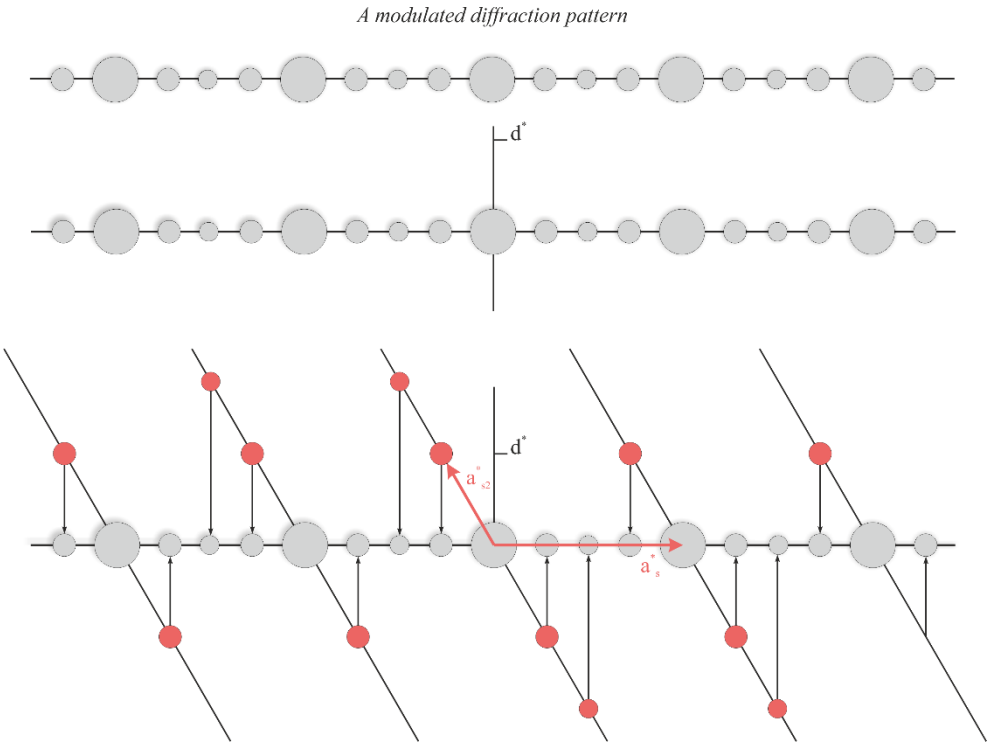

Fig. 20: Geometric construction of (1+1)D reciprocal lattice from a one-dimensional structure.

Once the new dimension has been introduced, a reciprocal lattice $(1+1)D$ can be defined $\vec{a}^*_{S1}$ and $\vec{a}^*_{S2}$ and constructs the experimental pattern as a projection of the lattice $(1+1)D$ along the initial $1D$ direction. By carrying out this method along the three dimensions it is possible to construct the complete reciprocal space $(3+1)D$ of the real incommensurate crystal. As mentioned before, in the superspace formalism the modulated structure is

described by a basic or average $3D$ structure defined by a standard space group and by a family of reflections with miller indices $(h, k, l, 0)$ and by a modulation function $\vec{u}^{\mu}(x_4)$ which describes the possible deviations of the modulated atomic parameters $\vec{u}$ (position occupation, ADP parameter etc.) from the average value of the basic structure. These modulation functions are wave functions described by the modulation vector $\vec{q}$ which determines their direction and periodicity. This vector is defined by a linear combination of the components of the lattice of the base structure. If one of the components of the vector $\vec{q}(\alpha\ \beta\ \gamma)$ is irrational the modulation is defined as incommensurate and causes the lack of perfect 3D periodicity. The argument of the modulation function defines the fractional coordinate x_4 in the $(3 + 1)D$ space. Therefore, the x_4 coordinate of the i-th atom in position x_{μ} is defined as:

$$x_4 = t + \vec{q} \cdot \vec{x}_{\mu} \tag{3}$$

where t is the origin of the fourth axis chosen arbitrarily. The modulation function could assume any mathematical form, as long as there is a periodicity along the x_4 coordinate:

$$u^{\mu}(x_4) = u^{\mu}(x_4 + 1) \tag{4}$$

this is a prerequisite otherwise the translational periodicity in the space $(3 + 1)D$ would be lost and the resulting diffraction would appear as stripes instead of having well confined satellites. So, thanks to its periodicity, the function can be expressed as a Fourier series:

$$u^{\mu}(x_4) = \sum_{n=1}^{\infty} A^n(\mu) \sin(2\pi n x_4) + B^n(\mu) \cos(2\pi n x_4) \tag{5}$$

where the Fourier coefficients A^n and B^n are the refineable variables of the modulation function. It is sufficient to refine few terms of the Fourier series because the amplitudes of successive orders decay rapidly. After having defined the modulation function $u^{\mu}(x_4)$, it is possible to explicit the direct superspace and its relationship with the real 3D space. With a geometric construction as in figure 21, it possible to visualize the direct superspace.

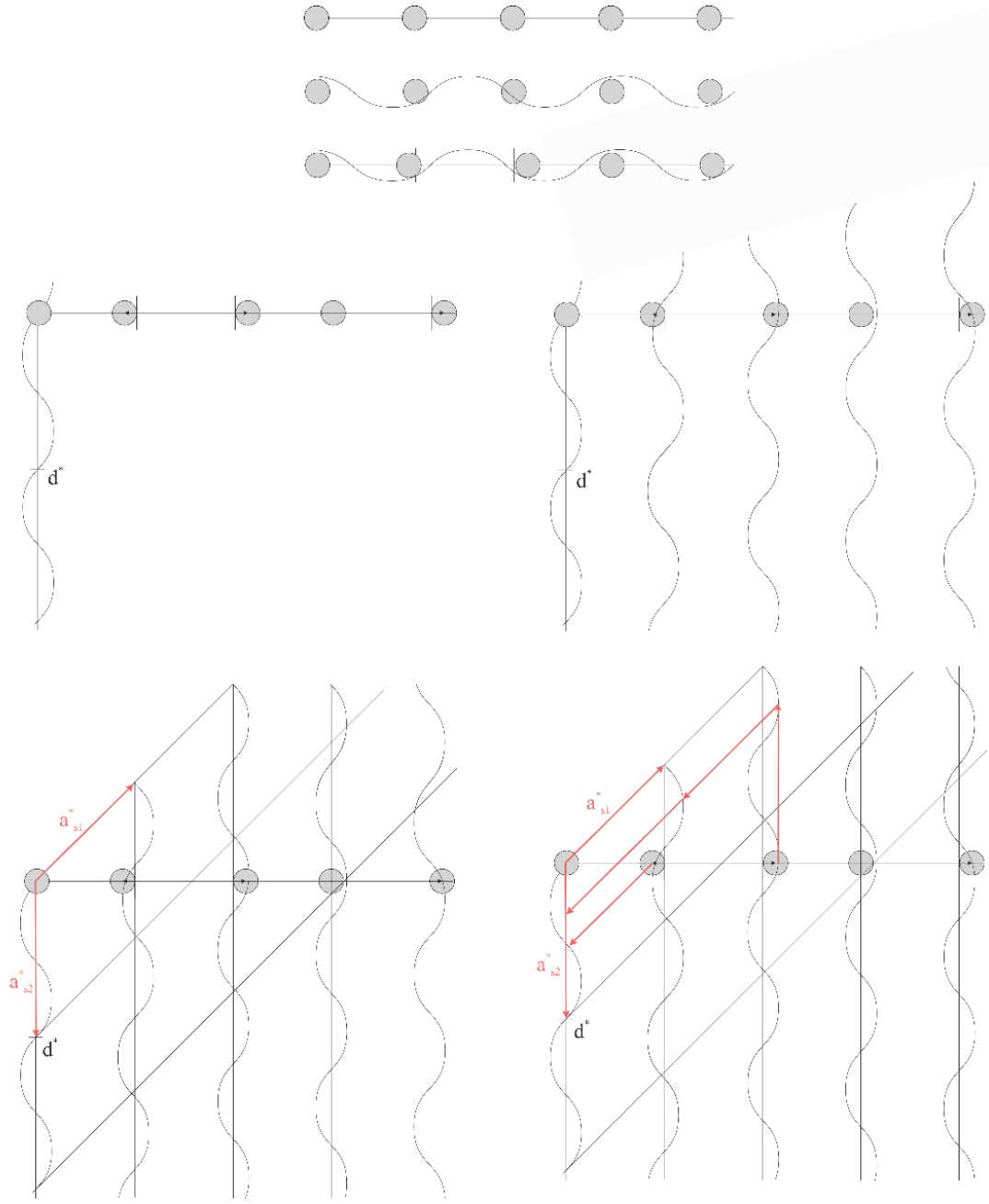

Fig. 21: Geometrical construction of the direct superspace starting from a linear chain of atoms (see text for details).

If we consider a chain of $1D$ atoms and apply a sinusoidal wave to the positions of these atoms (perturbation), the direct space in $(1+1)D$ is obtained by rotating the perturbation by 90° and using the positions of the atoms as a pivot. In this way, a direction perpendicular to the chain of atoms is defined and the period of the modulation function defines the periodicity $\vec{d}$ along the chain. Thus, it is possible to define a lattice also in the $(1+1)D$ space choosing as base $\vec{a}_{s1}$ and $\vec{a}_{s2}$, which lead to the definition of a unitary cell also in the superspace. The displacement of each atom of the chain $1D$ can therefore be referred respect to the unit cell selected by an integer number of translations of the base used, so that all the information to define the modulated crystal structure is present in the chosen unit cell.

It is evident that the real space is obtained as a section of the direct superspace perpendicular to the fourth axis. Each hypersection perpendicular to x_4 is $3D$ space and the position of the section is defined by the value of t variable. In the case of incommensurate modulated structures all sections t are virtually equivalent because in all points of the crystal the modulation function is present. In the case of a commensurate modulated structure, a correct choice of section t is required because all the possible sections are not equivalent. In the incommensurable structures, the t-plot is a straightforward method to draw the modulation function $u^{\mu}(x_4)$ and to evaluate the evolution of the modulation parameters in the crystalline structure. The t-plot is a graphic representation of the periodic modulation function with respect the values of x_4 or t variables in a range $0 \leq t \geq 1$. In the case of a commensurate modulated structure, there is always a N_s number that satisfies the equation $\vec{H}_0 = N_s\vec{q}$ where $\vec{H}_0$ is the reciprocal lattice vector of the base or average structure. In this case the components of the modulation vector are rational numbers and it is therefore possible to build a N_s-fold superstructure able to index all the reflections with three integer numbers. In the case of these structures, it is difficult to perform structural refinements of the superstructure with the classical crystallographic symmetry due to the increase of the independent refinable parameters and their mutual correlations. If the structural distortions involving the basic structure are minute, the satellites

intensities decreases rapidly and the refinement of many correlated parameters could bring to inconsistent results. The superspace approach, reduces the refinable parameters and their correlations. The most important difference of commensurate structure with incommensurate ones is that in commensurate crystal there are only discrete values of the modulation function, and these values are exactly N_s and are linked by:

$$x_4^{\mu} = t_0 + \frac{l}{N_s} + \vec{q} \cdot \vec{x}_0^{\mu} \qquad l = 1,2 \dots N_s \tag{6}$$

where $\vec{x}_0^{\mu}$ is the position of the $\vec{\mu}^{th}$ atom of the average structure and $\vec{t}_0$ is the origin chosen for the section t-plot. This equation implies that the positions along the fourth axis of the atom μ^{th} are finite and equal to N_s. Furthermore, under these conditions the choice of the origin of the phase t_0 of the modulation function modifies the modulation values for all atoms of the structure, producing different space groups for the superstructure. Finding the correct value of t_0 is one of the main challenges for solving commensurate structures when using the superspace approach. The diffraction patterns of aperiodic crystals have a similar symmetry to periodic crystals, i.e. they have a point symmetry. Therefore, the symmetry elements of the 3D space groups can also be generalized in a space with higher dimensions. The main reflections, which are indexed with the basic structure cell, must follow the point group of the basic structure, and the satellites must comply the same symmetry requirements. The point group operator transforms a main reflection into another equivalent reflection and must do the same with the satellites. This observation is a fundamental rule and allows us to establish that the additional dimension is subordinate to the real space and implies that no symmetry operator can exchange and/or mix the coordinates of the real space (3D) with the additional ones. In particular, the action of R on the modulation vector must respect the relation:

$$qR = \varepsilon q + H_R \tag{7}$$

where $\varepsilon = \pm 1$ and $\vec{H}_R$ is the reciprocal lattice vector, depends on R and is different from zero only if the modulation vector is commensurate. With this

relation it is possible to define the operator R in the space $(3+1)D$. This operator R transforms the basic structure lattice according to:

$$\begin{pmatrix} a' \\ b' \\ c' \end{pmatrix} = R \begin{pmatrix} a \\ b \\ c \end{pmatrix} \tag{8}$$

Combining equations 7 and 8 gives the matrix form of R_s:

$$R_s = \begin{pmatrix} R_{11} R_{12} R_{13} 0 \\ R_{21} R_{22} R_{23} 0 \\ R_{31} R_{32} R_{33} 0 \\ H_x \ H_y \ H_z \ \varepsilon \end{pmatrix} \tag{9}$$

Where $H_x \ H_y \ H_z$ are the components of the reciprocal vector $\vec{H}_R$, and $\varepsilon = \pm 1$. The symmetry element $\{R_s|\vec{t}\}$, where $\vec{t}$ is a non-integer translation and operates on atomic coordinates as:

$$\begin{pmatrix} x' \\ y' \\ z' \\ x_4' \end{pmatrix} = R_s \begin{pmatrix} x \\ y \\ z \\ x_4 \end{pmatrix} + \begin{pmatrix} t_1 \\ t_2 \\ t_3 \\ t_4 \end{pmatrix} \tag{10}$$

Then, after defining the symmetry operators in the superspace, it is possible to combine them to construct the symmetry groups in the superspace. The superspace formalism is formed by the classical symbol of the 3D space group of the basic structure, followed in round brackets by the components of the modulation vector and by the non-integer values of the translation along the fourth axis, which are indicated with letters: $s = 1/2$, $t = 1/3$, $q = 1/4$ and $h = 1/6$. For example, the superspace group $C2/m(\alpha 0 \gamma)0s$ indicates that the space group of the basic structure is $C2/m$ and that the parameter β of the modulation vectors $\vec{q}$ is zero for symmetry rules (it corresponds to the direction of the unique axis in the direct space). The generated superspace operators is a mirror plane with a non-integer translation along the fourth axis $\{my|000s\}$. The structure factor in the superspace is analogous to the definition in 3D space, for the diffraction techniques the scattering power $S(r)$ can also be defined in the space $(3+n)D$. The electrostatic potential for

electrons diffraction, the electron density for the X-ray diffraction and the "nuclear density" for the neutrons diffraction have maxima along the line, which is perpendicular to the real $3D$ space and represents the average position of the atom in the structure of base. The structure factors are therefore defined, as in conventional periodic crystals, as the Fourier transform $(3+n)D$ of the scattering power. Thus, the experimentally measured intensity of the reflections (h,k,l,m) is the modulus of the structure factor in the dimension $(3+n)D$. Hence, the relations between reciprocal and direct superspace are governed by the Fourier transform $(3+n)D$, and therefore the "phase problem" persists also for modulated structures. However, once the modulated structure in $(3+n)D$ space is solved, the real structure is obtained from a generalized section of the crystalline potential (for electrons) perpendicular to the additional n-dimensions. We start from the experimental diffraction pattern which is the projection on $3D$ space of the reciprocal lattice of $(3+n)D$ the structure, by operating with an inverse Fourier transform on the reciprocal lattice of the superspace. The generalized crystalline potential is obtained, and the structure is resolved in space $(3+n)D$. After that, the real structure is obtained from a t-section of the generalized crystalline potential perpendicular to 3D space, as explained above in the case of commensurate structures.

2.5 References

1. Bragg, W. H., Bragg Apr, W. L., H Bragg, B. W. & Professor of Physics, C. The reflection of X-rays by crystals. *Proceedings of the Royal Society of London. Series A, Containing Papers of a Mathematical and Physical Character* **88**, 428–438 (1913).

2. Ewald, P. P. X-ray diffraction by finite and imperfect crystal lattices. *Proceedings of the Physical Society* **52**, 167–174 (1940).

3. Dorset, D. L. Electron Crystallography. *Acta Crystallographica Section B: Structural Science* **52**, 753–769 (1996).

4. Vincent, R. & Midgley, P. A. Double conical beam-rocking system for measurement of integrated electron diffraction intensities. *Ultramicroscopy* **53**, 271–282 (1994).

5. Midgley, P. A. & Eggeman, A. S. Precession electron diffraction - A topical review. *IUCrJ* vol. 2 126–136 (2015).

6. Gemmi, M. & Nicolopoulos, S. Structure solution with three-dimensional sets of precessed electron diffraction intensities. *Ultramicroscopy* **107**, 483–494 (2007).

7. J. Gjønnes, V. Hansen, B. S. Berg, P. Runde, Y. Cheng, K. Gjønnes, D. Dorset, C. Gilmore. Structure Model for the Phase AlmFe Derived from Three-Dimensional Electron Diffraction Intensity Data Collected by a Precession Technique. Comparison with Convergent-Beam Diffraction. *Acta Crystallographica Section A: Foundations of Crystallography* **54**, 306–319 (1998).

8. Gemmi, M. Xiaodong Zou, Sven Hovmöller, Andrea Migliori, Marie Vennström, Yvonne Andersson. Structure of Ti_2P solved by three-dimensional electron diffraction data collected with the precession technique and high-resolution electron microscopy. *Acta Crystallographica Section A: Foundations of Crystallography* **59**, 117–126 (2003).

9. Gemmi, M., Klein, H., Rageau, A., Strobel, P. & le Cras, F. Structure solution of the new titanate $Li_4Ti_8Ni_3O_{21}$ using precession electron diffraction. *Acta Crystallographica Section B: Structural Science* **66**, 60–68 (2010).

10. P. Boullay, V. Dorcet, O. Pérez, C. Grygiel, W. Prellier, B. Mercey, and M. Hervieu. Structure determination of a brownmillerite $Ca_2Co_2O_5$ thin film by precession electron diffraction. *Physical Review B - Condensed Matter and Materials Physics* **79**, 184108 (2009).

11. J. Hadermann, M. Abakumov, A. Tsirlin, Vladimir P. Filonenko, J. Gonnissen, H. Tan, J. Verbeeck, M. Gemmi, E. Antipov, H. Rosner. Direct space structure solution from precession electron diffraction data: Resolving heavy and light scatterers in $Pb_{13}Mn_9O_{25}$. *Ultramicroscopy* **110**, 881–890 (2010).

12. J. Hadermann, A. Abakumov, S. Van Rompaey, T. Perkisas, Y. Filinchuk, G. Tendeloo. Crystal structure of a lightweight borohydride from submicrometer crystallites by precession electron diffraction. *Chemistry of Materials* **24**, 3401–3405 (2012).

13. Klein, H. Precession electron diffraction of Mn2O3 and PbMnO2.75: Solving structures where X-rays fail. *Acta Crystallographica Section A: Foundations of Crystallography* **67**, 303–309 (2011).

14. Kolb, U., Gorelik, T., Kübel, C., Otten, M. T. & Hubert, D. Towards automated diffraction tomography: Part I-Data acquisition. *Ultramicroscopy* **107**, 507–513 (2007).

15. Kolb, U., Mugnaioli, E. & Gorelik, T. E. Automated electron diffraction tomography - A new tool for nano crystal structure analysis. in *Crystal Research and Technology* vol. 46 542–554 (John Wiley & Sons, Ltd, 2011).

16. Palatinus, L., Klementová, M., Dřínek, V., Jarošová, M. & Petříček, V. An incommensurately modulated structure of η0-phase of Cu 3+xsi determined by quantitative electron diffraction tomography. *Inorganic Chemistry* **50**, 3743–3751 (2011).

17. Gemmi, M. & Oleynikov, P. Scanning reciprocal space for solving unknown structures: Energy filtered diffraction tomography and rotation diffraction tomography methods. *Zeitschrift fur Kristallographie* **228**, 51–58 (2013).

18. Wan, W., Sun, J., Su, J., Hovmöller, S. & Zou, X. Three-dimensional rotation electron diffraction: Software RED for automated data collection and data processing. *Journal of Applied Crystallography* **46**, 1863–1873 (2013).

19. Clabbers, M. T. B., Gruene, T., Parkhurst, J. M., Abrahams, J. P. & Waterman, D. G. Electron diffraction data processing with DIALS. *Acta Crystallographica Section D: Structural Biology* **74**, 506–518 (2018).

20. Leslie, A. G. W. & Powell, H. R. Processing diffraction data with mosflm. in 41–51 (Springer, Dordrecht, 2007).

21. Kabsch, W. XDS. *Acta Crystallographica Section D Biological Crystallography* **66**, 125–132 (2010).

22. Kolb, U., Gorelik, T. & Otten, M. T. Towards automated diffraction tomography. Part II-Cell parameter determination. *Ultramicroscopy* **108**, 763–772 (2008).

23. Shi, D., Nannenga, B. L., Iadanza, M. G. & Gonen, T. Three-dimensional electron crystallography of protein microcrystals. *eLife* **2013**, (2013).

24. Fan, J. *et al.* New monoclinic phase at the composition Cu2SnSe3 and its thermoelectric properties. *Inorganic Chemistry* **52**, 11067–11074 (2013).

25. Mugnaioli, E., Gorelik, T. & Kolb, U. "Ab initio" structure solution from electron diffraction data obtained by a combination of automated diffraction tomography and precession technique. *Ultramicroscopy* **109**, 758–765 (2009).

26. Kolb, U., Mugnaioli, E. & Gorelik, T. E. Automated electron diffraction tomography - A new tool for nano crystal structure analysis. in *Crystal Research and Technology* vol. 46 542–554 (John Wiley & Sons, Ltd, 2011).

27. Palatinus, L. *et al.* Hydrogen positions in single nanocrystals revealed by electron diffraction. *Science* **355**, 166–169 (2017).

28. Zhang, D., Oleynikov, P., Hovmoller, S. & Zou, X. Collecting 3D electron diffraction data by the rotation method. *Zeitschrift fur Kristallographie* **225**, 94–102 (2010).

29. Guo, P. *et al.* Accurate structure determination of a borosilicate zeolite EMM-26 with two-dimensional 10 × 10 ring channels using rotation electron diffraction. *Inorganic Chemistry Frontiers* **3**, 1444–1448 (2016).

30. Mugnaioli, E. *et al.* Ab initio structure determination of vaterite by automated electron diffraction. *Angewandte Chemie - International Edition* **51**, 7041–7045 (2012).

31. Mayence, A. *et al.* Phase identification and structure solution by three-dimensional electron diffraction tomography: Gd-phosphate nanorods. *Inorganic Chemistry* **53**, 5067–5072 (2014).

32. Yun, Y. *et al.* Phase identification and structure determination from multiphase crystalline powder samples by rotation electron diffraction. *Journal of Applied Crystallography* **47**, 2048–2054 (2014).

33. Jiang, J. *et al.* Synthesis and structure determination of the hierarchical meso-microporous zeolite ITQ-43. *Science* **333**, 1131–1134 (2011).

34. Mugnaioli, E. & Kolb, U. Applications of automated diffraction tomography (ADT) on nanocrystalline porous materials. in *Microporous and Mesoporous Materials* vol. 166 93–101 (Elsevier, 2013).

35. Martínez-Franco, R. *et al.* Synthesis of an extra-large molecular sieve using proton sponges as organic structure-directing agents. *Proceedings of the National Academy of Sciences of the United States of America* **110**, 3749–3754 (2013).

36. Feyand, M. *et al.* Automated Diffraction Tomography for the Structure Elucidation of Twinned, Sub-micrometer Crystals of a Highly Porous, Catalytically Active Bismuth Metal-Organic Framework. *Angewandte Chemie* **124**, 10519–10522 (2012).

37. Zhang, Y. B. *et al.* Single-crystal structure of a covalent organic framework. *Journal of the American Chemical Society* **135**, 16336–16339 (2013).

38. Liu, Y. *et al.* 3D Covalent Organic Frameworks of Interlocking 1D Square Ribbons. *Journal of the American Chemical Society* **141**, 677–683 (2019).

39. Rozhdestvenskaya, I. *et al.* The structure of charoite, $(K,Sr,Ba,Mn)_{15–16}(Ca,Na)_{32}[(Si_{70}(O,OH)_{180})](OH,F)_{4.0}\ nH_2O$, solved by conventional and automated electron diffraction. *Mineralogical Magazine* **74**, 159–177 (2010).

40. Gemmi, M., Campostrini, I., Demartin, F., Gorelik, T. E. & Gramaccioli, C. M. Structure of the new mineral sarrabusite, $Pb_5CuCl_4(SeO_3)_4$, solved by manual electron-diffraction tomography. *Acta Crystallographica Section B: Structural Science* **68**, 15–23 (2012).

41. Capitani, G. C. *et al.* The Bi sulfates from the Alfenza Mine, Crodo, Italy: An automatic electron diffraction tomography (ADT) study. *American Mineralogist* **99**, 500–510 (2014).

42. Plasil, J. *et al.* Crystal structure of lead uranyl carbonate mineral widenmannite: Precession electron-diffraction and synchrotron powder-diffraction study. *American Mineralogist* **99**, 276–282 (2014).

43. Németh, P. *et al.* A nanocrystalline monoclinic $CaCO_3$ precursor of metastable aragonite. *Science Advances* **4**, 6178–6190 (2018).

44. Gorelik, T. E., Czech, C., Hammer, S. M. & Schmidt, M. U. Crystal structure of disordered nanocrystalline αII-quinacridone determined by electron diffraction. *CrystEngComm* **18**, 529–535 (2016).

45. Mugnaioli, E., Reyes-Gasga, J., Kolb, U. & Bres, E. Evidence of Noncentrosymmetry of Human Tooth Hydroxyapatite Crystals Biocompatible Coatings View Project Study of synthetic hydroxyapatite View project.

46. Mugnaioli, E. & Gemmi, M. Single-crystal analysis of nanodomains by electron diffraction tomography: Mineralogy at the order-disorder borderline. *Zeitschrift fur Kristallographie - Crystalline Materials* **233**, 163–178 (2018).

47. Lanza, A. *et al.* Nanobeam Precession-Assisted 3D electron diffraction reveals a new polymorph of hen egg-white lysozyme. *IUCrJ* **6**, 178–188 (2019).

48. Gemmi, M., la Placa, M. G. I., Galanis, A. S., Rauch, E. F. & Nicolopoulos, S. Fast electron diffraction tomography. *Journal of Applied Crystallography* **48**, 718–727 (2015).

49. Nederlof, I., van Genderen, E., Li, Y. W. & Abrahams, J. P. A Medipix quantum area detector allows rotation electron diffraction data collection from submicrometre three-dimensional protein crystals. *Acta Crystallographica Section D: Biological Crystallography* **69**, 1223–1230 (2013).

50. Nannenga, B. L., Shi, D., Leslie, A. G. W. & Gonen, T. High-resolution structure determination by continuous-rotation data collection in MicroED. *Nature Methods* **11**, 927–930 (2014).

51. Wang, Y. *et al.* Elucidation of the elusive structure and formula of the active pharmaceutical ingredient bismuth subgallate by continuous rotation electron diffraction. *Chemical Communications* **53**, 7018–7021 (2017).

52. Simancas, J. *et al.* Ultrafast Electron Diffraction Tomography for Structure Determination of the New Zeolite ITQ-58. *Journal of the American Chemical Society* **138**, 10116–10119 (2016).

53. van Genderen, E. *et al.* Ab initio structure determination of nanocrystals of organic pharmaceutical compounds by electron diffraction at room temperature using a Timepix quantum area direct electron detector. *Acta Crystallographica Section A: Foundations and Advances* **72**, 236–242 (2016).

54. Sawaya, M. R. *et al.* Ab initio structure determination from prion nanocrystals at atomic resolution by MicroED. *Proceedings of the National Academy of Sciences of the United States of America* **113**, 11232–11236 (2016).

55. Nannenga, B. L., Shi, D., Leslie, A. G. W. & Gonen, T. High-resolution structure determination by continuous-rotation data collection in MicroEDED. *Nature Methods* **11**, 927–930 (2014).

56. Yonekura, K., Kato, K., Ogasawara, M., Tomita, M. & Toyoshima, C. Electron crystallography of ultrathin 3D protein crystals: atomic model with charges. *Proceedings of the National Academy of Sciences of the United States of America* **112**, 3368–3373 (2015).

57. Palatinus, L. *et al.* Specifics of the data processing of precession electron diffraction tomography data and their implementation in the program PETS2.0. *Acta Crystallographica Section B: Structural Science, Crystal Engineering and Materials* **75**, 512–522 (2019).

58. Kolb, U., Gorelik, T. & Mugnaioli, E. Automated diffraction tomography combined with electron precession: A new tool for ab initio nanostructure analysis. in *Materials Research Society Symposium Proceedings* vol. 1184 11–23 (Materials Research Society, 2009).

59. Petrícek, V., Dušek, M. & Palatinus, L. Crystallographic computing system JANA2006: General features. *Zeitschrift fur Kristallographie* vol. 229 345–352 (2014).

60. David Waterman, Gwyndaf Evans. Estimation of errors in diffraction data measured by CCD area detectors. *Journal of applied crystallography* **43**, 1356–1371 (2010).

61. Taylor, G. The phase problem. *urn:issn:0907-4449* **59**, 1881–1890 (2003).

62. Shechtman, Y. *et al.* Phase Retrieval with Application to Optical Imaging: A contemporary overview. *IEEE Signal Processing Magazine* **32**, 87–109 (2015).

63. Giacovazzo, C., Capitelli, F., Cuocci, C. & Ianigro, M. Direct methods and applications to electron crystallography. *Advances in Imaging and Electron Physics* **123**, 291–310 (2002).

64. Petříček, V., Dušek, M. & Palatinus, L. Crystallographic Computing System JANA2006: General features. *Zeitschrift für Kristallographie - Crystalline Materials* **229**, 345–352 (2014).

65. Sheldrick, G. M. Crystal structure refinement with SHELXL. *Acta Crystallographica Section C: Structural Chemistry* **71**, 3–8 (2015).

66. Brouns, E., Visser, J. W., de Wolff, P. M. An anomaly in the crystal structure of Na2CO3. *urn:issn:0365-110X* **17**, 614–614 (1964).

67. Janner, A., Janssen, T. Symmetry of incommensurate crystal phases. I. Commensurate basic structures. *urn:issn:0567-7394* **36**, 399–408 (1980).

68. de Wolff, P. M., Janssen, T., Janner, A. The superspace groups for incommensurate crystal structures with a one-dimensional modulation. *urn:issn:0567-7394* **37**, 625–636 (1981).

69. de Wolff, P. M. The Pseudo-Symmetry of Modulated Crystal Structures. *urn:issn:0567-7394* **30**, 777–785 (1974).

3. State of Art of Doubly Ordered Perovskite

3.1 Crystal structure

Over the years, the class of perovskite compounds having general formula ABX_3 has been intensively studied due to their innate physical and chemical properties. Among physical properties, they encompass several complex magnetic orderings, dielectric, piezo and ferroelectric effects, ionic and electronic conductivity and, in the cuprates family, high critical temperature superconductivity. Perovskites have been successfully employed as catalyst for oxidative processes or as electrodes in fuel cell technology. The origin of the stunning versatility is mainly related to the flexibility of the chemical composition (see Figure 2) and related crystalline phases. Starting from the aristotype $CaTiO_3$ compound, the A and B sites can be occupied by several chemical species providing the chance to tune the chemical and physical properties. Additionally, perovskite-type structures can be obtained with elements in the X site different from oxygen, namely F^-, Br^- or I^- anions and recently, halides-based variants have triggered increasing attention for the stunning photovoltaic properties.

In this structure type, *A* are a large cations *12*-fold coordinated in cube-octahedral cavities and *B* are a small cations octahedrally coordinated by *X* anions[1]. The aristotype structure has a primitive cubic cell with space group symmetry *Pm-3m*.

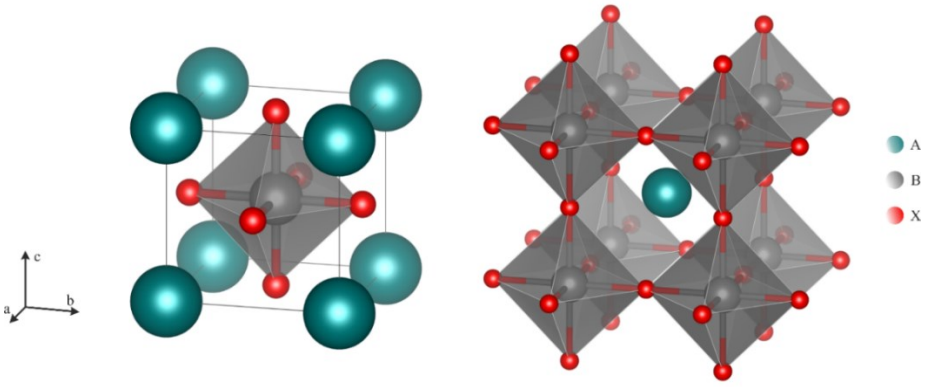

Fig. 1: Crystal structure of the prototypical perovskite phase.

The structure can be described in different ways: The first way views *A*-site cations in planes with the oxygens to form a AX_3 close-packed (111) layers. This disposition of *A* cations is comparable with the arrangement of Cl^- anions in *NaCl* structure, while the *B*-site cations reside in all octahedral interstitial sites thus forming BX_6 octahedra. Another way to view the structure is to impose corner-sharing BX_6 octahedra in the corners of a primitive cubic cell that form a 3D network, with *A* cation in the big interstitial site with dodecahedral coordination. Describing the structure with fractional coordinates, the *A*-site is in $(1/2, 1/2, 1/2)$, the *B*-site is at the origin and the X anion position half-way between adjacent *B* cations $(1/2, 0, 0)$, $(0, 1/2, 0)$, $(0, 0, 1/2)$. In the aristotype perovskite it is possible to calculate the lattice parameter a_p using the formula:

$$a_p = \sqrt{2}(r_A + r_X) = 2(r_B + r_X)$$

Where r_A, r_B and r_X are the radii of the A-site and B-site cations and anions, respectively. Perovskites, as mentioned before, can be made up of almost all the elements of the periodic table, as can be seen from the figure. In particular, the green coloured elements can occupy site *A,* in blue site *B* and in orange site *X*. And of course, based on their composition, they have different technological properties.

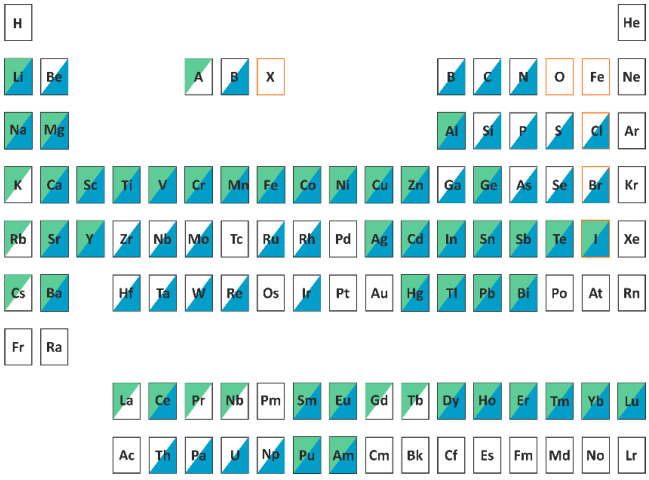

Fig. 2: Highlighted atoms can constitute materials with perovskite structure.

3.1.1 Deviations from Ideality

As previously mentioned, the perovskite structure can accommodate many metal ions, with an consequently variance reticular parameters. Goldshmidt in *1995* defined a tolerance factor t to evaluate how close a perovskite structure is to the ideal one and assessed the difference between the size of the two cations *A* and *B* and the anions[2]:

$$t = \frac{(r_A + r_X)}{\sqrt{2}\,(r_B + r_X)}$$

Since the t factor distinguishes between perovskite and non-perovskite only in 74% of cases and even less in cases where chlorides, bromides and iodides are present[3], a recent study by C. J. Bartel introduced a new tolerance factor *τ,*:

$$\tau = \frac{r_X}{r_B} - n_A\left(n_A - \frac{r_A/r_B}{\ln(r_A/r_B)}\right)$$

Where n_A is the oxidation state of *A*, r_i is the ionic radius of ion *i* and $r_A$is grater then r_B by definition. A value of τ lower than *4.18* indicates that perovskite structure is favoured/allowed.

In the case of double perovskites, which we define in subsequent chapters, the Goldshmidt factor *t* changes to[4]:

$$t = \frac{\left(\frac{r_{A\prime} + r_{A\prime\prime}}{2} + r_X\right)}{\sqrt{2}\,\left(\frac{r_{B\prime} + r_{B\prime\prime}}{2} + r_X\right)}$$

The new factor τ was designed on ABX_3 perovskites, but depends only on the chemical composition, it is adaptable to double perovskites without modifications, but only taking as the value of r_A and r_B an arithmetic mean of the radius of the two different cations occupying each homologous site[3]. Perovskites with similar τ-values but made with large A^{2+} cations have a structure with higher symmetry than perovskites with small A^{2+} cations.

In order to better reflect the dimensional effect of A^{2+} cations, a new parameter, called the fitness factor, has been defined:

$$\Phi = \frac{\sqrt{2}r_A}{r_B + r_O}$$

The value of $r_B + r_O$ expresses the size of the cubo-octahedral cavity formed by eight BO_6 octahedra, therefore Φ describes the size matching between the *A*-site cation and cavity[5]. The fitness factor is particularly useful to predict the symmetry of doubly ordered perovskites. For a doubly ordered perovskite with alkali earth metal in the structure, the cubic cell occurs for $\Phi > 1.00$ the tetragonal system at $0.90 < \Phi < 1.00$, the orthorhombic system at $0.90 < \Phi < 0.93$ and monoclinic system $\Phi < 0.90$. The ideal values of $t = 1$ or $\tau = 4.181$ and $\Phi = 1.00$ are based on the approximation of cations as solid spheres, therefore any deviation from the value of 1 indicates an instability in the structures. These instabilities are mitigated by a lowering of the symmetry with respect to the ideal symmetry group *Pm-3m*. The principal distortions, that lower the symmetry, are:

- Tilting of the BX_6 octahedra.
- Cationic displacement.
- Ordering of cations.

These three deformations, which lead to numerous different symmetries, are also the strength of perovskites.

3.1.2 Glazer Formalism

The tolerance factor (*t*) is also a predictor of what type of structural distortion occurs in perovskites. For example, a value greater than 1 can lead to a distortion that can cause a sharing of the faces instead of the vertices of the BO_6 octahedra. Conversely, if the *t* value is less than one, a tilting of the BO_6 octahedra is observed and the smaller the *t*-value, the larger is the tilt. Furthermore, if the cations of site *A* are much smaller than their cavity, there is a coordinated inclination of the BO_6 octahedrons. This distortion reduces the size of the cavity of site *A* and can reduce its coordination. If the BO_6

octahedron tilts rigidly, the bond lengths of *B-O* remain unchanged, but the distance *A-O* is reduced. All possible tilt of the octahedra and notation to describe possible combinations have been defined by Glazer[6]. The octahedra can tilt around one of the three axes as a single entity, so the bond lengths *B-O-B* remain constant, the inclination of an octahedron implies the inclination of an adjacent one. Glazer formalism describes magnitude and phase of the octahedral tilt using three characters with their apexes to define 23 different combinations or "tilt systems". The use of the same letter (*a*, *b* or *c*) implies that the tilt is equal along the three axes, the apexes are used to indicate whether the inclinations are in phase or in anti-phase or non-existent along a well-defined axis. For example, $a^0b^+c^-$ indicates a system where the amount of tilt is different around each axis: no tilt about the x-axis, in-phase tilt about the y-axis and anti-phase tilt about z-axis.

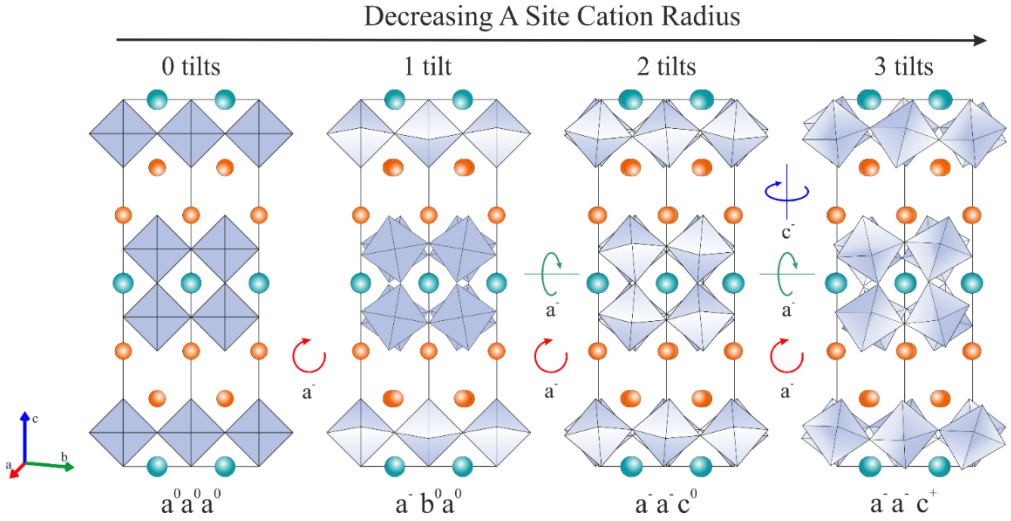

Fig 3: Three examples of inclination. From left to right: system with no inclination; with one inclination in antiphase along x-axis; with two inclinations with the same magnitude in antiphase along the x and y axis; three inclinations, two with the same magnitude in antiphase along x-axis and y-axis and one with different magnitude in phase along z-axis.

3.1.3 Jahn-Teller Distortion

The JT effect is generally found in octahedral co-ordinations involving transition metals. When a perovskite is constituted, a transitions metal is possible doubly degenerate electronic ground state. An example occurs with Co^{2+} ions (d^7) in high spin state, that have an electronic state $(t_{2g})^5\ (e_g)^2$:

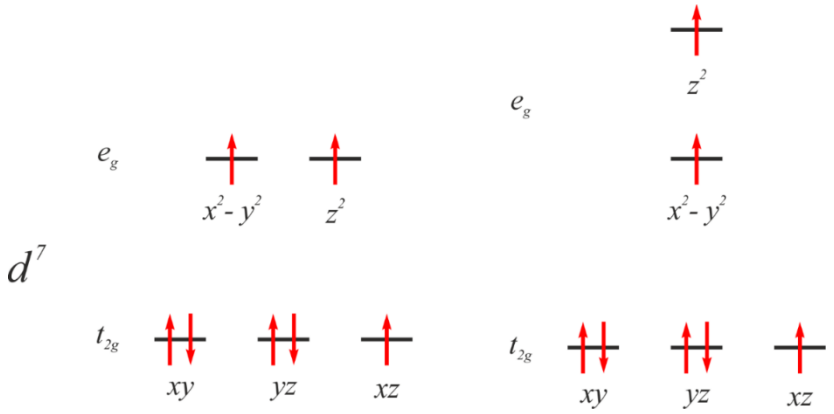

Fig. 4: Possible electron configuration of a d^7 atom: on the left the high spin state; on the right the configuration with the removal of degeneration of the orbitals e_g.

This configuration has an orbital degeneracy, but many complexes deform along one of the molecular axes, with the effect of removing the degeneracy of e_g orbitals and reducing the overall energy of the octahedrons. Jahn Teller's distortion can both lengthen and shorten the bond length (the theorem does not speak of direction but only of distortion)[7]. The extension or shortening of the bond has the purpose of reducing the electrostatic repulsion between the electronic pairs of the ligands *X* in order to reduce the overall energy of the octahedral geometry. The Jahn-Teller distortion (or Jahn-Teller effect) is very common for d^9, d^7(such as Ni^{3+}, low spin) and d^4 (Mn^{3+}, high spin) cations. Another distortion involving transition metal cations d^0 (like W^{6+}, Nb^{5+} and Ti^{4+} [8]) coordinated with an octahedra geometry is the decentralization of the cation with respect to the centre of the octahedron. This second order Jahn-Teller distortion lowers the orbital energy thanks to the hybridization of the *p* orbital of the anion. The overlap of the orbitals leads to different energetic

states but with very close energies. To remove these degenerations a spontaneous distortion occurs if the following three conditions occur:

- The t_{2g} must be free
- The difference between the energy of HOMO of anion and LUMO of cation must be small.
- There must be a distortion of the same symmetry as the transition between HOMO and LUMO.

These conditions are met by transition metal cations d^0 with an octahedral coordination, and the decentralization of the cation increases with increasing charge and decreases with increasing size. This phenomenon also depends on the difference between HOMO and LUMO and on the ability of the rest of the structure to withstand distortion[8]. It is therefore deduced that the first order Jahn-Teller distortion preserves the inversion center of the octahedra unlike the second order distortion.

3.2 Doubly Ordered Perovskites

3.2.1 Chemical Composition

The composition of the perovskite has a high versatility and are classified into solid solution and order phase. The solid solutions such as: $A_{1-x}A'_xBO_3$, $AB_{1-y}B'_yO_3$ or $A_{1-x}A'_xB_{1-y}B'_yO_3$ involve cations *A'* and *B'* with different charge with respect to *A* and *B*. In this case defects, mixed occupancy, or vacancies are formed in the structure[9]. If we consider the case in which the ions A^{3+} in the $A^{3+}B^{3+}X_3$ structure are replaced by an A^{2+} cation, the charge difference leads to oxide formations with ionic vacancies (V_0):

$$[A^{3+}_{1-x}A^{2+}_x][B^{3+}]O_{3-(x/2)}V_{o(x/2)}$$

$$[A^{3+}_{1-x}A^{2+}_x][B^{3+}_{1-x}B^{4+}_x]O_3$$

$$[A^{3+}_{1-x}A^{2+}_x]\left[B^{3+}_{1-2y}B^{4+}_{2y}\right]O_{3-(x/2)+}V_{o(x/2)-y}$$

The oxides of the first case are formed if the metal cations have invariable valences; Example of these compounds are: $CaTi_{1-x}Al_xO_{3-y}$, $CaTi_{1-x}Mg_xO_{3-y}$, $SrTi_{1-x}Al_xO_{3-y}$[10] (which are solid electrolytes). The compounds of the second case are formed if the state of cation *B* is tetravalent or less; an example is $La_{1-x}Sr_xMnO_3$[11]. The last compositional variant is formed when the tetravalent charge of the cation *B* is not stable and therefore the structure is stable thanks to the simultaneous formation of vacancies of the B^{4+} cation and electronic holes ($La_{1-x}Sr_xCoO_{3-y}$[12]). Further, a more complex ordered combination of perovskites encounters generic formula like: $AA'BB'O_6$, $A_2BB'O_6$, $AA'_2B_2B'O_9$ and $A_4B_3B'O_{12}$. The formation of an ordered phase depends on the combination of different metal cations featured by definite valence and ionic size. The subclass $AA'BB'O_6$[13] and $A_2BB'O_6$[1] are referred to as double perovskite; in these types of perovskites the *B*-cations have three possible different orders: rock-salt, layered and random.

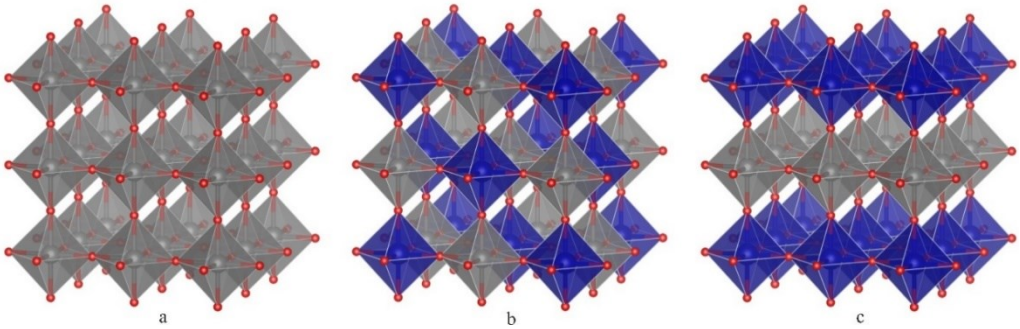

Fig. 5: Possible arrangements of B-cation in double perovskite: a) Random, (b) Rock-salt, (c) Layered.

The difference between the three arrangements is regulated by different factors (ionic radius, charge, cation coordination geometry and *A-B* cation size ratio) but the most important factor is the difference in ionic charge[4]. It is more probable to have a rock-salt order when the charge difference between the two cations *B* and *B'* is greater than two; if the difference is less than two, there is a random arrangement; the layered arrangement is instead very rare for *B* and *B'* cations[4]. The three different sublattices can be discriminated thanks to systematic absences in diffraction patterns. The presence of *k=2n+1* reflection on *0kl* projection indicates the rock-salt order of *B*-site cations, whereas the presence of reflections with order *h+l=2n+1* in *h0l* projection indicates the layered order of *B*-site. For the random order of *B*-site there are no significant systematic absences.

Table 1: crystallographic information on Double Perovskite with $a_p \approx 4Å$

Sublattice Type	Cell Size	Cristal System	Space Group
Random	$1a_p \times 1a_p \times 1a_p$	Cubic	$Pm\bar{3}m$
	$\sqrt{2}a_p \times \sqrt{2}a_p \times 2a_p$	Orthorhombic	$Pbnm$
Rock-Salt	$2a_p \times 2a_p \times 2a_p$	Cubic	$Fm\bar{3}m$
	$\sqrt{2}a_p \times \sqrt{2}a_p \times 2a_p$	Monoclinic	$P2_1/n$
Layered	$2a_p \times 2a_p \times 2a_p$	Monoclinic	$P2_1/m$

3.2.2 Cation Ordering

The cation order or disorder has a very important role in defining the symmetry of the crystalline structure and also affects the physical properties. When two cations occupying the same site type differ significantly in size or coordination preferences, they usually assume an ordered arrangement. Ordering of B-sites in $ABB'X_6$ double perovskites is very frequently observed, typically with a rock-salt order[14,15]. In contrast, A-site ordering in $AA'BB'O_6$ doubly ordered perovskites is relatively rare and based on cationic differences. This thesis is focused on this type of perovskites. In the next examples, the majority of doubly ordered perovskites entails (001) layering[16–18] of the different *A* and *A'* cations with *P4/mmm* symmetry[16,17] and these organization of cations is having only recently been explained[14,17]. In order to explain the *A*-site ordering, it is useful to focus on the anion environment. As illustrated in Figure 6, the layer order of A cations creates three distinct and unique position for the anions. The anion *1* is coplanar to the cations *A* and the anion *2* is in the plane of cation *A'*. As said previously, for a layered order it is necessary a difference in size and/or oxidation state of the *A* and *A'* cations.

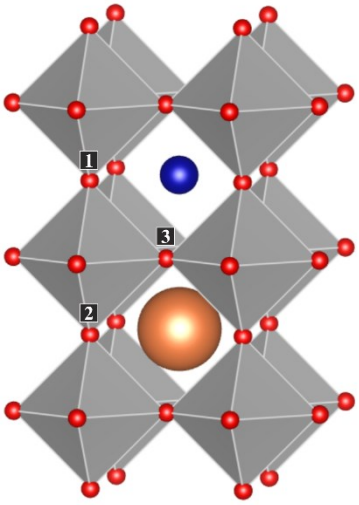

Fig. 6: Order of A-cations implying different anionic environments, in blue cation A, in orange cation A' and in red anion X.

For example, if the *A* is smaller with respect to *A'*, the coplanar (*1*) and (*2*) anions can not shift in reaction to the size difference because any shift of anions to *A*-site or *A'*-site would elongate the distance with the other three equivalent *A*-site cations. The other anions (*3*) are between the layer *A* and *A'* and can shift towards the smaller cation to reduce reticular strains. Hence, this symmetry is favoured because *2/3* of the anions are in relative free position and able to adjust to the size difference of cations and only *1/3* cannot. In a much rare case, *A* cations adopt a rock-salt arrangement, wherein every anion is between two different *A* and *A'* cations. In this configuration all the anions are blocked in their positions and unable to move towards smaller cation, then, impotent to reduce any reticular strains caused by the size difference of *A* and *A'*. The rock-salt disposition has a *Fm-3m* symmetry, the anions occupy Wyckoff site 24*d* ($^1/_4$,0,0), which is a special position and prevents any anion movement.

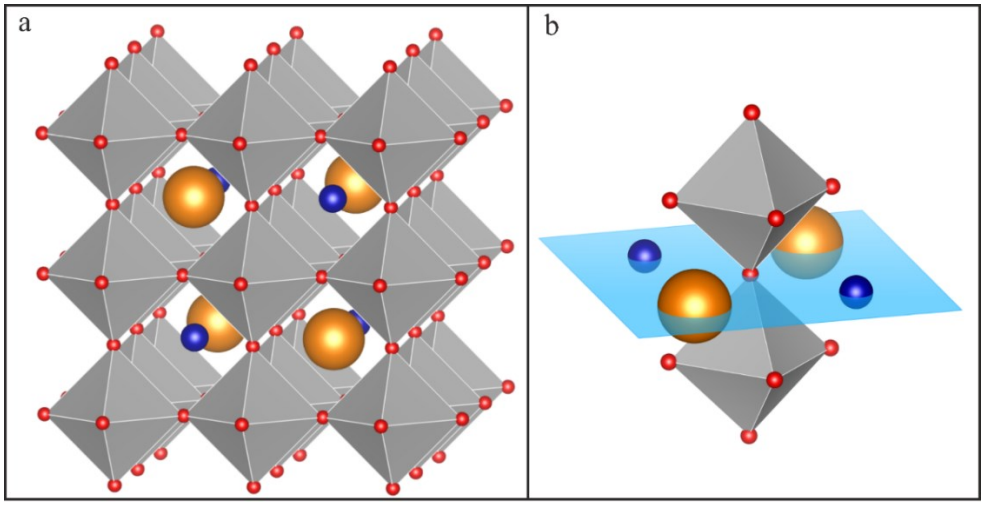

Fig. 7: The rock salt sorting of the A-site cations produces a chemical neighbourhood for the anions that are surrounded by two cations A and A'(a); in (b) an isolated anion is displayed to show the closest cations.

If one considers a layer disposition of site *B,* again the anions are blocked in special positions and unable to react to dimensional differences between *B*-site cations (figure 8). 2/3 of the anions in this lattice are coplanar to the *B*-site cations are blocked and only *1/3* of the anions can move.

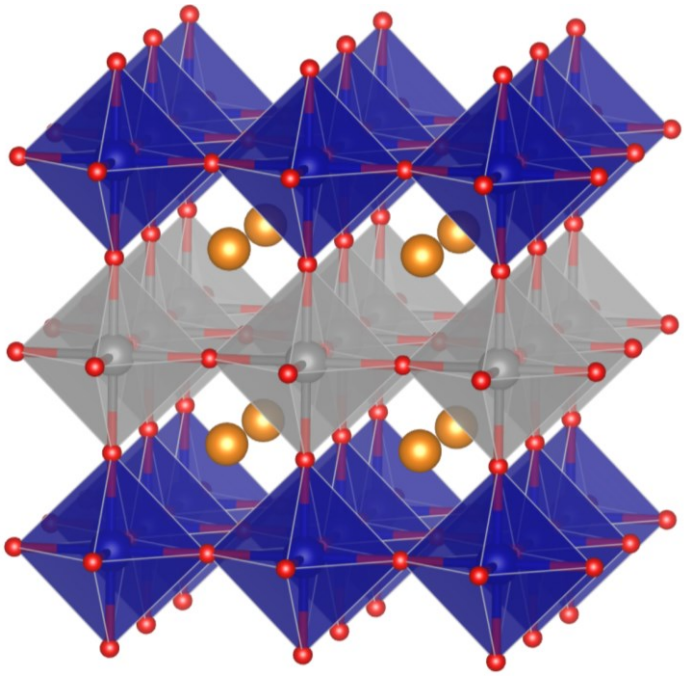

Fig. 8: Doubly orderer perovskite with layered order for cations B and B ' having a single ion in the A-site.

Instead, for the rock-salt-type arrangement of *B*-site cations, all anions are between *B* and *B'* and in this disposition the anions can move toward the smaller cation. Also, in this arrangement we have a *Fm-3m* symmetry, the anions occupy Wyckoff site $24e$ $(x,0,0)$ positions that allow movements towards the different cations.

All these disquisitions on "size problems" explain not only the choice between rock-salt ordering or layer ordering in *A*- and *B*-site in doubly ordered perovskites, but also the great difference in frequency between the two cationic order. The *A*-site layered order is better respect to its rock-salt counterpart, but the *1/3* of the anions are in unstable positions.

As explained above without a mechanism such as cationic or anionic vacancies or octahedral tilt, we cannot have any cationic order unless the lattice has a *B* cation capable of undergoing a Jahn-Teller distortion.

The ordering of the site A, to date, has been rarely observed and it is associated to several complications. For example, two compounds with different *A*-site order $NaBaLiNiF_6$[19] and $Na_2BaFe_4F_{12}$[13] and long-range rock-salt order and one with short-range order $PbCaTi_2O_6$[14,20] have been reported. Columnar type arrangements are also very rare, but two examples, $(CaCu_3)Ti_4O_{12}$ and $(CaFe)Ti_2O_6$[21,22], have been reported. Interestingly, this last example was obtained by high-pressure synthesis and resulted in one perovskite with an unprecedented $a^+a^+c^-$ tilt system, implying three distinct *A*-sites. The Ca^{2+} cation occupies the tetrahedral sites, the smaller neighbouring site is square planar and is occupied by Fe^{2+}, the tilt of octahedrons is essential for stabilizing this new tilt system. Many doubly ordered perovskites have the tilt system $a^+a^+a^+$ which creates two different *A*-sites: one is large with twelve-fold coordination and the other is smaller with four-fold coordination. In these systems, the order of the *A*-site is driven by the coordination preference and the cation-size. In $(Nd_{2/3-x}Li_{3x})TiO_3$, the ordering consists in layers of *A*-sites occupied by Nd^{3+} and other layers occupied by a mixture of Nd^{3+} and Li^+, and vacancies. The *B*-site is occupied by Ti^{4+} (d^0) cations, a cation suitable for a neighborhood of this type. The occurrence of Li^+ cations in *A*-site is unusual because these cations are small with respect to the *A*-cavity dimension. Large octahedral tilt angles are required to stabilize this dimensional discrepancy, so that Li^+ cations are shifted from the centre position, and their coordination number is reduced from *12* to *4*[23,24]. This site order type is observed also in non-stoichiometric anion-deficient perovskites. A documented example is the cuprate $Ba_2YCu_3O_{7-x}$[25,26], in which the ordering is achieved thanks to the decrement of the coordination number for a fraction of the *A*-sites due to vacancies. The vacancies, the coordination preference and the size difference contribute to stabilize a doubly ordered perovskite.

3.2.3 Twinning in perovskites

Generally, perovskites are affected by diffuse twinning due to the structural transformations occurring during cooling from the high temperatures required for the synthesis of these ceramic compounds. The high temperature phases exhibit cubic or tetragonal symmetry whereas the room temperature structures possess orthorhombic or monoclinic symmetry. Therefore, diffuse twinning occurs passing from high to low symmetry systems. A twinned crystal is a regular aggregate formed by distinct crystals with the same composition linked together with a well-defined mutual orientation. From a crystallographic point of view, a twinned crystal is characterized by symmetry operations that relate all distinct individuals of the composite crystal. The most frequent operations are a *n*-rotation around a zone axis or a reflection in a lattice plane called the twin plane. Three types of twin crystals exist[27]:

- Growth twins accidentally produced during crystal growth.
- Deformation twinning in response to mechanical stress.
- Transformation twins occurring when a high symmetry crystal is cooled down into a structure with a lower symmetry.

The strong twinning of perovskites in mainly related to the octahedra tilting system[28]. In fact, if two tilting arrangements are energetically and geometrically equivalent, several growth directions can occur contributing to hamper the correct symmetry of the crystal structure. In perovskites the growing boundaries are very complex to define, but the boundary must have an intrinsic pseudo-symmetry and coincident sites for the formation of planes with different low-energy composition[29]. If we consider the octahedra of perovskites non-deformable, and which remain unchanged after a topological modification, it is easy to demonstrate that the displacement of the cation *A* and the anion *X* is minimal[29]. In fact, the twinning variants occurring in perovskites are not only linked to the tilt framework (and related symmetry) but is often also accompanied by compositional divergences as in $CaSnO_3$[30], $ThNb_4O_{12}$[31] and $NaLaMgWO_6$[28].

3.2.5 Electric and Magnetic Proprieties of Double Perovskites

The electrical and magnetic properties of $A_2BB'X_6$ and $AABB'X_6$ compounds are mainly defined by the B cations. The electrical properties found for double and doubly ordered perovskites are varied, ranging from metallic to insulating materials. Such variety of the physical properties is conferred by the fact that $2d$, $4d$, $5d$ and even $4f$ transition metals with different oxidation states can be combined within these crystalline structures. Most of the synthesized perovskites have an insulating and semiconductor behavior, with conduction mechanisms that are activated thermally or by small-polaron hopping, or Mott variable-range hopping. Some compounds of this type exhibit an electrical conduction behavior typical of metals with a spin-polarized electron conduction. The compound that has been most studied is Sr_2FeMoO_6[32,33], that has revealed ferrimagnetic, semimetallic characteristics at room temperature and that has also shown a negative magnetoresistive tunnel effect at RT at low magnetic fields, therefore an excellent candidate for technological applications. The tunneling negative magnetoresistive effect (TMR) and the semimetallic character are correlated with each other, in fact the overlap between the d-state of the transition metals and the p-states of the oxygens cause the formation of a conduction down-spin band. This TMR effect is generated by the tunneling effect that occurs between the different crystalline grains of the sample. Thus, a magnetoresistive effect has never been measured in single crystal samples. Other doubly ordered perovskites like $YBaCuFeO_6$[73], featured by high dielectric constant values, low losses and good thermal stability, have been used as insulators. Many compounds of perovskite nature[34,35] have shown very high (even colossal) values of the dielectric constant, but conversely, do not possess the thermal stability and dielectric losses necessary for technological applications.

Ferroelectric compounds are those compounds that possess an intrinsic and permanent charge polarization which can be reversed by an external electric field, known as a switching process and represent a fundamental key-material for several applications in electronics. One of the possible applications are non-volatile memories such as Ferroelectric Random-Access Memory (FeRAM), in which the information stored is a function of the sign of the electrical polarization. For this application, some perovskites of lead and zirconium titanate $PbZr_xTi_{1-x}O_3$ PZT have already been used[36]. In this perovskite, the ferroelectric ordering is due to the polarizability of the atoms and the second order Jahn-Teller effect. In the case of the PZT, the cations of the B site (Ti^{4+} and Zr^{4+}) are both d^0 and shifted respect to the center of the coordination octahedron and combined with the high polarizability of the lead ions, confer ferroelectric properties. The lead-based double perovskites $Pb_2BB'O_6$, attracted much attention because this class of compounds generally have shown antiferroelectric transition temperatures above the room temperature. The double order involving the metals B and B ' in the structure greatly influence the ferroelectric properties. In samples in which the B and B' atoms are disordered there is a relaxor behavior[37–39], while the ordered samples show classic antiferroelectric behaviors[40,41]. Instead, the electric and magnetic properties in double perovskites are very complex and varied, because of the structural flexibility and the very numerous combinations of paramagnetic cations on sites A and B, that produce magnetic states ranging from the classic antiferromagnetic, ferromagnetic arrangements up to ferrimagnetic and glassy states[40,42–45]. Since the dual nature of the perovskite lattice, the super-exchange topology is complex. If in the structure there is only one paramagnetic atom in site B as in the case of the A_2BWO_6 type, there are two possible super-exchange paths that connect the magnetic atoms, which are however competing with each other causing a frustrated character to the system[45]. If two distinct paramagnetic atoms B and B' are present in the structure, each B atom is surrounded by six B' atoms and the shortest exchange path is B-O-B'.

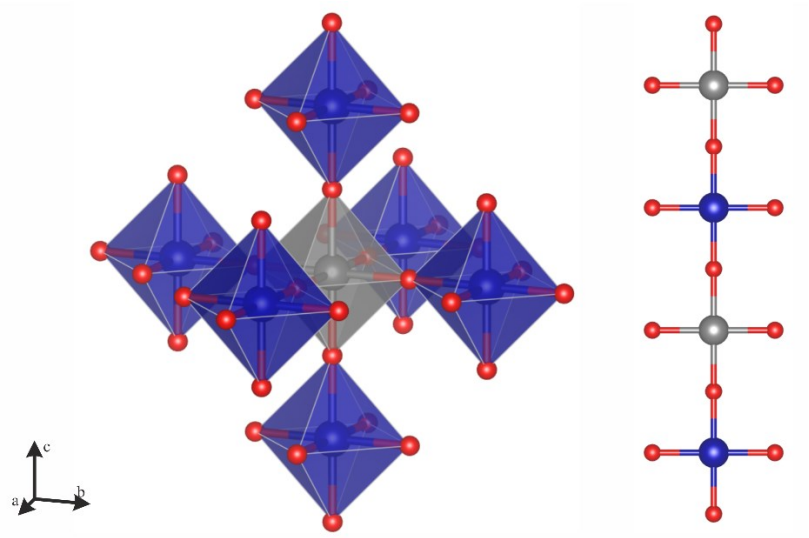

Fig. 9: View of the structure of doubly ordered perovskite in which are present two distinct paramagnetic atoms on the left. View of the O-B-O-B'chain along c axis on the right.

This interaction depends on the relative energy between the B and B 'orbitals, and this overlap may be competing with the B-O-B'-O-B interaction which may weaker the first interaction and become stronger. In any case, the possibility of having different ways of ordering in the structure of the metals d, allows to have different types of interaction. Generally, oxides with a perovskite structure are antiferromagnetic due to the rules of Goodenough-Kanamori[46,47], which state that ferromagnetic interactions are present only with combinations of half-filled orbitals with empty or full orbitals. The properties of doubly ordered perovskites are also influenced by the nature of the A and A' cations. These cations produce a reticular distortion caused by their size; a small ion in fact induces inclinations of the BO_6 octahedra, modifying the overlap between the B cation and the orbitals of the oxygens. In conclusion, doubly ordered perovskites possess numerous and different electrical and magnetic properties that can be simultaneously present in the same phase. Therefore, the possibility of having magnetic and electrical properties at the same time as a function of chemical substitutions, makes perovskites the ideal candidates for multiferroism.

One of the most promising aspects concerning doubly ordered perovskites is represented by the chance to induce a non-conventional ferroelectric polarization, indicated as “hybrid improper ferroelectricity” (HIF)[48–51]. This ability in perovskites is related to the coupling of non-polar modes, introduced from the reciprocal rotations and tilting of the BO_6 octahedra of the framework. These rotations induce a polar mode as a secondary order and the coupling of the free energy of the system is a trilinear invariant between the parameters related to the distortions (rotations and inclinations). Examples of HIF have been found in perovskites $AA'BB'O_6$ that possess heterovalent metals and sorted in site A.[51,52] Following these first discoveries, numerous computational works and predictive studies on the symmetry have been carried out. Such theoretical studies established that the most effective chemical tool for having a ferroelectric polarization through the HIF mechanism[19–21] is a cationic ordering of sites A and/or B. The most promising ordering to make perovskite an HIF candidate is the rock salt distribution of cations B and B' and a layered intercalation of two cations A and A'. These doubly ordered perovskites with general formula $AA'BB'O_6$ have been synthesized with an enormous chemical variety of combinations of cations[53,54].

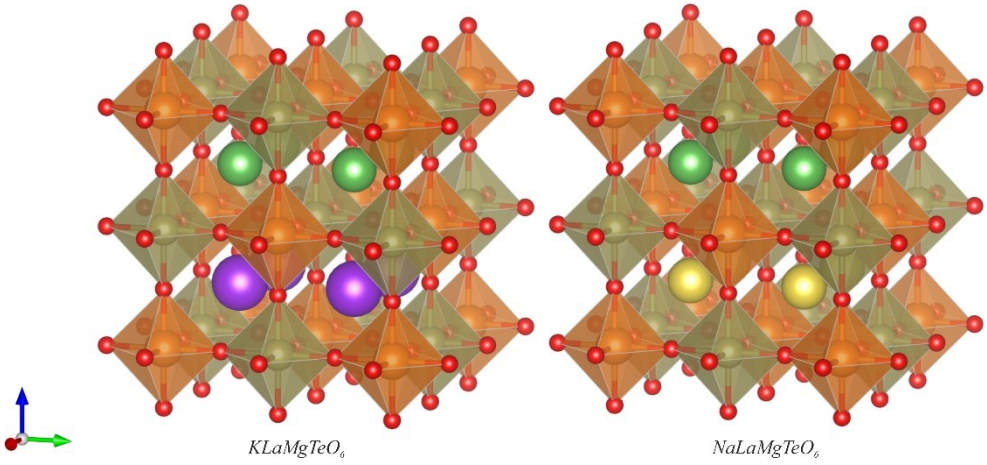

Fig. 10: Example of doubly ordered perovskite with promising HIF effect left: $KLaMgTeO_6$ right:$NaLaMgTeO_6$.

In these perovskites the cations B and B' are often transition metals that can undergo a second order Jahn-Teller distortion, such as the cation W^{6+} and metals of the period 3d such as Mn, Fe, Co and Ni[55–58]. The d-metal exchange coupling mediated by the presence of d^0 W^{6+} ions defines weak antiferromagnetic interactions with Neel temperatures usually below 15 K[21]. Research has resulted in a synthesis of doubly ordered phases with potential mutiferroic properties consisting of cation A=Na^+ or K^+, A'= RE^{3+} and B = Co^{2+}, Fe^{2+}, Ni^{2+} [59]. Perovskites which are made up of $NaA'BWO_6$ have a $P2_1$ monoclinic polar symmetry with an $a^-a^-c^+$ tilt pattern that allows for the HIF[60–63] mechanism. Young et al.[71], for the phase $NaYCoWO_6$ defines as a key factor of the electrical polarizability the great difference of the atomic radii between the cations A and A', thus confirming that the electrical polarization is linked to a HIF mechanism and is supported by the large octahedral tilting due to the smaller atomic size of the cations A'[18]. On the contrary, compounds with nature $AA'BWO_6$ crystallize in a symmetrical center group *C2/m* with a tilting system $a^0b^-c^0$ and a supercell $\sqrt{2}a_p*\sqrt{2}a_p*2a_p$ (with $a_p \sim 3.9$ Å). Some compositions in which the A/A' cations are sodium and lanthanum, respectively, possess a C-centered crystalline structure at room temperature and a symmetry $P2_1$ at low temperature. This change in symmetry is related to the change of the positions of the anions and rearrangement of the tilt pattern[59]. Also, from electron diffraction (ED) and HREM studies on different phases ($NaLaMgWO_6$, $NaLaCoWO_6$, $KLaMnWO_6$ and $NaCeMnWO_6$) revealed a C-centered monoclinic structure with incommensurate structural modulation. The HREM images present an unusual nanoscale contrast, which have been explained with incommensurate modulated twin domains[64–66]. Indeed, the 1D modulation contained by a $12a_px2a_px2a_p$ superstructure has been linked to an inhomogeneous distribution of A/A' cations[64], and the checkerboard contrast difference in HREM was interpreted as a different distribution of the Na and La content[64,67]. Other authors, on the other hand, link the structural modulation in $AA'BWO_6$ perovskites to the topological distortion following a shift or change in inclination of the octahedra and a periodic twinning[66,68,69]. Therefore, the origin of the modulation in these systems is still controversial and the description of these incommensurate structures have yet to be fully

defined. The complete definition of the incommensurable modulated structures of doubly ordered perovskites is important because:

- Structural modulation could remove centrosymmetric symmetry and induce local distortions giving the opportunity to measure an electrical polarizability or to obtain dipolar arrangements.
- Structural information may be able to understand the transition from an incommensurate C-centered modulated structure and the polarizable $P2_1$ phase observed very often for doubly ordered perovskites.

For these reasons, in this thesis the doubly ordered perovskite $NaLaCoWO_6$ was synthesized, and the incommensurate modulated structure was studied with the combined use of different diffraction experiments.

3.2.5 Background $NaLaCoWO_6$

In this thesis two different doubly ordered perovskites, which showed different physical properties, were examined with electron diffraction experiments. The first one is $NaLaCoWO_6$ perovskite, which has been synthesized for the first time by Arillo et al. in *1997*. Initially the structure was determined in the $P2_1/m$ symmetry group with β closer to *90°* and lattice parameters $\sqrt{2a_p} * \sqrt{2a_p} * 2a_p$[70]. However, the refinement on the SXRD was not satisfactory with the proposed spacegroup, therefore, following theoretical analysis and additional investigations, the symmetry group was changed to *C2/m*. This change, which led to a more accurate refinement of diffraction patterns, implies a different choice of the unit-cell and tilt scheme. In fact, for $P2_1/m$, the unit-cell dimensions are $\sqrt{2a_p} * \sqrt{2a_p} * 2a_p$ and the tilting scheme is $a^-a^-c^0$, while for *C2/m* the unit-cell dimensions are $2a_p * 2a_p * 2a_p$ and the tilting scheme is $a^0b^-c^0$[71]. In *C2/m* symmetry, the *A*/*A'* cation have layers ordering, *B*/*B'* cation have rock-salt ordering and a second order Jahn-Teller distortion effects the site *B'*[17]. More specifically, the W^{6+} cations tend to move towards the *Na* layers, while *Co* remains at the centre of the octahedral coordination with a specific tilting scheme. For this compound an approximate superstructure was conceived from electron diffraction and high-resolution electron micrographs. Indeed, in this model, the structural modulation is not accounted and the crystallographic description of such complex modulated structure still unknown. In previous studies a regular stripelike contrast in HRTEM images with a $12a_p$ periodicity, and the sharp satellite reflections in electron diffraction patterns have been observed. This superstructure vanishes at low temperature, and being a reversible first-order transition characterized by a large thermal hysteresis, it is restored well above the transition temperature[72]. Nevertheless, the origin of this long-range order has never been explained: it has been argued that this complex structural condition could be due to an occupational order (chemical order) or an ionic displacement (change of tilting order or oxygen displacement) or a combination of both. Indeed, the actual research work is focused on the crystal study of the long-range ordered superstructure in such doubly

perovskites by adopting electronic diffraction and other diffraction techniques. This study will provide fundamental implications regarding the physical properties of this material.

3.2.6 Background $NaLaMgWO_6$

The second doubly ordered perovskite has Mg in site B, and it is characterized by photoluminescent properties. The first synthesis of this phase was carried out by Sekiya[74] et al. in *1984*. The crystal structure of this phase has been resolved in the *C2/m* symmetry group with cell $\sqrt{2a_p} * \sqrt{2a_p} * 2a_p$[70] and a β close to 90°. The rock salt order for cations B and B' and a layered order for ions A and A' was immediately shown[1]. This perovskite is doped with different rare-earths (such as Eu^{3+}, Sm^{3+} or Nd^{3+}) or other optically active ions to change and define its photolectric characteristics[75]. It was demonstrated the possibility of building a prototype light-emitting diode (LED) device using the combination of a $NaLaMgWO_6$: Mn^{4+}. In fact, it has been shown that this material under an excitation with a wavelength of 342 nm is able to emit at a far-red wavelength of approximately 700 nm with an efficiency of more than 60%[76]. This property can be exploited for the construction of new emitting devices. In the last year a new series of phosphors have been synthesized with the Sol-gel method, this series consists of $NaLaMgWO_6$:Bi^{3+}/Mn^{4+}/Pr^{+3}. in particular, it has been shown that depending on the atom used as an impurity[77], the photoluminescent characteristics can be enormously changed. In fact, the incorporation of the Bi^{3+} ion increases the photoluminescence intensity of such phosphors under blue-light excitations. This result pave the way for materials that have a dual function: illumination for plant growth and simultaneous temperature detection with very high sensitivity[77]. In these studies, the crystalline structure of these new materials has not been completely determinate: in literature the crystallographic studies of this phase report the presence of a structural modulation. A first microscopy study reports the presence of the spontaneous formation of compositionally modulated stripes, which binds to areas La-rich and La-poor[78]. Assuming, that the observation of the separation of the two phases offers the possibility to design nanostructured and self-assembled materials inside of the

perovskitic framework[78]. Additional microscopy studies on this perovskite revealed the presence of antiphase boundaries, orientation domain structures and a compositional modulation, but the authors attribute it to areas where there is an excess of Na/Mg and in others a deficiency of Na/Mg[79]. Therefore, the controversial interpretations reported in the literature propose us to carry out a crystallographic study on the origin of the structural modulation. To establish whether the modulation is occupational or positional, a series of compounds with a different La/Na balance was synthetized and analyzed.

3.3 References

1. Blasse, G. New compounds with perovskite-like structures. *Journal of Inorganic and Nuclear Chemistry* **27**, 993–1003 (1965).

2. Nielsen, P. K., Hemmingsen, C., Friis, S. U., Ladefoged, J. & Olgaard, K. Comparison of straight and curled Tenckhoff peritoneal dialysis catheters implanted by percutaneous technique: A prospective randomized study. *Peritoneal Dialysis International* **15**, 18–21 (1995).

3. J. Bartel, C. Sutton, B. Goldsmith, L.M. Ghiringhrlli M. Scheffler_New tolerance factor to predict the stability of perovskite oxides and halides. *Science Advances* **5**, 1–10 (2019).

4. Anderson, M. T., Greenwood, K. B., Taylor, G. A. & Poeppelmeier, K. R. B-cation arrangements in double perovskites. *Progress in Solid State Chemistry* **22**, 197–233 (1993).

5. Teraoka, Y., Wei, M. D. & Kagawa, S. Double perovskites containing hexavalent molybdenum and tungsten: Synthesis, structural investigation and proposal of a fitness factor to discriminate the crystal symmetry. *Journal of Materials Chemistry* **8**, 2323–2325 (1998).

6. Glazer, A. M. The classification of tilted octahedra in perovskites. *Acta Crystallographica Section B Structural Crystallography and Crystal Chemistry* **28**, 3384–3392 (1972).

7. Miller G. F. and Musgrave M. J. P. The Royal Society is collaborating with JSTOR to digitize, preserve, and extend access to Proceedings of the Royal Society of London. Series A, Mathematical and Physical Sciences. *Proceedings of the Royal Society of London A* **236**, 352–383 (1956).

8. Kunz, M. & David Brown, I. Out-of-center distortions around octahedrally coordinated d^0 transition metals. *Journal of Solid-State Chemistry* vol. 115 395–406 (1995).

9. Zhang, H. M., Shimizu, Y., Teraoka, Y., Miura, N. & Yamazoe, N. Oxygen sorption and catalytic properties of $La_{1-x}Sr_xCo_{1-y}Fe_yO_3$ Perovskite-type oxides. *Journal of Catalysis* **121**, 432–440 (1990).

10. Takahashi, T. & Iwahara, H. Ionic conduction in perovskite-type oxide solid solution and its application to the solid electrolyte fuel cell. *Energy Conversion* **11**, 105–111 (1971).

11. Tofield, B. C. & Scott, W. R. Oxidative nonstoichiometry in perovskites, an experimental survey; the defect structure of an oxidized lanthanum manganite by powder neutron diffraction. *Journal of Solid State Chemistry* **10**, 183–194 (1974).

12. Teraoka, Y., Yoshimatsu, M., Yamazoe, N. & Seiyama, T. Oxygen-Sorptive Properties and Defect Structure of Perovskite-Type Oxides. *Chemistry Letters* **13**, 893–896 (1984).

13. López, M. L., Veiga, M. L. & Pico, C. Cation ordering in distorted perovskites (MLa)(MgTe)O_6, M = Na, K. *Journal of Materials Chemistry* **4**, 547–550 (1994).

14. King, G. & Woodward, P. M. Cation ordering in perovskites. *Journal of Materials Chemistry* **20**, 5785 (2010).

15. Howard, C. J., Kennedy, B. J. & Woodward, P. M. Ordered double perovskites - A group-theoretical analysis. *Acta Crystallographica Section B: Structural Science* **59**, 463–471 (2003).

16. Davies, P. K., Wu, H., Borisevich, A. Y., Molodetsky, I. E. & Farber, L. Crystal Chemistry of Complex Perovskites: New Cation-Ordered Dielectric Oxides. *Annual Review of Materials Research* **38**, 369–401 (2008).

17. Knapp, M. C. & Woodward, P. M. A-site cation ordering in AA′BB′O_6 perovskites. *Journal of Solid State Chemistry* (2006).

18. Davies, P. K. Cation ordering in complex oxides. *Current Opinion in Solid State and Materials Science* **4**, 467–471 (1999).

19. Duncan. Crystal Structure and NMR Studies of a Cubic Perovskite. *Japanese Society of Biofeedback Research* **19**, 463–466 (1992).

20. King, Grace Goo, E., Yamamoto, T. & Okazaki, K. Crystal Structure and Defects of Ordered ($Pb_{1-x}Ca_x$)TiO_3. *Journal of the American Ceramic Society* **71**, 454–460 (1988).

21. Leinenweber, K. & Parise, J. High-pressure synthesis and crystal structure of $CaFeTi_2O_6$, a new perovskite structure type. *Journal of Solid State Chemistry* vol. 114 277–281 (1995).

22. Bochu, B. *et al.* Synthèse et caractérisation d'une série de titanates perovskites isotypes de [$CaCu_3$](Mn_4)O_{12}. *Journal of Solid State Chemistry* **29**, 291–298 (1979).

23. Sommariva, M. & Catti, M. Neutron diffraction study of quenched $Li_{0.3}La_{0.567}TiO_3$ lithium ion conducting perovskite. *Chemistry of Materials* **18**, 2411–2417 (2006).

24. Varez, A., Fernández-Ḍaz, M. T., Alonso, J. A. & Sanz, J. Structure of fast ion conductors $Li_{3x}La_{2/3-x}TiO_3$ deduced from powder neutron diffraction experiments. *Chemistry of Materials* **17**, 2404–2412 (2005).

25. Corey, E. J. & Su, W. Oxygen-vacancy ordering in the $Ba_2YCu_3O_{7-x}$ Superconducting System. *Tetrahedron Letters* **28**, 5241–5244 (1987).

26. Chaillout, C., Capponi, J. J., Chenavas, J. & Cdex, G. Oxygen vacancy ordering and non-stoichiometry in the $Ba_2YCu_3O_{7-x}$ superconductors. **22**, 1685–1693 (1987).

27. Giacovazzo, C. *et al.* Fundamentals of Crystallography. *Fundamentals of Crystallography* (2013).

28. King, G., Garcia-Martin, S. & Woodward, P. M. Octahedral tilt twinning and compositional modulation in $NaLaMgWO_6$. *Acta Crystallographica Section B: Structural Science* **65**, 676–683 (2009).

29. Segall, R. L., Barry, J. C. & Hutchison, J. L. Z. Kristaliogr. 127, 386-387 (1985).

30. Vegas, a., Vallet-Regí, M., González-Calbet, J. M. & Alario-Franco, M. a. The $ASnO_3$(A=Ca,Sr) Perovskites. *Acta Crystallographica Section B Structural Science* **42**, 167–172 (1986).

31. Alario-franco, B. Y. M. A. & A-cation-deficient, T. Structural Studies on A-Cation-Deficient Perovskite-Related Phases. $ThNb_4O_{12}$. Thorium/Vacancy Ordering in Slow-Cooled Samples. 177–186 (1982).

32. Kobayashi, K.-I., Kimura, T., Sawada, H., Terakura, K. & Tokura, Y. Room-temperature magnetoresistance in an oxide material with an ordered double-perovskite structure. *Nature 1998 395:6703* **395**, 677–680 (1998).

33. Sarma, D. D., Mahadevan, P., Saha-Dasgupta, T., Ray, S. & Kumar, A. Electronic structure of Sr_2FeMoO_6. *Physical Review Letters* **85**, 2549–2552 (2000).

34. Yan-Qing, T., Meng, Y. & Yong-Mei, H. Structure and colossal dielectric permittivity of Ca_2TiCrO_6 ceramics. *Journal of Physics D: Applied Physics* **46**, 015303 (2012).

35. Yang, W. Z., Mao, M. M., Liu, X. Q. & Chen, X. M. Structure and dielectric relaxation of double-perovskite La_2CuTiO_6 ceramics. *Journal of Applied Physics* **107**, 124102 (2010).

36. Kim, K. & Lee, S. Integration of lead zirconium titanate thin films for high density ferroelectric random-access memory. *Journal of Applied Physics* **100**, 051604 (2006).

37. Ivanov, S. A., Eriksson, S., Tellgren, R. & Rundlöf, H. Neutron powder diffraction study of the magnetoelectric relaxor $Pb(Fe_{2/3}W_{1/3})O_3$. *Materials Research Bulletin* **39**, 2317–2328 (2004).

38. Malibert, C. *et al.* Order and disorder in the relaxor ferroelectric perovskite (PSN): comparison with simple perovskites. *Journal of Physics: Condensed Matter* **9**, 7485 (1997).

39. Perrin, C. *et al.* Influence of B-site chemical ordering on the dielectric response of the $Pb(Sc_{1/2}Nb_{1/2})O_3$ relaxor. *Journal of Physics Condensed Matter* **13**, 10231–10245 (2001).

40. Ivanov, S. A., Nordblad, P., Mathieu, R., Tellgren, R. & Ritter, C. Structural and magnetic properties of the ordered perovskite Pb_2CoTeO_6. *Dalton Transactions* **39**, 11136–11148 (2010).

41. Blasco, J., Merino, R. I., García, J. & Sánchez, M. C. Properties and phase transition of the ordered perovskite Pb_2MnWO_6. *Journal of Physics Condensed Matter* **18**, 2261–2271 (2006).

42. Azad, A. K., Eriksson, S. G., Eriksen, J. & Rundlöf, H. Magnetic ordering of Fe in $Sr_{2-x}Ba_xFeWO_6$ (x=0.0,0.33,0.67,1.00) studied by neutron powder diffraction. *Journal of Magnetism and Magnetic Materials* **272–276**, 771–773 (2004).

43. Dass, R. I. & Goodenough, J. B. Multiple magnetic phases of span class. *Physical Review B* **67**, 014401 (2003).

44. Ritter, C. *et al.* Structural and magnetic properties of double perovskites AA′FeMoO$_6$ (AA′ = Ba_2, BaSr, Sr_2 and Ca_2). *Journal of Physics Condensed Matter* **12**, 8295–8308 (2000).

45. Coomer, F. C. & Cussen, E. J. Structural and magnetic properties of Ba_2LuMoO_6: A valence bond glass. *Journal of Physics Condensed Matter* **25**, (2013).

46. Goodenough, J. B. Theory of the role of covalence in the perovskite-type manganites [La,M(II)]MnO_3. *Physical Review* **100**, 564–573 (1955).

47. Kanamori, J. Superexchange interaction and symmetry properties of electron orbitals. *Journal of Physics and Chemistry of Solids* **10**, 87–98 (1959).

48. Khalyavin, D. D. *et al.* Emergent helical texture of electric dipoles. *Science* **369**, 680–684 (2020).

49. Hayashida, T., Kimura, K., Urushihara, D., Asaka, T. & Kimura, T. Observation of Ferrochiral Transition Induced by an Antiferroaxial Ordering of Antipolar Structural Units in $Ba(TiO)Cu_4(PO_4)_4$. *Journal of the American Chemical Society* **143**, 3638–3646 (2021).

50. Jin, S., O'Bryan, H. M., Tiefel, T. H., McCormack, M. & Rhodes, W. W. Large magnetoresistance in polycrystalline La–Y–Ca–Mn–O. *Applied Physics Letters* **66**, 382 (1998).

51. Hwang, H. Y., Cheong, S. W., Radaelli, P. G., Marezio, M. & Batlogg, B. Lattice effects on the magnetoresistance in doped $LaMnO_3$. *Physical Review Letters* **75**, 914–917 (1995).

52. Schiffer, P., Ramirez, A. P., Bao, W. & Cheong, S. W. Low temperature magnetoresistance and the magnetic phase diagram of $La_{1-x}Ca_xMnO_3$. *Physical Review Letters* **75**, 3336–3339 (1995).

53. Zuo, P., Darie, C., Colin, C. v. & Klein, H. Investigation of the Structure of the Modulated Doubly Ordered Perovskite $NaLaCoWO_6$ and Its Reversible Phase Transition with a Colossal Temperature Hysteresis. *Inorganic Chemistry* **58**, 81–92 (2019).

54. López, M. L., Veiga, M. L. & Pico, C. Cation ordering in distorted perovskites $(MLa)(MgTe)O_6$, M = Na, K. *Journal of Materials Chemistry* **4**, 547–550 (1994).

55. Chan, T. S., Liu, R. S., Hu, S. F. & Lin, J. G. Structure and physical properties of double perovskite compounds Sr_2FeMO_6 (M = Mo, W). *Materials Chemistry and Physics* **93**, 314–319 (2005).

56. Manoun, B., Igartua, J. M., Gateshki, M. & Saxena, S. K. High-pressure study of the Sr_2CoWO_6 ordered double perovskite tungstate oxide. *Journal of Molecular Structure* **888**, 244–252 (2008).

57. Bijelić, J. *et al.* Nanocrystalline Antiferromagnetic High-κ Dielectric Sr_2NiMO_6 (M = Te,W) with Double Perovskite Structure Type. *Molecules 2020, Vol. 25, Page 3996* **25**, 3996 (2020).

58. Blasco, J., Merino, R. I., García, J. & Sánchez, M. C. Properties and phase transition of the ordered perovskite Pb2MnWO6. *Journal of Physics: Condensed Matter* **18**, 2261 (2006).

59. King, G., Thimmaiah, S., Dwivedi, A. & Woodward, P. M. Synthesis and Characterization of New $AA'BWO_6$ Perovskites Exhibiting Simultaneous Ordering of A-Site and B-Site Cations.

60. Shankar P. N. *et al.* A-Site and B-Site Cation Ordering Induces Polar and Multiferroic Behavior in the Perovskite $NaLnNiWO_6$ (Ln = Y, Dy, Ho, and Yb). *Chemistry of Materials* **32**, 5641–5649 (2020).

61. Shankar P. N. *et al.* Structural, Magnetic, and Electrical Properties of Doubly Ordered Perovskites $NaLnNiWO_6$ (Ln = La, Pr, Nd, Sm, Eu, Gd, and Tb). *The Journal of Physical Chemistry C* **125**, 6749–6757 (2021).

62. De, C. & Sundaresan, A. Nonswitchable polarization and magnetoelectric coupling in the high-pressure synthesized doubly ordered perovskites. *Physical Review B* **97**, 214418 (2018).

63. Fukushima, T., Stroppa, A., Picozzi, S. & Perez-Mato, J. M. Large ferroelectric polarization in the new double perovskite $NaLaMnWO_6$ induced by non-polar instabilities. *Physical Chemistry Chemical Physics* **13**, 12186–12190 (2011).

64. García-Martín, S., Urones-Garrote, E., Knapp, M. C., King, G. & Woodward, P. M. Transmission Electron Microscopy Studies of $NaLaMgWO_6$: Spontaneous Formation of Compositionally Modulated Stripes. *Journal of the American Chemical Society* **130**, 15028–15037 (2008).

65. Garcia-Martin, S., King, G., Urones-Garrote, E., Nénert, G. & Woodward, P. M. Spontaneous Superlattice Formation in the Doubly Ordered Perovskite $KLaMnWO_6$. *Chemistry of Materials* **23**, 163–170 (2010).

66. Borchani, S. M., Koubaa, W. C. R. & Megdiche, M. Structural, magnetic and electrical properties of a new double-perovskite $LaNaMnMoO_6$ material. *Royal Society Open Science* **4**, (2017).

67. Garcia-Martin, S., King, G., Urones-Garrote, E., Nénert, G. & Woodward, P. M. Spontaneous superlattice formation in the doubly ordered perovskite $KLaMnWO_6$. *Chemistry of Materials* **23**, 163–170 (2011).

68. Ju, H. L. *et al.* Dependence of giant magnetoresistance on oxygen stoichiometry and magnetization in polycrystalline $La_{0.67}Ba_{0.33}MnO_z$. *Physical Review B* **51**, 6143–6146 (1995).

69. García-Martín, S., King, G., Nénert, G., Ritter, C. & Woodward, P. M. The incommensurately modulated structures of the perovskites $NaCeMnWO_6$ and $NaPrMnWO_6$. *Inorganic Chemistry* **51**, 4007–4014 (2012).

70. Arillo, M. A., Pico, C., Gómez, J., Veiga, M. L. & López, M. L. Structural characterization and properties of the perovskite $(NaLa)(MW)O_6$(M=Co, Ni): two new members in the group–subgroup relations for the perovskite-type structures. *Journal of Materials Chemistry* **7**, 801–806 (2002).

71. Colin, C. v. *et al.* Structural Study of a Doubly Ordered Perovskite Family $NaLnCoWO_6$ (Ln = Y, La, Pr, Nd, Sm, Eu, Gd, Tb, Dy, Ho, Er, Yb): Hybrid Improper Ferroelectricity in Nine New Members. *Inorganic Chemistry* **56**, 8478–8489 (2017).

72. Zuo, P., Darie, C., Colin, C. v. & Klein, H. Investigation of the Structure of the Modulated Doubly Ordered Perovskite NaLaCoWO6 and Its Reversible Phase Transition with a Colossal Temperature Hysteresis. *Inorganic Chemistry* **58**, 81–92 (2019).

73. Lai YC, Du CH, Lai CH, Liang YH, Wang CW, Rule KC, Wu HC, Yang HD, Chen WT, Shu GJ, Chou FC. Magnetic ordering and dielectric relaxation in the double perovskite $YBaCuFeO_5$. J Phys Condens Matter. 2017

74. Sekiya, T.; Yamamoto, T.; Torii, Y. Cation Ordering in $(NaLa)(MgW)O_6$ with the Perovskite Structure. **2006**, *57* (7), 1859–1862.

75. Zhang, Y.; Guo, N.; Shao, B.; Li, J.; Ouyang, R.; Miao, Y. Photoluminescence and Optical Temperature Measurement of Mn^{4+}/Er^{3+} Co-Activated Double Perovskite Phosphor through Site-Advantageous Occupation. *Spectrochimica acta. Part A, Molecular and biomolecular spectroscopy* **2021**, *259*.

76 Huang, X.; Liang, J.; Li, B.; Sun, L.; Lin, J. High-Efficiency and Thermally Stable Far-Red-Emitting $NaLaMgWO_6:Mn^{4+}$ Phosphorsfor Indoor Plant Growth Light-Emitting Diodes . *Optics Letters* **2018**, *43* (14), 3305.

77 Wang, M.; Han, Z.; Huang, J.; Liao, J.; Sun, Y.; Huang, H.; Wen, H. Rui. $NaLaMgWO_6:Mn^{4+}/Pr^{3+}/Bi^{3+}$ Bifunctional Phosphors for Optical Thermometer and Plant Growth Illumination Matching Phytochrome P_R and P_{FR}. *Spectrochimica acta. Part A, Molecular and biomolecular spectroscopy* **2021**, *259*.

78 García-Martín, S.; Urones-Garrote, E.; Knapp, M. C.; King, G.; Woodward, P. M. Transmission Electron Microscopy Studies of $NaLaMgWO_6$: Spontaneous Formation of Compositionally Modulated Stripes. *Journal of the American Chemical Society* **2008**, *130* (45), 15028–15037.

79 Li, S.; Gao, Q.; Li, J.; He, X.; Zhang, Q.; Li, C.; Shen, Y.; Gu, L.; Yao, Y.; Wang, Y.; Yu, R.; Duan, X.; Ikuhara, Y. Revealing Antiphase Boundaries and Defects at Atomic Resolution in $NaLaMgWO_6$ Double Perovskites. *Materials Express* **2012**.

4. Structural study of doubly ordered perovskites

The topic of this chapter is the subject of a manuscript submitted to https://arxiv.org/abs/2110.14907

4.1.1 Synthesis of $NaLaCoWO_6$

The synthesis of $NaLaCoWO_6$ compound followed the protocol reported by Borchani et al.[1]. This protocol describes a solid-state reaction which involves mixing in stoichiometric quantities Na_2CO_3, La_2O_3 and $CoWO_4$ coumpounds For a better synthesis, the $CoWO_4$ precursor was freshly synthesized through former solid-state synthesis, which involves mixing stoichiometric quantities of CoO and WO_3 and a heat treatment at 900°C for 8 hours. For the synthesis of perovskite, the reactant oxides, once mixed, are thermally treated at 925°C in air for 6 hours with a heating ramp of 4.5°C/min. Afterwards, the sample was ground and pressed to form a pellet and sintered at a temperature of 950°C with a ramp of 2.5°C/min for 8 hours.

4.1.2 Diffraction Experiments

Precession-assisted 3D ED and energy-dispersive X-ray (EDX) spectroscopy were performed with the Zeiss Libra 120 transmission electron microscope working at 120 kV and equipped with a LaB_6 thermionic source and a Bruker EDX XFlash6T-60 detector at the National Enterprise for nano Science and nano Technology in Pisa. For the electron diffraction collections, samples were ground with an agate mortar, the resulting powder was suspended and sonicated in ethanol and drop-deposited on a carbon coated copper grid. Sequential electron diffraction patterns were collected in nanodiffraction mode with a parallel beam of 150 nm, obtained by selecting a condenser aperture of 5 μm. Data were energy-filtered on the zero-loss peak with an in-column Ω-filter and a slit width of about 20 eV[2]. Patterns were collected in stepwise mode with a protocol explained by Mugnaioli et al.[3]. The precession motion of the electron beam around the optical axis was obtained by a Nanomegas Digistar P1000 device[4]. The semi-aperture of the precession cone was set to 1°. The angular collection range of 3D ED data was up to 120 degrees, with steps of 1°. After each tilt step, in order to check the crystal

movements a STEM image was taken and the electron beam as repositioned back in the same point of the crystal. Diffraction patterns were recorded by an ASI Timepix single-electron detector[5]. Cell determination, modulation vector definition and electron diffraction intensity extraction were performed with the PETS 2.0 program on data from thirty different nanocrystals[6]. The X-ray diffraction measurements were performed with a STOE Stadi P diffractometer equipped with Cu-$K\alpha_1$ radiation, a STOE&Cie Johansson monochromator and a Dectris MYTHEN2 1 K detector. The X-ray analyses have been performed in transmission geometry and the sample grounded and placed between sheets of acetate. The time-of-flight (TOF) neutron diffraction data were collected with the cold neutron diffractometer WISH at the ISIS second target station (UK)[7]. The data were focused on 4 detector banks with average 2θ of 154, 121, 90 and 57° each covering 32° of the scattering planes. All structure refinements were performed with the Jana2006 software[8]. The electron diffraction data has been treated within the kinematical approximation. Group theory and symmetry analysis calculations have been performed with the ISOTROPY and ISODISTORT softwares[42]. The free energy invariants have been calculated using the ISOTROPY and INVARIANT softwares[10].

4.1.3 Crystal Analysis

To solve the structure of the $NaLaCoWO_6$, 3D electron diffraction (3D-ED) was collected on thirty different nanocrystals. From the indexing of the main reflections, a monoclinic cell was found with cell parameters: *a=7.83(3)Å b=7.84(2)Å c=7.89(8)Å* e *β=90.16(8)Å*.

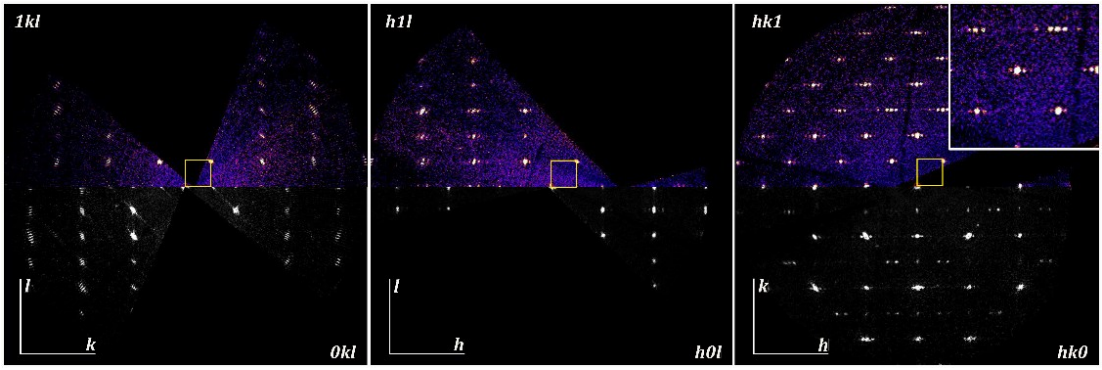

Fig.1: Sections of the reciprocal space of $NaLaCoWO_6$ obtained from a 3D ED data collection. Top in figure in violet, plane of the reciprocal space following the fundamental section. The black zones, devoid of reflections, are areas of the reciprocal space that are not integrated due to the mechanical limitations of the TEM.

From the study of the reconstruction of the reciprocal space (fig.1) the symmetry of the structure was determined. We found there is an alternation of the diffraction columns in the *0kl* and *1kl* plane and in the *h0l* and *h1l* plane, together with a checkerboard pattern in the *hk0* and *hk1* reconstruction. This indicates the extinction rule *h+k=2n,* therefore a *C*-centering lattice, but since there are no other extinction rules, the structure can have three different symmetries *C2*, *Cm* and *C2/m*. It is clearly seen from the reconstruction of the reciprocal space that the main reflections are accompanied by first order satellites along the ***a**** direction, a clear signal that the structure is modulated.

The monoclinic cell of this doubly ordered perovskite has an angle β very close to a right angle. This causes twinning phenomena inside the crystal, which can lead to incorrect evaluations of the extinction rules, and of the definition of the modulation vector (figure 2).

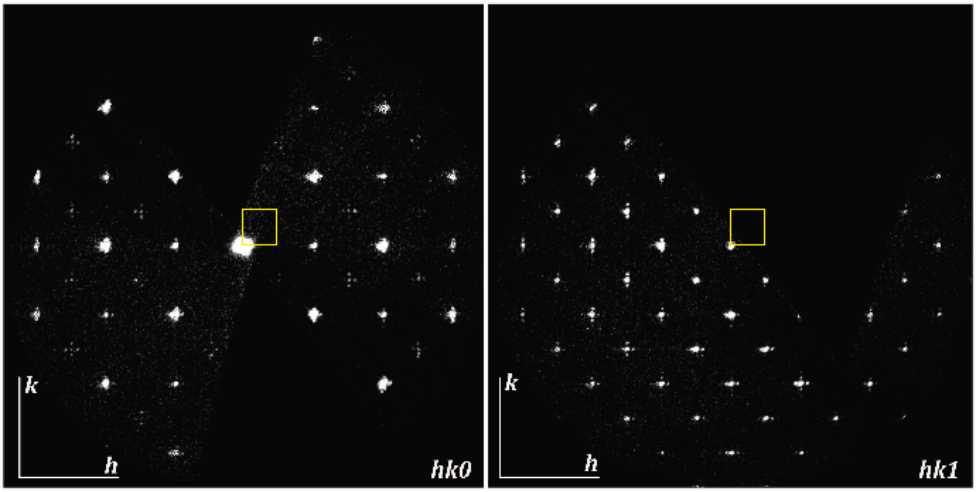

Fig.2: Sections of the reciprocal space of $NaLaCoWO_6$ obtained from a 3D ED data collection. The panels show the typical appearance of hk0 and hk1 direction for a twinned crystal.

4.1.4 Average structure

Without integrating the intensities of the satellites, the average structure of the perovskite was determinate with a *C/2m* symmetry using the SuperFlip algorithm integrated into *JANA2006* software[8]. The resulting doubly ordered perovskite structure consists of two alternating layers between the A (Na^{+1} and La^{+3}) and B (Co^{+2} and W^{+6}) components of the doubly ordered perovskite along the ***b**** direction. The layer composed of Co^{+2} and W^{+6} cations in corner-sharing octahedra has a checkerboard order and is alternated with the layers of the cations Na^{+1} and La^{+3} which are stacked along ***b**** (figure 3).

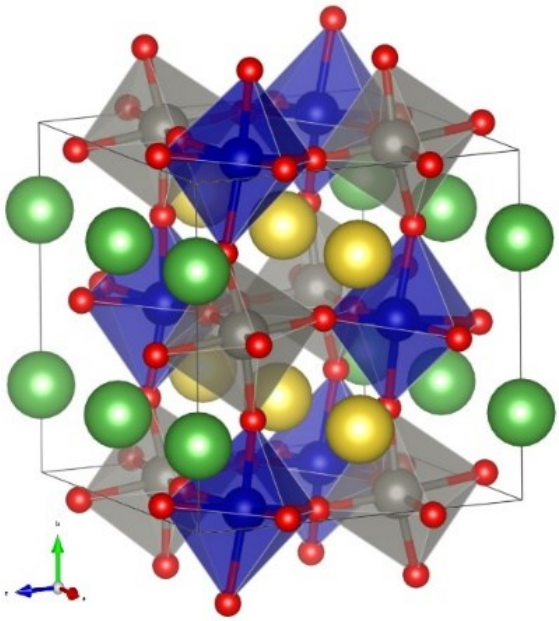

Fig.3: $NaLaCoWO_6$ average structure. with rock salt order for cations B/B' and layer order for A/A'. Co in blue, W in gray, Na in yellow, La in green, oxygens in red.

The octahedra CoO_6^{-8} and WO_6^{-2} have a tilting pattern of $a^0b^-c^0$ in Glazer notation[11]. For the refinement of the average structure, in addition to the electron diffraction data ($wR_{obs}=14.6\%$) a diffractogram collected with transmission geometry and an X-ray source of Copper ($\lambda = 1.54059$ Å) was used.

Using the Rietveld method we obtained a discrepancy factor *(wR_{obs})* of 5.52% and impurities have been defined within the sample (Fig. 4).

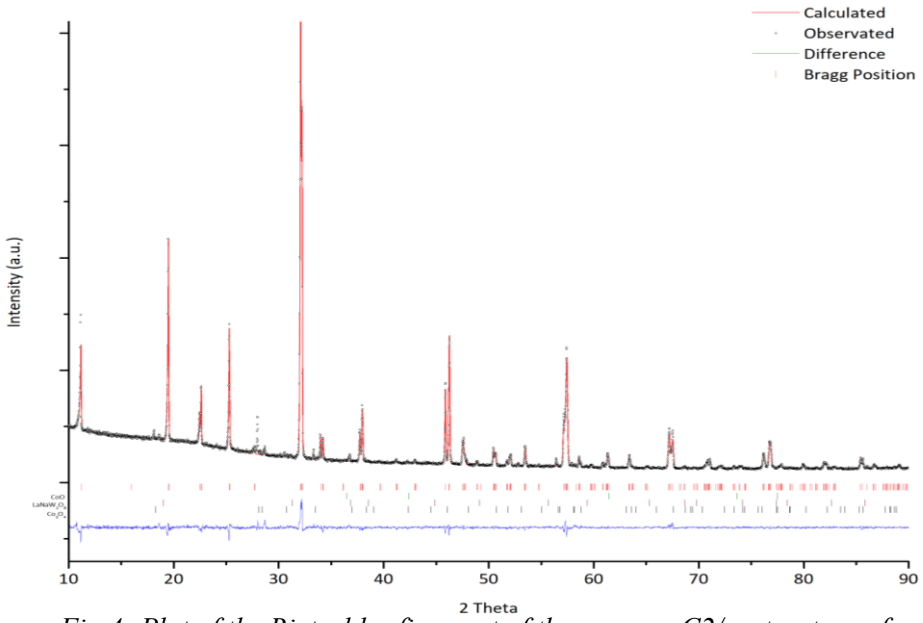

Fig.4: Plot of the Rietveld refinement of the average C2/m structure of $NaLaCoWO_6$ against experimental X-Ray pattern. Observed data (black point), calculated pattern (red line) and difference (blue line) are reported. The thick marks (bottom) indicate the Bragg positions: the main phase in red, in green CoO, in black Co_3O_4 and in violet $LaNaW_2O_8$.

The three impurities defined inside the sample are *CoO, Co_3O_4* and *$LaNaW_2O_8$* due to the synthesis method used[12]. In the X-ray diffractogram satellites are completely confuse with the background, whereas in 3D-ED patterns are clearly visible. This suggests that the modulation is mainly related to the structural distortion involving lighter atoms, like oxygen.

Table1.Structural parameters of the average C2/m structure from the combined refinement of X-ray and 3D-ED data at room temperature.

Atom	*Wyckoff Symbol*	*x*	*y*	*z*	U_{iso}
Na	4h	0.0	0.751(8)	0.5	0.013(3)
La	4g	0.0	0.752(1)	0.0	0.018(1)
Co	4i	0.287(5)	0.0	0.273(2)	0.022(3)
W	4i	0.739(4)	0.0	0.251(7)	0.008(2)
O1	4i	0.992(2)	0.0	0.275(5)	0.038(2)
O2	8j	0.736(5)	0.2562(5)	0.761(6)	0.045(4)
O3	4i	0.512(3)	0.0	0.205(3)	0.007(2)
O4	4i	0.214(3)	0.0	0.990(2)	0.025(8)
O5	4i	0.289(2)	0.0	0.502(5)	0.037(3)

Space group C2/m, Z=4. Unit-cell parameters: a=7.83(3)Å, b=7.84(2)Å, c=7.89(8)Å and β=90.16(8) Å. Discrepancy Factor on electron data: wR_{obs}=14.6%, R_p=13.2%, GOF=12.07. Discrepancy Factor on X-ray data: wR_{obs}=5.52%, R_p=3.68%, GOF=1.82.

4.1.5 Modulated Structure

First of all, the modulation vector ***q*** and the reflection conditions in 4D-space was determined by studying the reciprocal space of the 3D-ED data (fig. 5).

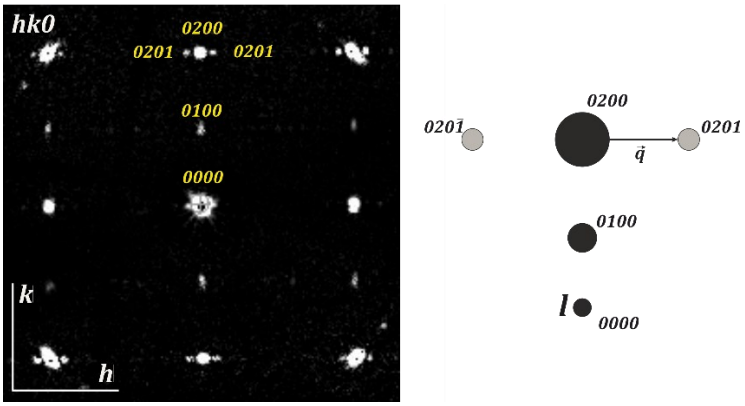

Fig.5: Definition of the modulation vector q

The modulation vector for indexing the satellites has a single component *q=0.172(2)a** and the reflection conditions of the satellites *hklm: h+k=2n* and *h0lm:m=2n* consistent with the superspace group *C2/m(α0γ)0s*. We are therefore in the special case in which the third component of the modulation vector ***q*** is equal to zero. With this information, structural resolution using a superspace approach on a complete 3D-ED data set was attempted. The solution resulting from the Superflip algorithm indicates a large positional modulation of the cations Na^{+1} and La^{+3}, which is inconsistent with the fact that this result would imply the presence of satellites even in the X-ray data which are completely absent.

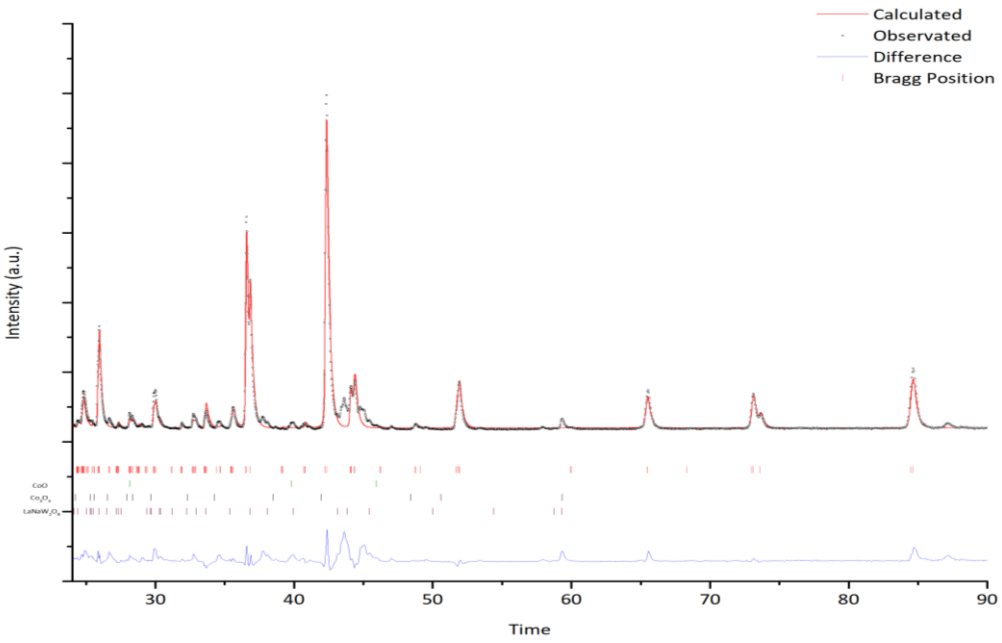

Fig.6: Plot of the Rietveld refinement of the average C2/m structure of $NaLaCoWO_6$ against TOF neutron diffraction data. Observed data (black points), calculated pattern (red line) and difference (blue line) are reported. The thick marks (bottom) indicate the Bragg positions of the main phase in red, in green CoO, in black Co_3O_4 and in violet $LaNaW_2O_8$. The reliability factors are wR_p=5.52%, R_p=3.68%

To disclose the nature of the incommensurate distortions, high resolution neutron diffraction, which is more sensitive to light ions, was carried out at room temperature. First, the average structure found by electron diffraction data was used as starting structure for the neutron diffraction refinement, obtaining an excellent agreement (fig.6). The simultaneous refinement of the average structure against with TOF-NPD data and powder x-ray data results in a good fit of the experimental data. During the refinement of the average structure, the thermal atomic parameters (ADPs) were considered anisotropic. The average structural model is featured by elongated anisotropic ADPs for the oxygen positions, suggesting a possible disorder or splitting of these sites. To explain this disorder and obtain reasonable thermal parameters, it was necessary to split the atomic positions of all oxygens as schematically represented in figure 7.

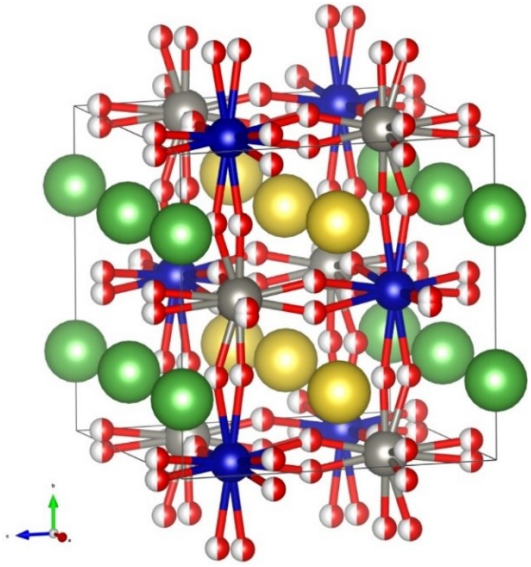

Fig.7: $NaLaCoWO_6$ average structure as refined with neutron data. Co blue, W in gray, Na yellow and La green; all the oxygens in red have partial occupancy in the two split positions.

The average splitting between the two atomic positions of the oxygen is ~ 0.5 Å (table 2). The splitting positions of the oxygens found in the Wyckoff ***4i*** position (all equatorial oxygen O1, O3, O4 and O5) are linked by a of the mirror plane passing along the *h0l* direction. On the contrary, the splitting of the apical O2 site has been modelled with two Instead, the two positions (O2 and O2') of the apical O2 site in position ***8j*** are symmetry-independent positions.

Table 2. Distance between the split positions of the oxygens.

Atom	*Distance (Å)*
O1-O1'	0.72(3)
O2-O2'	0.609(1)
O3-O3'	0.756(1)
O4-O4'	0.17(7)
O5-O5'	0.49(3)
Average	0.549(1)

The disorder of the anions position results into two different octahedra around the cations Co^{+2} and W^{+6}, and the incommensurable modulation of the structure is associated to the change in the octahedral geometry around the cations *B* and *B'*. This suggests that two different tilting topologies of the octahedral frameworks coexist in the crystal structure of $NaLaCoWO_6$, likely inducing the incommensurate modulation. With the information found from the ED data (vector of modulation and superspace symmetry) and the sensitivity of the neutrons for the oxygens, the incommensurable structure was determined starting from the neutron diffraction data (see Fig. 8).

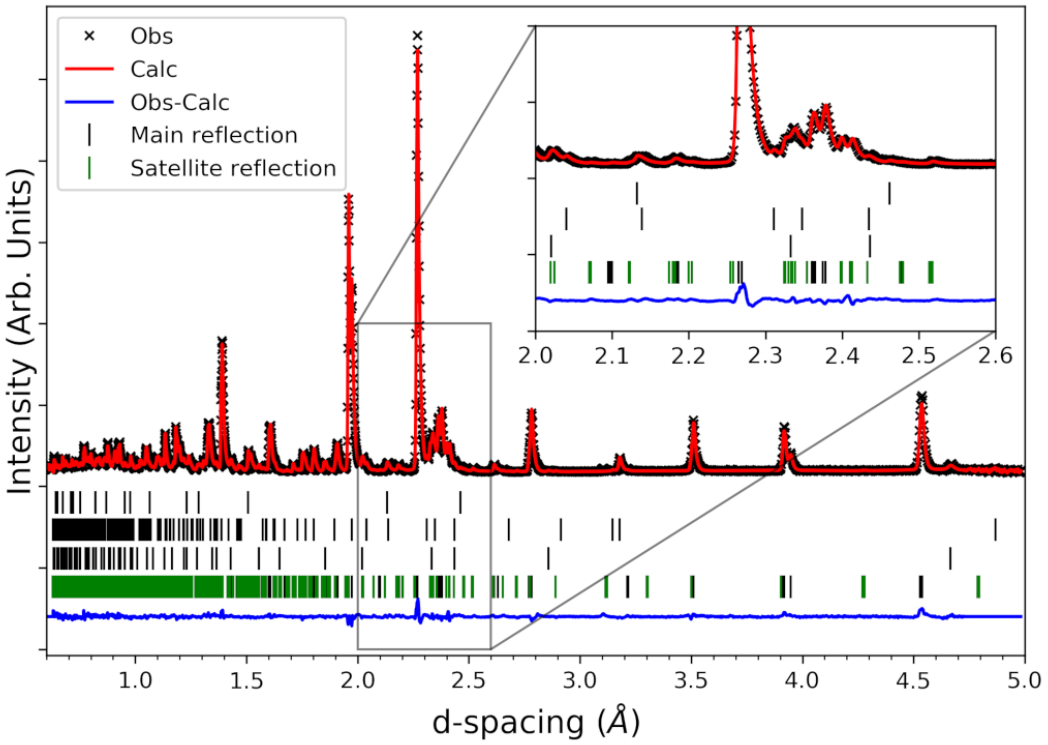

Fig. 8: Plot of the Rietveld refinement of the C2/m(α0γ)0s structure of $NaLaCoWO_6$ against TOF neutron diffraction data. Observed data (black point), calculated pattern (red line) and difference (blue line) are reported. The thick marks(bottom) indicate the Bragg position of the main phase in black, in green satellites of first order, in black of CoO, in black of Co_3O_4 and in black $LaNaW_2O_8$. The reliability factors are wR_p=3.39%, R_p=2.80%.

The discontinuous modulation function of Crenel[13] (1) was used to describe the positions of the oxygens, which allows to describe the positional alternation between the two sites generated by the symmetry operations of the superspace group.

$$f(\bar{x}_4) = 1 \quad \bar{x}_4 \in [\bar{x}_4^0 - \frac{\Delta}{2}, \bar{x}_4^0 + \frac{\Delta}{2}] \tag{1}$$

$$f(\bar{x}_4) = 0 \quad \bar{x}_4 \notin [\bar{x}_4^0 - \frac{\Delta}{2}, \bar{x}_4^0 + \frac{\Delta}{2}]$$

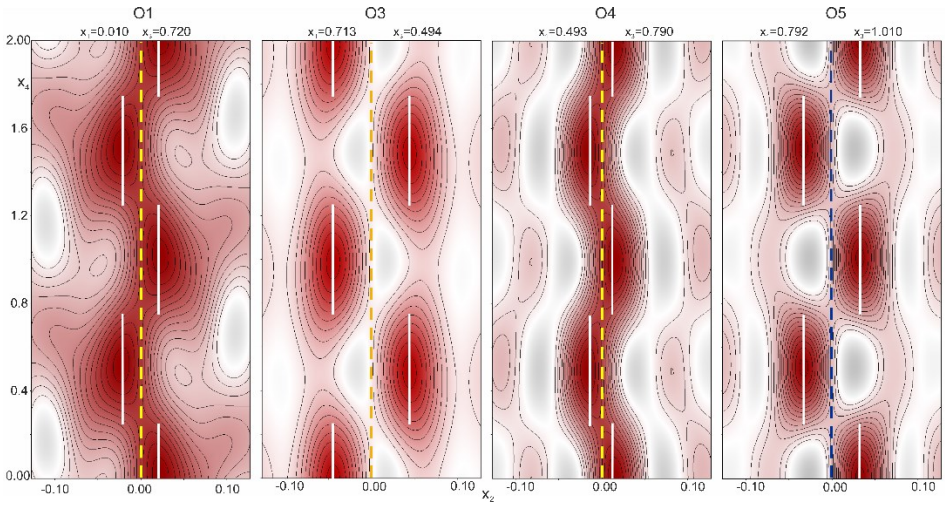

Fig.9: F_{obs} Fourier maps of the (3+1)D super-space around selected atoms, projected on the $x_{2–x4}$ planes. Horizontal axes display x_2 fractional coordinates (y coordinates) and vertical axes correspond to x_4; The fitted atomic modulation functions, represented as continuous white lines, show how the modulation causes the atoms to displace from their average special position on the mirror plane in yellow and twofold axis in blue, represented as a dashed line.

The two equivalent positions for the equatorial oxygen O1, O3 and O4 are generated by a mirror plane and by a glide plane for O5 both perpendicular to ***b*** and symmetrized by the super-space operator x_1, $-x_2$, x_3 and $x_4 + 1/2$ in figure 9. The modulation of these equatorial oxygens has a width of *0.5*, in accordance with the stoichiometry of the average structure, and has the origin at zero (parameter x_4^0). To verify the correctness of the imposed constraints, it was simulated the case in which the parameter x40 is different from 0. In this case, strong satellites *111+1* and *110-1*, should have been observed.

Nevertheless, they are absent in the experimental data. The superspace group *C2/m(α0γ)0s* is characterized by the element of symmetry $\{m_y|000s\}$ that in combination with the crenel function features, ensures the occupation of only one position at the same time, above and below the plane of the mirror plane or glide plane. Apical oxygen O2 has a different modulation with respect other oxygen sites, and the two positions are not correlated by symmetry operations. Therefore, to explain the behavior of the modulation in the structure, it was necessary to consider two independent oxygens that occupy their site alternately during the modulation period. The O_2 has modulation along the x_3 direction (corresponding to direction c in the real space) so far, in the whole modulation period, the O_2 remains on the mirror plane and therefore in a special position (Fig. 10).

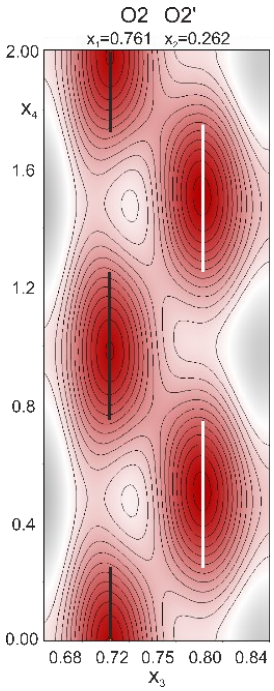

Fig.10: F_{obs} Fourier maps of the (3+1)D super-space around selected atoms, projected on the $x_{2–x3}$ planes. Horizontal axes display x_3 fractional coordinates (z coordinates) and vertical axes correspond to x_4; The fitted atomic modulation functions, represented as continuous white and black lines, in black O2 and in white O2'.

To simplify, in the structure when O2 is present in site in O2' position a vacancy exists and conversely, when O2' is occupied in O2 position is vacant. This complementarity produces full long-rage occupancy in modulated structure. This movement of the anions causes a change of the octahedra tilting and causes a simultaneous shift of all remaining cations. The positional modulation of these heavy atoms is minute and it is fitted with a crenel function. The two positions of the cations *A* and *A'* are generated by a twofold axis oriented orthogonally respect to ***a*** instead for the cations B and B' the two positions are generated by a mirror plane orthogonal to ***b***. Both modulations cause a positional alternation above and below the plane along which the symmetry operations are located (Fig. 11).

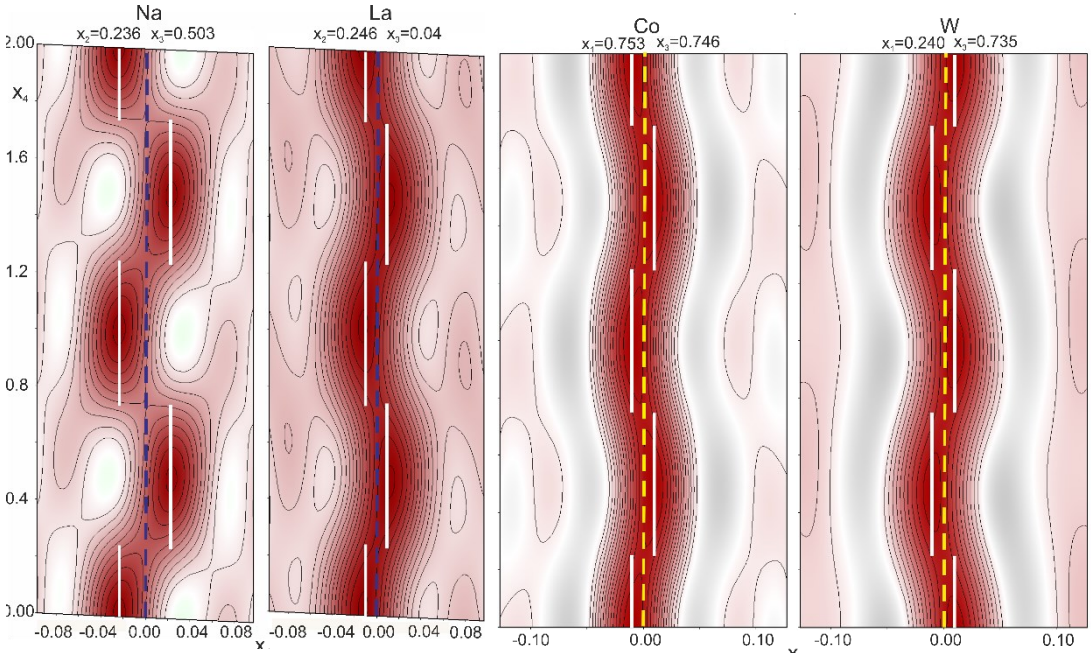

fig.11: Fobs Fourier maps of the (3+1)D superspace around selected atoms, projected on the x_1–x_4 planes (left) x_2–x_4 plane (right). Horizontal axes display $x_{1,2}$ fractional coordinates (x,y coordinates) and vertical axes correspond to x4; The fitted atomic modulation functions, represented as continuous white lines, show how the modulation causes the atoms to displace from their average special position on the twofold axis in blue and mirror plane in yellow, represented as a dashed line.

To verify the validity of this structural model, we also refined it on 3D-ED single crystal data with a kinematic approximation that led to an *R* factor of wR_p=*21.92%,* R_p=*20.30%* and *GOF=13.15*. The change of the octahedra tilting (Fig.12) and refined parameters are shown below (Table 3 and Table 4):

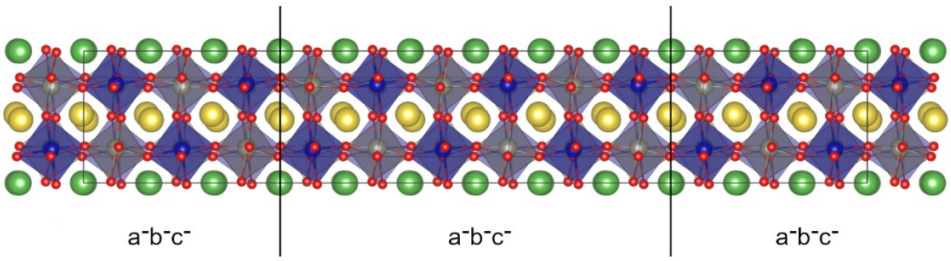

Fig. 12: One dimensional octahedral tilt twining along direction a, with cell size $12a_p$. *The interchange in inclination occurs at one sixth of the supercell.*

The incommensurate modulation can be described by an abrupt change of sign of the tilting angle along the *a* and *c* directions which resemble a twinning boundary. The tilting pattern in the structure is a^-b^-c, with the tilting angle along the *b* direction constant across the structure. The antiphase tilting along the *c* direction (see Figure 12) is a direct consequence of the $x_{4,0}$ parameter being 0. The anion distortions are responsible for the modulation, as expected from the weak signal in the XRD compared with the neutron one, and the cations distortion follows the changes in the octahedral tilting.

For the structure solution of the incommensurate distortion, we adopted the sinusoidal modulation functions formulated by Van Smaalen[22]. Indeed, such wave-like continuous functions was inadequate to get a satisfactory agreement with the Wollf's sections of the (3+1)-dimensional Fourier maps. To better define the discontinuities recognized in those maps the co-called Crenel functions are likely more adequate. The structural modulation is mainly due to the coexistence of two independent systems of octahedral tilting. Therefore, the incommensurate distortion is originated by the alternation of this two conditions in an incommensurate fashion. So far, the Crenel discontinuous function can properly describe such alternation (see Fig. 9 and 10) of the oxygens positions. The modulation of the cations is less

pronounced and in general the adoption of the Crenel function provides the best agreement factors in the combined refinements with ED and TOF diffraction data.

Table 3: crystallographic data of $NaLaCoWO_6$ and parameters for data refinement.

	Average Structure	*Modulated Structure*	*Modulated Structure*
Crystal data			
Crystal System	*Monoclinic*	*Monoclinic*	*Monoclinic*
Space or Superspace Group	*C2/m*	*C2/m(α0γ)0s*	*C2/m(α0γ)0s*
A,b,c (Å)	*7.833, 7.842, 7.898, 90.160*	*7.833, 7.842, 7.898, 90.160*	*7.833, 7.842, 7.898, 90.160*
Modulation vector		*q=0.172a**	*q=0.172a**
Data collection			
Source	*Electrons*	*Neutron and X-Ray*	*Electrons*
No. of observed reflection	*534*		*783*
Range ok h, k, l, m	*$h=-8 \rightarrow 8$, $k=-8 \rightarrow 8$, $l=-8 \rightarrow 8$*		*$h=-6 \rightarrow 6$, $k=-6 \rightarrow 6$, $l=-6 \rightarrow 6$*
Refinement			
$R[F^2 > 2\sigma(F^2)]$, $wR(F^2)$ main reflection	*0.146*	*0.339*	*0.219*
$R[F^2 > 2\sigma(F^2)]$, $wR(F^2)$ Satellite reflection		0.570	*0.316*
No. of Reflection	*534*	*16363*	*249*
No. of Parameters	*35*	*46*	*40*

Table 4. Final structural parameters for the C2/m(α0γ)0s model described in the text for the neutron and X-ray refinement (upper line) and 3D-ED data (bottom line).

Atoms	*x*	*y*	*z*	U_{iso}	*Δ*	*x4,0*
Na1	-0.0157(8) -0.033(4)	0.2466(10) 0.232(3)	0.4803(8) 0.517(5)	0.0037(13) 0.019(9)	0.5	0
La1	-0.0077(5) -0.0065(12)	0.2482(4) 0.2472(8)	0.0003(5) 0.0038(18)	0.0188(5) 0.039(4)	0.5	0
Co1	0.7435(13) 0.7394(15)	-0.0101(10) 0.0064(14)	0.7455(8) 0.7265(19)	0.0013(10) 0.025(5)	0.5	0
W1	0.2514(6) 0.2537(7)	0.0109(6) 0.0103(7)	0.7342(3) 0.7440(8)	0.0122(6) 0.016(4)	0.5	0
O1	0.0097(6) 0.003(3)	0.0269(6) 0.001(3)	0.7215(4) 0.737(5)	0.01562(19) 0.033(6)	0.5	0
O2	0.7695(6) 0.760(4)	0.2584(5) 0.253(3)	0.7276(4) 0.753(5)	0.01562(19) 0.033(6)	0.5	0
O2'	0.7497(6) 0.734(4)	0.2658(5) 0.243(3)	0.7990(5) 0.812(7)	0.01562(19) 0.033(6)	0.5	0.5
O3	0.7116(6) 0.706(4)	-0.0412(5) -0.051(3)	0.4934(4) 0.500(6)	0.01562(19) 0.033(6)	0.5	0
O4	0.4905(6) 0.502(3)	0.0120(6) 0.002(3)	0.7979(5) 0.788(5)	0.01562(19) 0.033(6)	0.5	0
O5	0.7879(5) 0.790(4)	0.0311(5) 0.044(3)	1.0093(4) 0.991(6)	0.01562(19) 0.033(6)	0.5	0

The neutron and x-ray refinement has been conducted on the ToF data collected on WISH at average *2θ* of 154°, 121°, 90° and 57° and on the X-ray collected with Cu-Kα1 radiation. The refined cell parameters are *a=7.83302(8) Å, b= 7.84217(8) Å, c= 7.89833(7) Å, β=90.160(10)°* and *q= 0.1710(3)a** and the overall reliability factors are R_p*=2.88%,* $_wR_p$*=4.08 %.* The electron diffraction refinement has been performed in kinematical approximation with overall reliability factors of R_{wp}=18.49%, R_p*=17.59*% and *GOF=11.07*.

4.1.6 Results on the stoichiometry

After the collection of the electron diffraction, a compositional analysis was carried out with the EDX technique (Fig. 13) on the same nanocrystals used for the electron diffraction experiments. The analysis indicates a systematic sodium and tungsten deficiency within the sample with an average composition of the sample close to: $Na_{0,76}La_{1,24}Co_{1,12}W_{0,87}O_6$. On the contrary, the combined X-ray/TOF-NPD structural refinements the La, Na and W sites are fully occupied and neither mixing of the two heterovalent ions nor randomly distributed vacancies are noticed. Both sites result completely occupied and the refined composition is in agreement with the nominal $NaLaCoWO_6$ stoichiometry. Furthermore, the identified secondary phases are composed by all the elements involved in the nominal composition indeed their presence in not in contrast with the occurrence of the 1:1 ratio for La and Na in the doubly ordered perovskite. The sodium deficiency in the structure can be explained by the formation of Na_2O at high temperature found in previous syntheses[12] but also by Na loss induced by the electron irradiation. The illuminated region can be depleted in Na content that tends to evaporate as documented in the literature by the observation of the segregation of metallic Na and Na_2O[25,26].

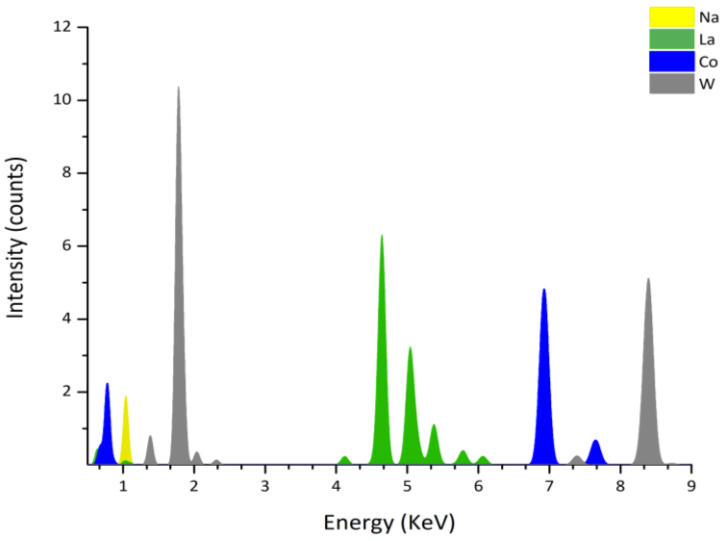

Fig. 9: EDX spectrum on a nanocrystal of doubly ordered perovskite.

For instance, we can conclude that the doubly ordered perovskite is not characterized by off stoichiometry. The postulated presence of occupational modulation, based on EDX data and envisaged in several published works[19,20], is therefore disproved by the actual results.

4.1.7 Symmetry Analysis and the HIF Density Wave

To discuss the details of coupling and dipolar ordering inside the incommensurate phase, it is more convenient to refer to the commensurate phase with symmetry $P2_1$. In the rest of the chapter, we will describe the distortions of all phases with respect to the parent structure *P4/nmm*.

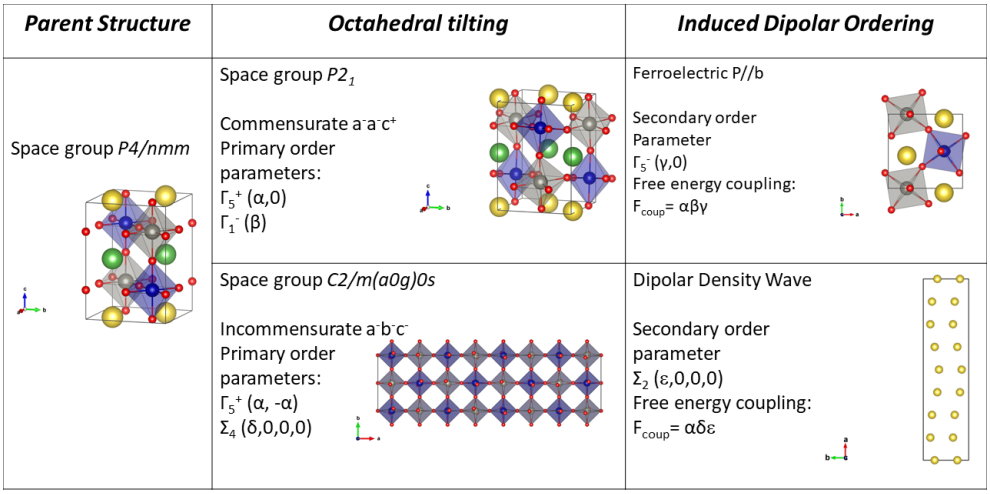

Fig. 10: Symmetry analysis of the $P2_1$ and $C2/m(\alpha 0\gamma)0s$ structures. Schematic display of the primary octahedral tilting distortions and of the corresponding induced dipolar ordering for the phases.

Operating in this way will simplify the terms of the coupling and the calculations of group theory. The *P4/nmm* symmetry derives from the structure of the aristotype perovskite, which has Pm-3m symmetry by the action of two irreducible representations:

- By action of the irreducible representation $\mathbf{R_1^+}$, and a propagation vector (1/2, 1/2, 1/2), which causes the checkerboard ordering of site B
- By action of the irreducible representation $\mathbf{X_3^-}$ with a propagation vector (0, 0, 1/2) that give rise to the ordering of the layers of site A.

This last transformation is important for the HIF mechanism because it causes the removal of the inversion operation in the point group of site B, this allows the octahedra to assume any inclination, which causes the breaking of the macroscopic symmetry, removing the spatial inversion operation. The HIF mechanism, in fact, in the low temperature commensurate phase *P2₁* of the doubly ordered perovskites $AA'BB'O_6$ is related to the tilting of the octahedra, which assume the $a^-a^-c^+$ [14–17] topology. In particular, the antiphase tilting (a^-) of octahedra along the crystallographic directions a and b are related to the irreducible representation Γ_5^+ with a parameter of order α. On the other hand the inclination in phase (c^+) around the c axis is due to the irreducible representation Γ_1^- with a parameter of order β. These distortions acting simultaneously on the parent structure with *P4/nmm* symmetry cause a secondary polar distortion, which transforms as an irreducible representation Γ_5^- with a parameter of order γ, but with a trilinear free energy invariant αβγ as it is schematically represented in the figure 10. The transformation Γ_5^- that causes the polar distortion in the structure causes an opposite and uniform shift between the cation and the anion which has the effect of creating a net dipolar moment along the *b*-axis in the *P2₁* structure. This polarization induced in the structure by this transformation is switchable if an external electric field is applied, and the switching mechanism would require a change of sign of the parameters α or β which would imply a change in the inclination to $a^-a^-c^0$ or $a^0a^0c^+$ respectively. The incommensurable phase of the compound

$NaLaCoWO_6$ is found in a similar case but presents itself with an incommensurable order of the induced dipoles. The phase with symmetry *C2/m(α0γ)0s* resolved and refined in this thesis can be obtained from the relative structure *P4/nmm* by action two distortions that operate, also in this case, on the octahedral tilting topology:

- The transformation Γ_5^+ causes a commensurate inclination out of phase along the direction b. It is the same transformation present in the phase $P2_1$ that causes the tilting scheme $a^-a^-c^0$ but with a different direction of the order parameter that is (α, $-\alpha$).
- The transformation Σ_4 with order parameter δ causes an incommensurable tilting out of phase along the directions a and c. This effect is originated by the condition $x_{4,0} = 0$ of the crenel function.

These two distortions, which act on the tetragonal parent structure, induce an incommensurable displacement of the cation along the direction b that transforms with Σ_2 with a trilinear invariant $\alpha\delta\varepsilon$ in the free energy as schematized in the figure 10. The analogies between the commensurate $P2_1$ case and the incommensurate *C2/m(α0γ)0s* one let us to conclude that in the latter case we have observed the development of an incommensurate ordering of the induced dipoles with the same propagation vector as the incommensurate tilting. The induced dipoles are oriented along the b axis, in analogy with the $P2_1$ phase, and their amplitude is modulated with the period of the modulation vector, resembling the electric analog of a spin density wave. For the latter reason we describe the incommensurate dipolar ordering as a hybrid improper dipolar density wave.

4.1.8 Magnetic Characterization of the $NaLaCoWO_6$

The magnetic properties of this phase were investigated used a SQUID magnetometer at Department of Physic of University of Parma. Measurements were carried out in which a cooling with no field and a cooling with a field (ZFC/ZF) which showed antiferromagnetic behavior at a temperature below 25K were carried out:

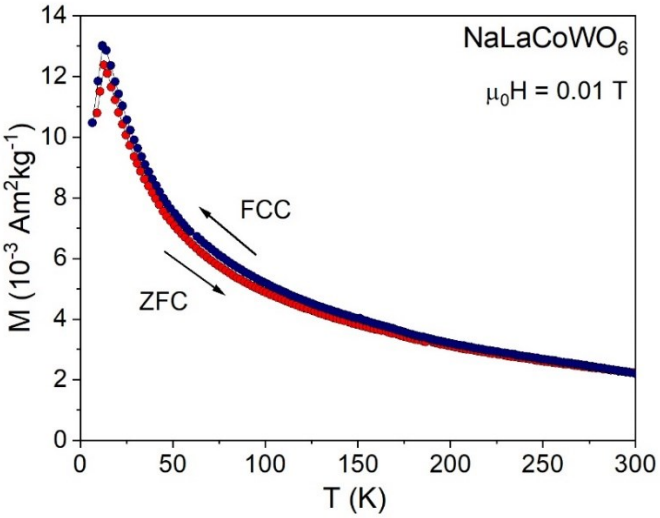

Fig. 11: Zero field cooling Field Cooling curves for NaLaCoWO6 compound.

This low temperature transition can be attributed exclusively to the presence of Co^{2+} which is the only ion magnetically active. Since Co and W are ordered the superexchange interaction would involves the chain Co-O-W-O-Co. Thus, the magnetic interaction is indirect and the strong tilting of the oxygen-linked octahedra contributes to the low temperature of the spin ordering. In earlier studies[18] isothermal magnetization curves performed below the T_N (Neel Temperature) demonstrated that the antiferromagnetic ordering is not perfect, and it is postulated the presence of frustrated effects, such as glassy magnetic states, pointing out that the magnetic nature of this system is complex. In earlier studies, the magnetic characterization for $NaLaFeWO_6$ and $NaNdFeWO_6$ systems has evidenced similar antiferromagnetic phases with T_N ordering temperatures below 25K. In the case of Nd-based doubly

ordered perovskite ZFC/FC curves are characterized by the progressive increment of the susceptibility below the T_N. This increment is not observed for the counterpart $NaLaFeWO_6$, and it is attributed to the magnetic contribution of the magnetic Nd^{3+} that tends to couple with the magnetism of the Fe^{2+} ions. For instance, the magnetic behavior for $NaLaMWO_6$ with M=Fe^{2+}, Mn^{2+}, Co^{2+} is substantially equivalent with slight differences of the magnetic ordering temperature[18,19]. Neutron diffraction experiments conducted on $NaNdFeWO_6$ below 25K revealed the occurrence of a long-range antiferromagnetic ordering with propagation vector *k=(1/2,0,½)*. This magnetic structure characterizes the low temperature crystal structure showing monoclinic $P2_1$ symmetry. The magnetic structure, depicted in figure 12 is composed by the antiparallel columns of Fe magnetic moments along the b axis oriented in antiparallel fashion along the *a* axis. The spins of Nd are ordered in ferromagnetic layers stacked in antiparallel reciprocal orientation. The same type of neutron diffraction experiments for the $NaLaFeWO_6$ system did not reveal the occurrence of low temperature long-range antiferromagnetic state. The authors accounted the absence of magnetic contribution to the scattering likely related to the low magnetic moment distributed in a single unit cell. This effect could be ascribed to the presence of only half B sites occupied by a magnetic ion and to the weak magnetic interactions mediated by the W atoms.

Nevertheless, for $NaLaCoWO_6$ the study of the low temperature antiferromagnetic state would require a series of neutron diffraction experiments below 25K in order to explore the eventual long-range ordered distribution of the magnetic moments of Co^{2+} ions. Such neutron diffraction experiments could provide valuable information on the occurrence of the structural transformation from incommensurate C2/m structure to unmodulated $P2_1$ phase described by P. Zuo et al.[20] but not observed in ED data collected below the transition temperature.

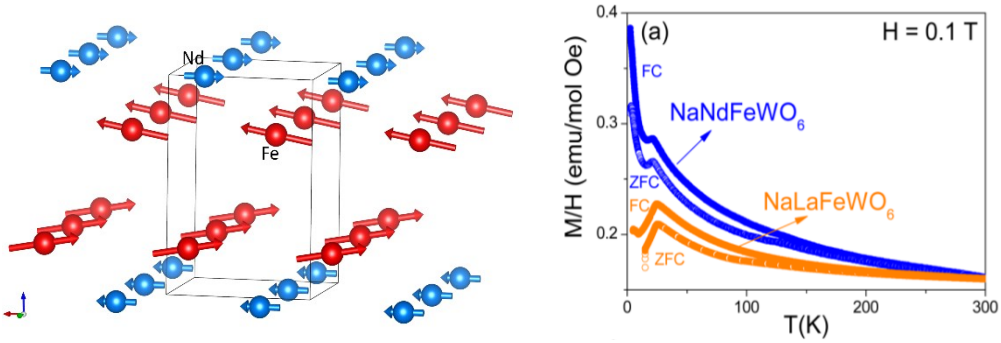

Fig. 12: Left: Monoclinic magnetic structure at 20K for $NaNdFeWO_6$ where magnetic moments of Fe and Nd are antiferromagnetically ordered. The only Fe (red) and Nd (blue) atomic positions of the $P2_1$ crystal structure are depicted. Right: ZFC/FC curves for NaNdFeWO6 and NaLaFeWO6 respectively[18].

4.2 Structural study of doubly ordered perovskite $Na_{1\pm x}La_{1\pm x}MgWO_6$

To verify that the modulation of this type of perovskite is not related to its composition but to the octahedral tilting, three phases of $NaLaMgWO_6$ were synthesized with a different amount of Na. The three phases synthesized by the same procedure were:

- ***$Na_{0.8}La_{1.2}MgWO_6$***
- ***$NaLaMgWO_6$***
- ***$Na_{1.2}La_{0.8}MgWO_6$***

Where in two compositions the Na incorporation is deficient and in excess with respect the 1:1 ratio.

4.2.1 Synthesis of $Na_{1\pm x}La_{1\pm x}MgWO_6$

For the synthesis of all phases of these doubly ordered perovskites we followed the protocol reported by Borchani et al.[1]. This protocol involves a solid-state reaction which involves mixing, in stoichiometric quantities of Na_2CO_3, La_2O_3 and $MgWO_4$. For a better synthesis, the $MgWO_4$ precursor was freshly synthesized through another solid-state synthesis which involves mixing stoichiometric quantities of MgO and WO_3 and a heat treatment at 950°C for 8 hours. For the synthesis of perovskites, the reactant oxides, once mixed with the right stoichiometry, are thermally treated at 925°C in air for 6 hours with a heating ramp of 4.5°C/min. Once the treatment was completed, the sample was ground and pressed to form a pellet and sintered at a temperature of 950°C with a ramp of 2.5°C/min for 8 hours.

4.2.2 Diffraction Experiments

Precession-assisted 3D ED were performed with the Zeiss Libra 120 transmission electron microscope working at 120 kV and equipped with a LaB_6 thermionic source and a Bruker EDX XFlash6T-60 detector at the National Enterprise for nanoScience and nano Technology in Pisa. For the electron diffraction collections, the samples were ground with an agate mortar and the resulting powder was suspended and sonicated in ethanol and drop-deposited on a carbon coated copper grid. Sequential electron diffraction patterns were collected in nanodiffraction mode with a parallel beam of 150 nm, obtained by selecting a condenser aperture of 5 μm. Data were energy-filtered on the zero-loss peak with an in-column Ω-filter and a slit width of about 20eV[2]. Patterns were collected in stepwise mode with a protocol explained by E. Mugnaioli et al.[3]. The precession motion of the electron beam around the optical axis was obtained by a Nanomegas Digistar P1000 device[4]. The semi-aperture of the precession cone was set to 1°. The angular collection range of 3D ED data was up to 120° degrees, with steps of 1°. After each tilt step, for check the crystal movement STEM image was taken and the electron beam was repositioned back in the same point of the crystal. Diffraction patterns were recorded by an ASI Timepix single-electron detector[5]. Cell determination, modulation vector definition and electron diffraction intensity extraction were performed with the PETS 2.0 program on data from thirty different nanocrystals[6]. The X-ray diffraction measurements were performed with a STOE Stadi P diffractometer equipped with Cu-$K\alpha_1$ radiation, a STOE&Cie Johansson monochromator and a Dectris MYTHEN2 1 K detector. The X-ray analyses have been performed in transmission geometry, the sample are ground and placed in a borosilicate capillary. The diffraction measurements with a synchrotron source were collected at the Elettra beam line[21]. All structure refinement were performed with the Jana2006 software[8]. The electron diffraction data has been treated within the kinematical approximation.

4.2.3 Crystal Analysis of $NaLaMgWO_6$

To discover the structure of the $NaLaMgWO_6$ in which the balance of metals A and A 'is 1:1. 3D electron diffraction (3D-ED) was collected on ten different nanocrystals. Also in this case, evidence of a superstructure was found. So, we proceeded as in the previous case, studying first the average structure and then the modulated one. From the indexing of the main reflections a monoclinic cell with cell parameters was found: $a=7.82(1)Å$ $b=7.83(4)Å$ $c=7.89(2)Å$ e $\beta=90.19(3)Å$.

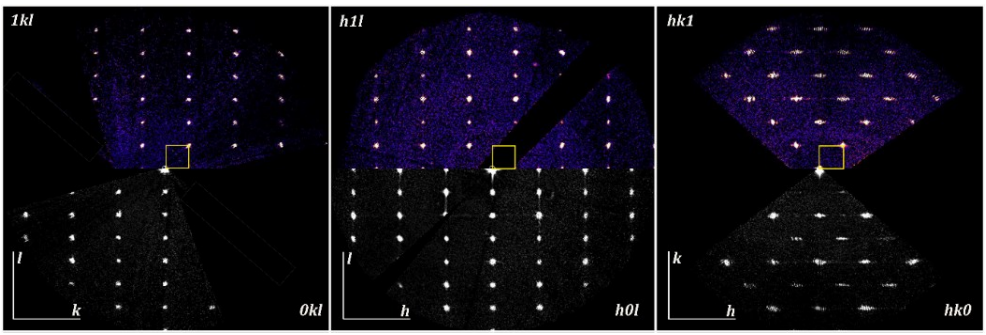

Fig.1: Sections of the reciprocal space of $NaLaMgWO_6$ obtained from a 3D ED data collection. On top in violet, plane of the reciprocal space following the fundamental section. The black zones, devoid of reflections, are areas of the reciprocal space that are not integrated due to the mechanical limitations of the TEM.

From the study of the reconstruction of the reciprocal space (fig.1) the symmetry of the structure was determined. In this case there is an alternation of the diffraction columns in the *0kl* and 1kl plane and in the *h0l* and *h1l* plane, together with a checkerboard pattern in the *hk0* and *hk1* reconstruction. The extinction rule $h+k=2n$ indicates that the structure has a lattice with *C*-centering, but since there are no other extinction rules, the structure can have three different symmetries *C2*, *Cm* and *C2/m*. It is clearly seen from the reconstruction of the reciprocal space that the main reflections are accompanied by first order satellites along the ***a**** direction, a clear signal that the structure is modulated.

4.2.4 Average structure of $NaLaMgWO_6$

We proceeded as in the case of the previous perovskite, initially we integrated only the intensities of the main reflections, to find the average structure of the perovskite. The structure was determinate using the SuperFlip algorithm integrated into the *JANA2006* software[8]. The resulting structure is very similar to the previous one. In fact, it consists of two alternating layers between the A (Na^{+1} and La^{+3}) and B (Mg^{+2} and W^{+6}) components of the doubly ordered perovskite along the ***b**** direction. The layer composed of the cations Mg^{+2} and W^{+6} with an octahedral coordination that share the corners has a checkerboard order and is alternated with the layers of the cations Na^{+1}/ La^{+3} and La^{+3} which are stacked along ***a**** (figure 2).

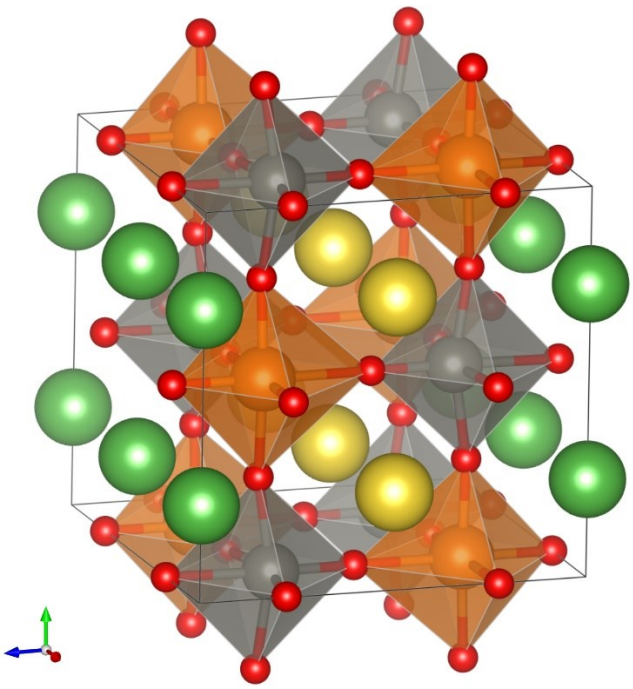

Fig.2: $NaLaMgWO_6$ average structure. Mg in orange and W in gray. Na in yellow and La in green, oxygens in red. With rock salt order for cations B/B' and layer order for A/A'.

The octahedra MgO_6^{-8} and WO_6^{-2} have a tilting pattern of $a^0b^-c^0$ in Glazer[11] notation. For the refinement of the average structure, in addition to the electron diffraction data which have a $wR_{obs}=8.42\%$, was used a diffractogram collected with transmission geometry and a Cu Kα1 (λ= 1.54059 Å) source was used. Using the Rietveld method on the diffractogram we have a discrepancy factor of $wR_{obs}=2.58\%$.

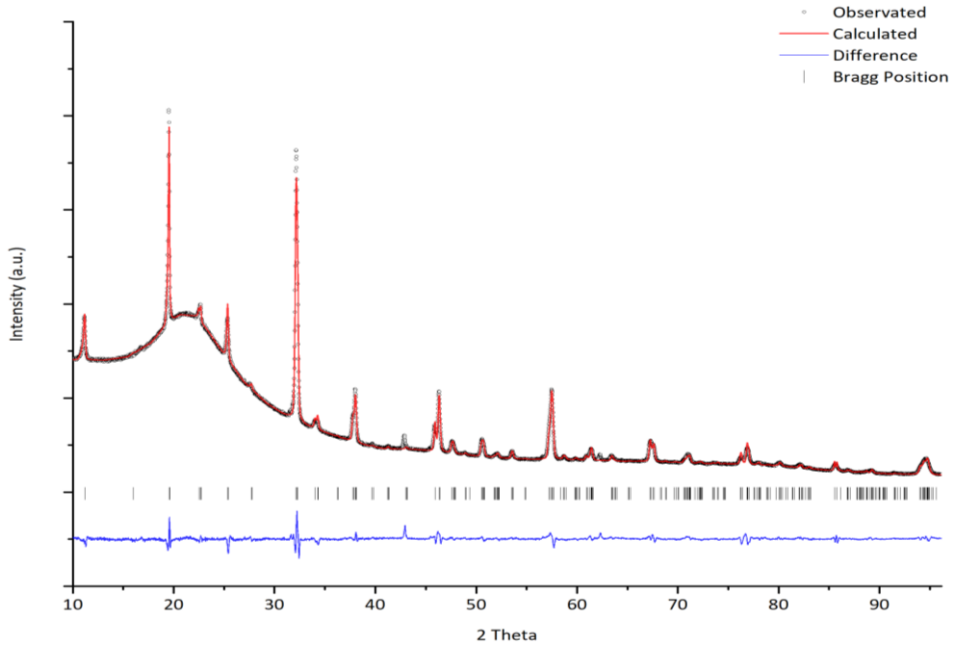

Fig.3: Plot of the Rietveld refinement of the average C2/m structure of $NaLaMgWO_6$ against X-ray data. Observed data (black point), calculated pattern (red line) and difference (blue line) are reported. The thick marks(bottom) indicate the Bragg position of the main phase.

In this phase no impurities were found unlike the previous Co-based perovskite. Also in this case, in the X-ray diffractogram satellites are completely absent due to the lower resolution of the technique compared to 3D-ED.

For this phase we also carried out measurements at the Elettra synchrotron in Trieste. As you can see from Rietveld refinement (fig. 4) even with the wavelength of *(λ= 0.823633 Å)* no satellites are visible. However, it was useful to refine the average structure of the doubly ordered perovskite.

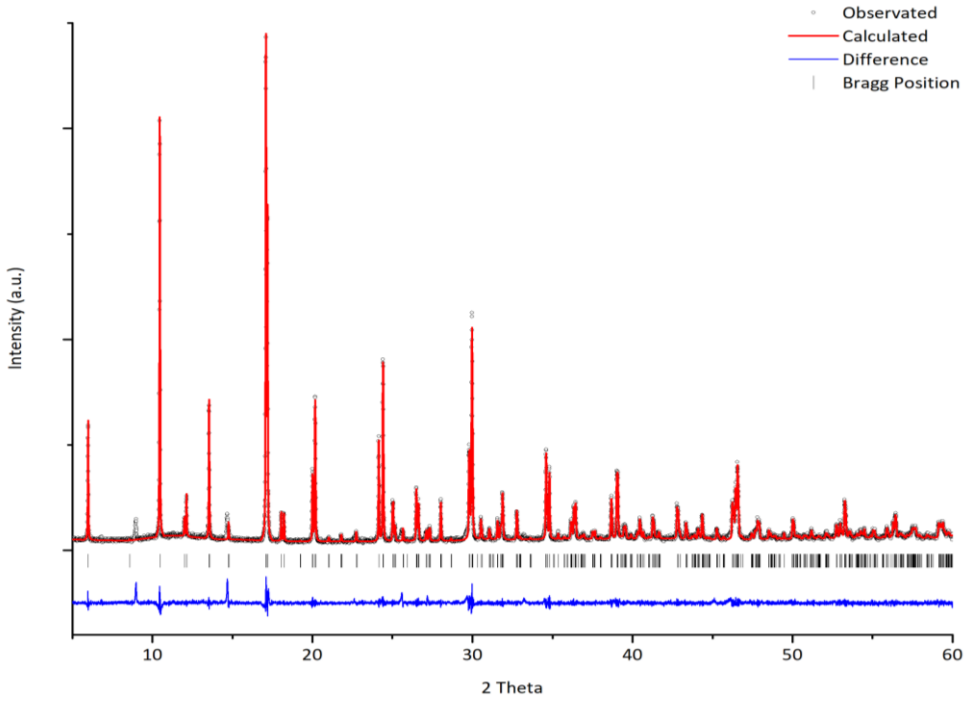

Fig. 4: Plot of the Rietveld refinement of the average C2/m structure of $NaLaMgWO_6$ against synchrotron data. Observed data (black point), calculated pattern (red line) and difference (blue line) are reported. The thick marks(bottom) indicate the Bragg position of the main phase.

Table 1: Structural parameters of the average C2/m structure from the combined refinement of the X-ray, synchrotron source and 3D-ED data at room temperature.

Atom	*Wyckoff Symbol*	*x*	*y*	*z*	U_{iso}
Na	4h	0.5	0.249(5)	0.5	0.090(3)
La	4g	0.5	0.250(1)	0.0	0.011(8)
Mg	4i	0.233(6)	0.5	0.233(6)	0.026(9)
W	4i	0.251(7)	0.0	0.265(5)	0.002(4)
O1	4i	0.006(7)	0.0	0.227(1)	0.007(2)
O2	8j	0.247(5)	0.245(7)	0.230(4)	0.006(8)
O3	4i	0.259(8)	0.0	0.484(3)	0.044(6)
O4	4i	0.495(8)	0.0	0.233(6)	0.008(2)
O5	4i	0.233(7)	1.0	0.996(3)	0.008(7)

Space group C2/m, Z=4. Unit-cell parameters: a=7.83(1)Å b=7.79(2)Å c=7.87(3)Å e *β=90.13(2)Å. Discrepancy Factor on electron data:* wR_{obs}*=8.42%* R_p*=7.24% GOF=3.16. Discrepancy Factor on X-ray data:* wR_{obs}*=2.58%,* R_p*=1.58% GOF=2.98. Discrepancy Factor on Synchrotron data:* wR_{obs}*=1.58%,* R_p*=2.67% GOF=4.25.*

4.2.5 Modulated Structure of $NaLaMgWO_6$

To solve the superstructure, firstly, were defined the modulation vector ***q*** and the reflection conditions in 4D-space by studying the reciprocal space of the 3D-ED data. The modulation vector for indexing the satellites has a single component *q=0.176(2)a** and the reflection conditions of the satellites *hklm: h+k=2n* and *h0lm:m=2n* consistent with the superspace group *C2/m(α0γ)0s*. We are therefore in the special case in which the third component of the modulation vector ***q*** is equal to zero. With these information was made an attempt at structural resolution using a superspace approach on a complete 3D-ED data set. The modulation for this phase only concerns the oxygen atoms, in this case a sinusoidal function was used to describe their positions. The positional modulation parameters were found using the JANA2006[8].

The best agreement is obtained with a modulation on the oxygen atoms excluding O2 (apical atom of the octahedral coordination) using the notation of Van Smaalen[22].

$$x(\bar{x}_4) = x_0 + A_x sin(2\pi\bar{x}_4) + B_x cos(2\pi\bar{x}_4) + l_x$$

$$y(\bar{x}_4) = y_0 + A_y sin(2\pi\bar{x}_4) + B_y cos(2\pi\bar{x}_4) + l_y$$

$$z(\bar{x}_4) = z_0 + A_z sin(2\pi\bar{x}_4) + B_z cos(2\pi\bar{x}_4) + l_z$$

where $\bar{x}_4 = \vec{q} \cdot \overrightarrow{r_0} = q_z \cdot (z_0 + l_z)$ and l_x, l_x and l_x are integer number. The atomic position without modulation are x_0, y_0 and z_0. Instead A_i and B_i are the modulation amplitude expressed as fractional coordinates. The amplitudes of the positional modulation of the oxygen are rather minute as it can be observed from the Wolf sections.

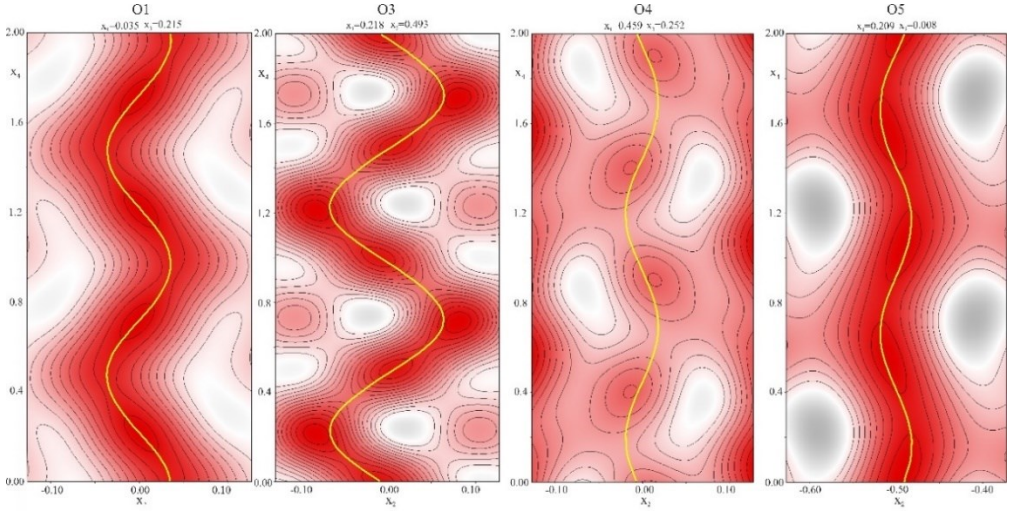

Fig. 5: F_{obs} Fourier maps of the (3+1)D super-space around the to the average position, projected on the x_{2-x4} planes. Horizontal axes display x_2 fractional coordinates (y coordinates) and vertical axes correspond to x_4; The fitted atomic modulation functions, represented as continuous yellow lines

Therefore, the modulation does not cause a change of the tilting scenario but only a change in the magnitude of the relative inclination between the octahedra of W^{6+} and Mg^{2+}. In fact, the attempt to fit the Wolf sections with a crenel or sawtooth function (now disused) was unsuccessful, because the maxima are blurred. As illustrated in Figure 6 this difference of relative

cooperative tilting is visible by considering the position of the O3 which has the positional modulation of greater amplitude.

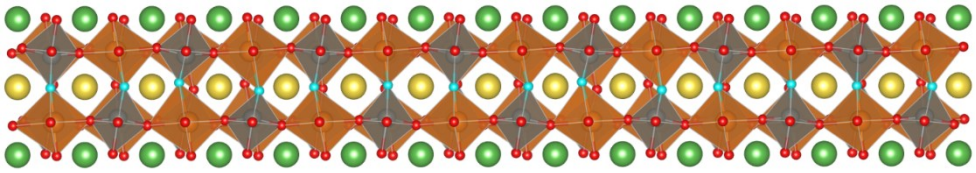

Fig. 6: One dimensional octahedral tilt twining along direction a, with cell size $13a_p$. The relative inclination changes between octahedra, the O3 in cyan.

Table 2: Crystal Data for the $NaLaMgWO_6$ compound.

	Average Structure	*Modulated Structure*
Crystal data		
Crystal System	*Monoclinic*	*Monoclinic*
Space or Superspace Group	*C2/m*	*C2/m(α0γ)0s*
a,b,c (Å)	*7.830, 7.790, 7.872, 90.139*	*7.830, 7.790, 7.872, 90.139*
Modulation vector		*q=0.176a**
Data collection		
Source	*Electrons, X-Ray and Synchotron*	*Electrons*
No. of observed reflection	*6072*	*346*
Range ok h, k, l, m	$h=-8 \rightarrow 8$, $k=-8 \rightarrow 8$, $l=-8 \rightarrow 8$	$h=-6 \rightarrow 6$, $k=-6 \rightarrow 6$, $l=-6 \rightarrow 6$
Refinement		
$R[F^2 > 2\sigma(F^2)]$, $wR(F^2)$ main reflection	*0.025*	*0.156*
$R[F^2 > 2\sigma(F^2)]$, $wR(F^2)$ Satellite reflection		*0.209*
No. of Reflection	*15439*	*456*
No. of Parameters	*34*	*39*

Differently to what observed in $NaLaCoWO_6$ the modulation of the oxygen sites can be described efficiently with a sinusoidal function as evidenced by the difference Fourier maps. The wave-like periodical distortions of the

octahedral coordination could be ascribed to the different chemical nature of the divalent ion. In $NaLaCoWO_6$ the Co^{2+} imparts a Jahn-Teller distortion to the oxygen coordination. The ordered NaCl-like distribution of Co^{2+} (J-T active) and W^{6+} (J-T inactive) is mediated by the discontinuous distortion of the oxygen positions well defined by the Crenel function. The sinusoidal modulation in Mg-based compounds could be related to the B site ordering involving only inactive J-T metals. The Mg^{2+} is a non magnetic ion and obviously is not a transition metal with half-filled d orbitals, therefore the octahedral coordination can be differently distorted with respect the Co^{2+} environment.

Table 3: Distance between the magnesium and the oxygens.

	Distance Mg - Ox	*Distance W - Ox*
M – O1	2.136	1.761
M – O2	1.995	1.937
M – O3	2.225	1.812
M – O4	1.862	1.620
M – O5	1.851	2.079
Average	*2.014*	*1.842*

Further, to confirm the actual model of (3D+1)-dimensional crystal structure, a structural refinement based on the combination of 3D-ED and neutron diffraction data is mandatory. Since the incommensurate modulation is mainly originated by the position of the oxygens, neutron diffraction experiments on $NaLaMgWO_6$ are necessary to complete and consolidate the results obtained with preliminary x-ray, synchrotron, and electron diffraction data.

4.2.6 Differences between $Na_{1\pm x}La_{1\pm x}MgWO_6$

For the two non-stoichiometric phases, the 3D ED electron diffraction and the X-ray diffraction on powder was collected. From electron diffraction in both cases a modulation like the stoichiometric case was found.

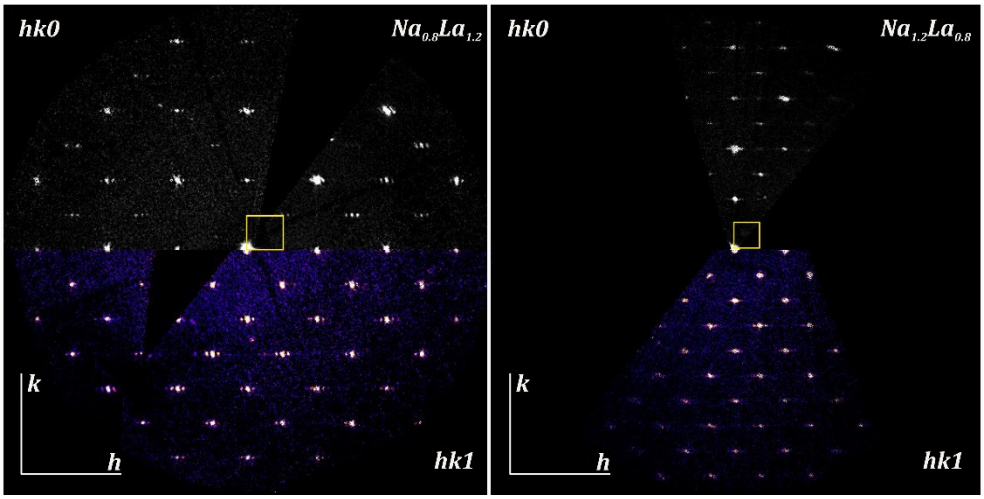

Fig.7: Sections of the reciprocal space of $Na_{1.2}La_{0.8}MgWO_6$ (right)with camera length 230 A^{-1}/px and $Na_{0.8}La_{1.2}MgWO_6$ (left) with camera length 180 A^{-1}/px obtained from a 3D ED data collection. Bottom in violet, plane of the reciprocal space following the fundamental section. The black zones, devoid of reflections, are areas of the reciprocal space that are not integrated due to the mechanical limitations of the TEM.

Indexing the main reflection, we find a same cell between the three phases:

Table 4: Elementary cells of the three phases

	a	*b*	*c*	*β*
$Na_{0.8}La_{1.2}MgWO_6$	7.80(3)	7.81(5)	7.89(3)	90.12(3)
$NaLaMgWO_6$	7.83(1)	7.79(2)	7.87(3)	90.13(2)
$Na_{1.2}La_{0.8}MgWO_6$	7.80(2)	7.81(1)	7.89(4)	90.15(3)

and integrating the main reflections we determinate the average structure with the electron diffraction data and refined together with the XRD data appear very similar and confirm partial occupancy of the excess species on the site A/A'. The structure was determinate using the SuperFlip algorithm integrated into the *JANA2006* software[8] and kinematical approximation.

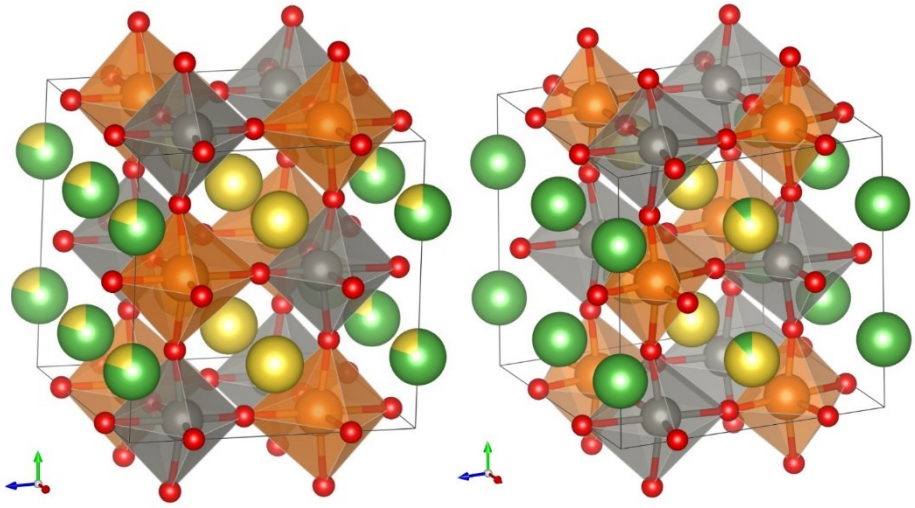

Fig.8: Average structures of $Na_{1.8}La_{0.8}MgWO_6$ (left) and $Na_{0.8}La_{1.2}MgWO_6$ (right). Mg in orange and W in gray. Na in yellow and La in green, oxygens in red. With rock salt order for cations B/B' and layer order for A/A'.

In both case the octahedra MgO_6^{-8} and WO_6^{-2} have a tilting pattern of $a^0b^-c^0$ in Glazer[11] notation. The refinement parameters are show below:

Table 5: Crystal Data for the medium structure of the phases with excess and defect of sodium.

	$Na_{0.8}La_{1.2}MgWO_6$	$Na_{1.2}La_{0.8}MgWO_6$
Crystal data		
Crystal System	*Monoclinic*	*Monoclinic*
Space Group	*C2/m*	*C2/m*
a,b,c (Å)	*7.801, 7.812, 7.893, 90.120*	*7.804, 7.815, 7.895, 90.153*

Data collection		
Source	*Electrons and X-Ray*	*Electrons and X-ray*
No. of observed reflection	*6461*	*6072*
Range ok h, k, l, m	$h=-8 \rightarrow 8$, $k=-8 \rightarrow 8$, $l=-8 \rightarrow 8$	$h=-8 \rightarrow 8$, $k=-8 \rightarrow 8$, $l=-8 \rightarrow 8$
Refinement		
$R[F^2 > 2\sigma(F^2)]$, $wR(F^2)$	*0.130*	*0.064*
No. of Reflection	*6461*	*6000*
No. of Parameters	*23*	*32*

By refining the excess sodium phase with the XRD data we were able to determine the presence of different impurities, Na_2WO_6, and $Na_4Mg(WO_4)_3$ due to the excess sodium of the system and the high temperatures used during perovskite synthesis.

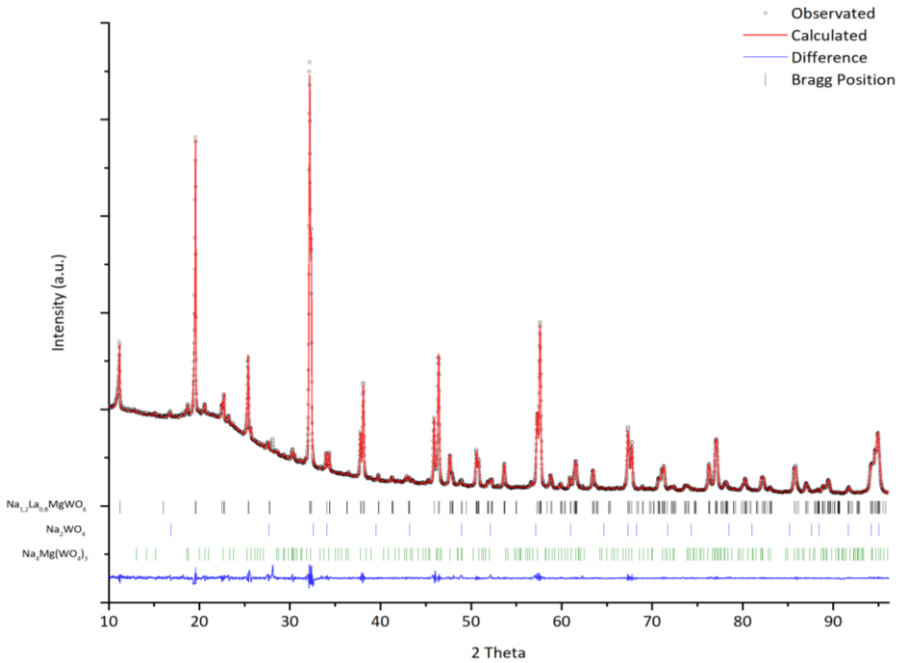

Fig.9: Plot of the Rietveld refinement of the average C2/m structure of $Na_{1.2}La_{0.8}MgWO_6$ against X-ray data. Observed data (black point), calculated pattern (red line) and difference (blue line) are reported. The thick marks(bottom) indicate the Bragg position of the main phase in black.

Indeed, in the XRD of the phase with sodium defects, we don't observe the impurities inside the sample:

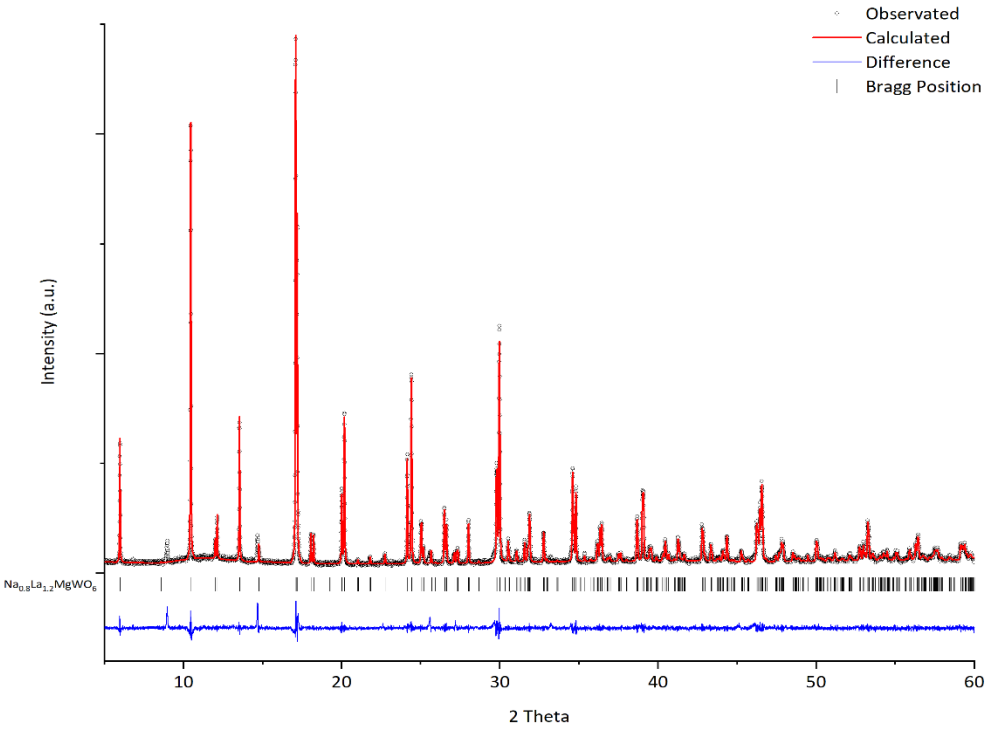

Fig.10: Plot of the Rietveld refinement of the average C2/m structure of $Na_{0.8}La_{1.2}MgWO_6$ against X-ray data. Observed data (black point), calculated pattern (red line) and difference (blue line) are reported. The thick marks(bottom) indicate the Bragg position of the main phase in black.

To solve the superstructure of these two no-stoichiometric phases, firstly, were defined the modulation vector ***q*** and the reflection conditions in 4D-space by studying the reciprocal space of the 3D-ED data. The modulation vector for the satellite indexing in the two phases is very similar and has a single component $q=0.172(2)a^*$ for $Na_{0.8}La_{1.2}$ and $q=0.174(1)a^*$ for $Na_{1.2}La_{0.8}$. The reflection conditions of the satellites in both cases are *hklm: h+k=2n* and *h0lm:m=2n* consistent with the superspace group *C2/m(α0γ)0s*. We are therefore in the special case in which the third component of the modulation vector ***q*** is equal to zero. With these information was made an attempt at structural resolution using a superspace approach on a complete

3D-ED data set. In both cases we were successful, and the modulation was described as in the stoichiometric phase with a sinusoidal function. Even in these cases that modulation involves all oxygen atoms except O2.
As can be seen from the wolff sections of the two phases, the modulation is very similar between the three phases, what changes is the magnitude of the displacement with respect to the average position. In the case in which we have an excess of sodium there is a greater displacement and a clearer position of the oxygen in the modulation period, but not enough to be described with a crenel function as in the case of the $NaLaCoWO_6$ phase.

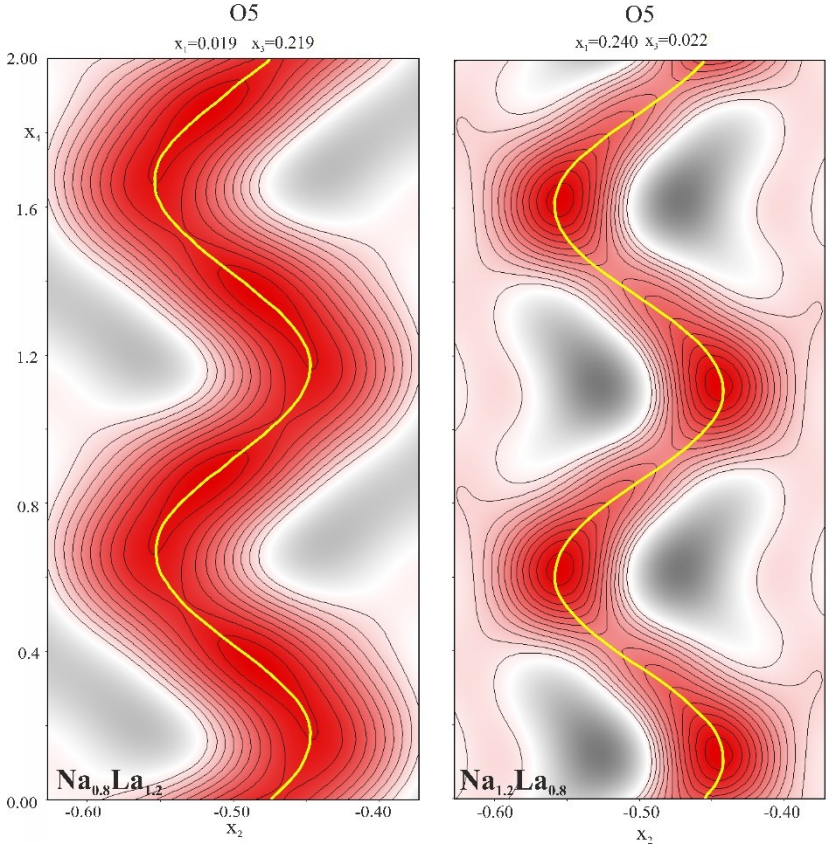

Fig.11: F_{obs} Fourier maps of the (3+1)D super-space around the to the average position, projected on the $x_{2–x4}$ planes. Horizontal axes display x_2 fractional coordinates (y coordinates) and vertical axes correspond to x_4; The fitted atomic modulation functions, represented as continuous yellow lines. Left the O5 in $Na_{0.8}La_{1.2}MgWO_6$ phase, right the O5 in $Na_{1.2}La_{0.8}MgWO_6$.

Also in these two cases, if we study the position of the O5 in the structure, we observe that the modulation does not cause a change variation of the order of inclination either case but only a change the magnitude of the relative inclination between the octahedra of Tungsten and Magnesium.

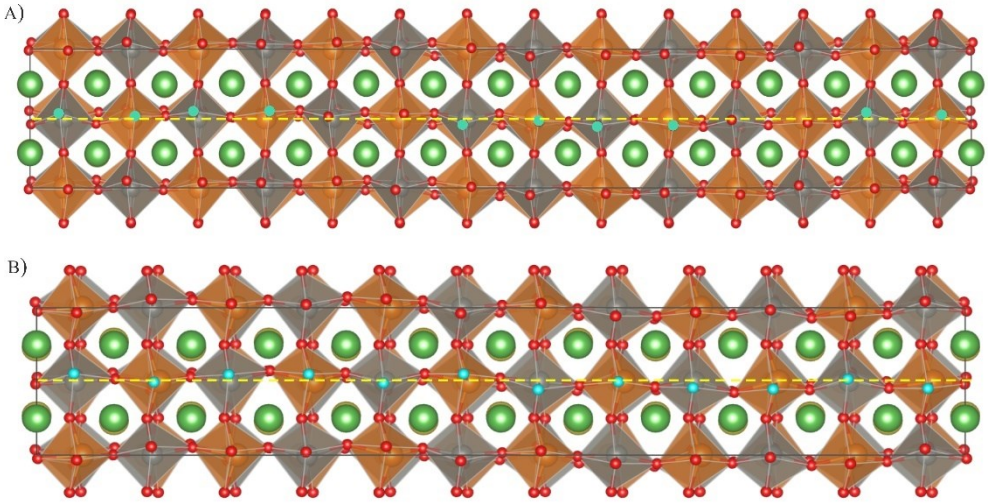

Fig.12: A) One dimensional octahedral tilt twining along direction a of $Na_{0.8}La_{1.2}MgWO_6$, with cell size $13a_p$ the twofold axis in yellow. B) One dimensional octahedral tilt twining along direction a of $Na_{1.2}La_{0.8}MgWO_6$, with cell size $13a_p$ the twofold axis in yellow.

As can be seen from Figure 5, the displacement of the oxygen along a modulation period does not cause a change in the order of the reciprocal rotations but causes a more or less marked displacement of O5 above or below the twofold axis. We note the different behavior of the O5 displacements between the two phases as it was already clear from the Wolff sections.

The refinement parameters for modulation structure are show in table 6:

Table 6: Crystal Data for the modulated structures of the phases with excess and defect of sodium.

	$Na_{0.8}La_{1.2}MgWO_6$	$Na_{1.2}La_{0.8}MgWO_6$
Crystal data		
Crystal System	*Monoclinic*	*Monoclinic*
Superspace Group	*C2/m(α0γ)0s*	*C2/m(α0γ)0s*
a,b,c (Å)	*7.801, 7.812, 7.893, 90.120*	*7.804, 7.815, 7.895, 90.153*
Data collection		
Source	*Electrons*	*Electrons*
No. of observed reflection	*346*	*403*
Range ok h, k, l, m	$h= -6 \rightarrow 6$, $k=-6 \rightarrow 6$, $l=-6 \rightarrow 6$	$h= -6 \rightarrow 6$, $k=-6 \rightarrow 6$, $l=-6 \rightarrow 6$
Refinement		
$R[F^2 > 2\sigma(F^2)]$, $wR(F^2)$ *main reflection*	*0.071*	*0.064*
$R[F^2 > 2\sigma(F^2)]$, $wR(F^2)$ *Satellite reflection*	*0.245*	*0.233*
No. of Reflection	*784*	*403*
No. of Parameters	*35*	*29*

4.2.7 Modulation and composition

The study of these three phases highlights that the modulation is not linked to the Na/La balance in the structure. Therefore, it can be excluded that the modulation in this compound is compositional as has been proposed in previous studies[23]. In analogy with $NaLaCoWO_6$ phase, the modulation is essentially displacive causing a change in the reciprocal positions of the octahedra of cations B and B'. For $Na_{1.2}La_{0.8}MgWO_6$ the excess of the Na is not incorporated in the double perovskite but it is segregated in Na-rich secondary phases.

Table 7: Occupancy factors for the La and Na sites in the three monoclinic Mg-based ordered perovskites

Nominal composition	*La site occupancy*	*Na site Occupancy*
$NaLaMgWO_6$	*1*	*1*
$Na_{1.2}La_{0.8}MgWO_6$	*La 0.94(3) / Na 0.06(5)*	*1*
$Na_{0.8}La_{1.2}MgWO_6$	*1*	*La 0.01(5) / Na 0.99(3)*

In fact, as evidenced in the Table 7, albeit the nominal composition is off-stoichiometric, the Na/La ratio is close to the ideal 1:1 condition. Hence the net separation of the heterovalent A and A' ions into two layers represents a strong structural constraint for the stability of the doubly ordered perovskite. This result provides the confirmation that the layered structure is accessible only with the insertion of ions differently charged with an equivalent stoichiometric balance. Therefore, deviations from the 1:1 ratio are allowed for minute compositional changes. If the stoichiometry departs from the $NaLaMgWO_6$ formula, the modulation causes a change in the mutual rotation order of the octahedral of Mg and W. Differently to what observed with Co-based compound, the best fitting is achieved with a sinusoidal function, rather than the crenel type [24], for the atomic positions of oxygens. Having only 3D-ED data, the refinement of the wave-like positional modulation of the oxygens requires further structural investigations. To validate the modulation of the oxygens positions diffraction experiments with neutron source are mandatory. We noticed that a limited compositional disorder on site A or A'

returns a stronger distortion of the octahedral coordination, if compared to the stoichiometric compound. For instance, the ED data provided a preliminary description of the structural modulation and demonstrated that the compositional modulation in doubly ordered perovskites is excluded.

4.2.8 Final Remarks

We have shown that the $NaLaCoWO_6$ compound has a modulated phase at room temeprature with an incommensurate out of phase tilting along the a and c directions. The 3D electron data was used in synergy with neutron and X-ray diffraction experiments for the structure solution of the incommensurate phase within the superspace formalism. In literature, the incommensurate modulation in doubly ordered perovskites has been interpreted as originated by the distribution of the A and A' ions to form alternated off-stoichiometric domains composing a checkerboard contrast[23,27] observed in HREM experiments. In the combined XRD/TOF-NPD structural refinements, the La and Na sites are fully occupied and mixing of the two heterovalent ions or randomly distributed vacancies are excluded. Furthermore, the identified impurities are not in contrast with the occurrence of the 1:1 ratio of the La and Na in the doubly ordered perovskite. Thus we can conclude that the modulation is fully displacive and the nominal composition and cationic ordering is maintained in the crystal structure with a large extent. The same indication comes out from the structural analysis of the $(NaLa)MgWO_6$ compounds with variable Na/La ratio. Also for NaLaMgWO6, the structural modulation was described with the (3+1)-dimensional *C2/m(α0γ)0s* space group and exhibits a displcive character defined by incommensurate octhahedral tilting pathways. Therefore the actual crystallographic study excludes the occurrence of irregular distribution of A and A' cations in $AA'BB'O_6$ perovskites as the origin of the incommensurate distortion. Future diffraction experiments carried out from low to room temperature might provide valuable insights of the thermal stability of the incommensurate domains having a different tilting framework.

4.3 References

1. Borchani, S. M., Koubaa, W. C. R. & Megdiche, M. Structural, magnetic and electrical properties of a new double-perovskite $LaNaMnMoO_6$ material. *Royal Society Open Science* **4**, (2017).

2. Gemmi, M. & Lanza, A. E. 3D electron diffraction techniques. *Acta Crystallographica Section B: Structural Science, Crystal Engineering and Materials* **75**, 495–504 (2019).

3. Mugnaioli, E. *et al.* Ab initio structure determination of vaterite by automated electron diffraction. *Angewandte Chemie - International Edition* **51**, 7041–7045 (2012).

4. Steciuk, G., Palatinus, L., Rohlíček, J., Ouhenia, S. & Chateigner, D. Stacking sequence variations in vaterite resolved by precession electron diffraction tomography using a unified superspace model. *Scientific Reports* **9**, (2019).

5. Nederlof, I., van Genderen, E., Li, Y. W. & Abrahams, J. P. A Medipix quantum area detector allows rotation electron diffraction data collection from submicrometre three-dimensional protein crystals. *Acta Crystallographica Section D: Biological Crystallography* **69**, 1223–1230 (2013).

6. Vincent, R. & Midgley, P. A. Double conical beam-rocking system for measurement of integrated electron diffraction intensities. *Ultramicroscopy* **53**, 271–282 (1994).

7. Chapon, L. C. *et al.* Wish: The new powder and single crystal magnetic diffractometer on the second target station. *Neutron News* vol. 22 22–25 (2011).

8. Petříček, V., Dušek, M. & Palatinus, L. Crystallographic Computing System JANA2006: General features. *Zeitschrift für Kristallographie - Crystalline Materials* **229**, 345–352 (2014).

9. Campbell, B. J., Stokes, H. T., Tanner, D. E. & Hatch, D. M. ISODISPLACE: A web-based tool for exploring structural distortions. *Journal of Applied Crystallography* **39**, 607–614 (2006).

10. Hatch, D. M. & Stokes, H. T. INVARIANTS: program for obtaining a list of invariant polynomials of the order-parameter components associated with irreducible representations of a space group. *Journal of Applied Crystallography* **36**, 951–952 (2003).

11. Glazer, A. M. The classification of tilted octahedra in perovskites. *Acta Crystallographica Section B Structural Crystallography and Crystal Chemistry* **28**, 3384–3392 (1972).

12. Sekiya, Tadashi. Yamamoto, Tetsuo. Torii, Y. Cation Ordering in $NaLaMgWO_6$ (1984).

13. Petříček, V., van der Lee, A. & Evain, M. On the use of crenel functions for occupationally modulated structures. *Acta Crystallographica Section A* **51**, 529–535 (1995).

14. Shankar P N, R. *et al.* A-Site and B-Site Cation Ordering Induces Polar and Multiferroic Behavior in the Perovskite NaLnNiWO6(Ln = Y, Dy, Ho, and Yb). *Chemistry of Materials* **32**, 5641–5649 (2020).

15. P N, R. S. *et al.* Structural, Magnetic, and Electrical Properties of Doubly Ordered Perovskites $NaLnNiWO_6$(Ln = La, Pr, Nd, Sm, Eu, Gd, and Tb). *Journal of Physical Chemistry C* **125**, 6749–6757 (2021).

16. De, C. & Sundaresan, A. Nonswitchable polarization and magnetoelectric coupling in the high-pressure synthesized doubly ordered perovskites $NaYMnWO_6$ and NaHoCoW O6. *Physical Review B* **97**, 214418 (2018).

17. Fukushima, T., Stroppa, A., Picozzi, S. & Perez-Mato, J. M. Large ferroelectric polarization in the new double perovskite $NaLaMnWO_6$ induced by non-polar instabilities. *Physical Chemistry Chemical Physics* **13**, 12186–12190 (2011).

18. Retuerto, M. *et al.* Polar and Magnetic Layered A-Site and Rock Salt B-Site-Ordered $NaLnFeWO_6$ (Ln = La, Nd) Perovskites. *Inorganic Chemistry* **52**, 12482–12491 (2013).

19. King, G., Wayman, L. M. & Woodward, P. M. Magnetic and structural properties of $NaLnMnWO_6$ and $NaLnMgWO_6$ perovskites. *Journal of Solid State Chemistry* **182**, 1319–1325 (2009).

20. Zuo, P., Darie, C., Colin, C. v. & Klein, H. Investigation of the Structure of the Modulated Doubly Ordered Perovskite NaLaCoWO 6 and Its Reversible Phase Transition with a Colossal Temperature Hysteresis. *Inorganic Chemistry* **58**, 81–92 (2019).

21. Lausi, A. *et al.* Status of the crystallography beamlines at Elettra. *The European Physical Journal Plus 2015 130:3* **130**, 1–8 (2015).

22. Van Smaalen, S. Incommensurate crystal structures.

23. García-Martín, S., Urones-Garrote, E., Knapp, M. C., King, G. & Woodward, P. M. Transmission electron microscopy studies of $NaLaMgWO_6$: Spontaneous formation of compositionally modulated stripes. *Journal of the American Chemical Society* **130**, 15028–15037 (2008).

24. Evain, M., Petricek V. Crenel Functions and Aperiodic Structure Determinations. **305**, 43–48 (2010).

25. RF, E. Radiation Damage to Organic and Inorganic Specimens in the TEM. Micron (Oxford, England: 1993) 2019, 119, 72–87.

26. Jiang, N.; Su, D.; Spence, J. C. H.; Zhou, S.; Qiu, J. Electron Energy Loss Spectroscopy of Na in Na, Na_2O, and Silicate Glasses. Journal of Materials Research 2008, 23 (9), 2467– 2471. https://doi.org/10.1557/JMR.2008.0296.

27. M. W. Licurse. TEM Studies of Modulated Mixed A-site Perovskites, Accessible Penn Dissertations (2013).

5. State of Art of Metal organic frameworks

5.1 General features of MOFs

Metal-organic structures (MOFs) are a class of materials that was defined in the last decades of the 20th century. Their main peculiarity that makes them unique is to be at the same time crystalline and porous where the porosity (ϕ) is defined as the ratio between the volume occupied by the pores (Vp) and the total volume[1]:

$$\phi = \frac{V_p}{V}$$

The porosity is a peculiarity that is rarely found in solid materials, because the atoms usually tend to arrange themselves as compactly as possible to maximize their mutual attractive forces. Porous materials are classified into three categories, according to the size of their pores[2]:

- Microporous with pores smaller than 2 nm.
- Mesoporous with pores comprised between 2 and 50 nm.
- Macroporous with pores dimensions larger than 50 nm.

The porosity of the MOFs is evaluated with a surface area analysis using the BET approach (Brunauer-Emmett-Teller), in which the gas absorption is estimated by varying the gas pressure at constant temperature[3]. Therefore, this characteristic allows the MOFs to interact with the external environment not only through the external surface but also with their internal mass through the adsorption mechanism[4] . This capacity is based on several processes[5]:

- Physisorption, in which physical interactions are established between the adsorbate and the material. The strength of these interactions is related to the surface characteristics of the two substances (polarizability and quadrupole moment).

- Chemisorption in which the interaction is mediated through chemical bonds that are formed between the material and the adsorbate.

- Size exclusion, that is an ability of porous materials to separate two species from a mixture preventing the adsorption of larger molecules, thanks to the dimensional difference between the molecules and the pore.

Thanks to these interesting characteristics, that are strictly connected to the high porosity that in MOFs can exceed 50%[6], and to their obvious numerous applications, international research is enormously interested in the synthesis of new MOFs.

From the chemical point of view MOFs are organic-inorganic coordination compounds, composed of positively charged metals, which are coordinated with neutral or negatively charged organic linkers. These linkers usually coordinate the metals using nitrogen or oxygen atoms that allow a directionality of the metal-ligand bonds. The unit formed in this way by the metal and the organic ligand is called Secondary Building Units (SBU). First period transition metals are often used for MOFs synthesis, although, in principle, all metal ions could be suitable for MOFs synthesis[7]. Depending on the topology and on the functional groups of the organic linker, different structures with different pore shapes and different unit cells can be obtained in each synthesis. One of the earliest examples of MOF is known as MOF-5 and was synthesized by Yaghi et al. in 1999[8] (figure 1). In this MOF, the metal node is composed by four ZnO_4 tetrahedra that make up a supertetrahedral structure. They form the SBU with the carboxylate groups which are bridging the different tetrahedra. These SBUs are linked together by the organic linker 1,4-benzenedicarboxylate (BDC), to form a cubic crystal structure with a space group $Fm\bar{3}m$. Since the MOF is a modular structure, starting from the synthesized MOFs, one can "customize" its structure either by changing the metal species of the SBU and/or the organic linker to obtain different topologies. Therefore, the resulting crystalline structures are extremely variable, and the physicochemical features can be uncountable.

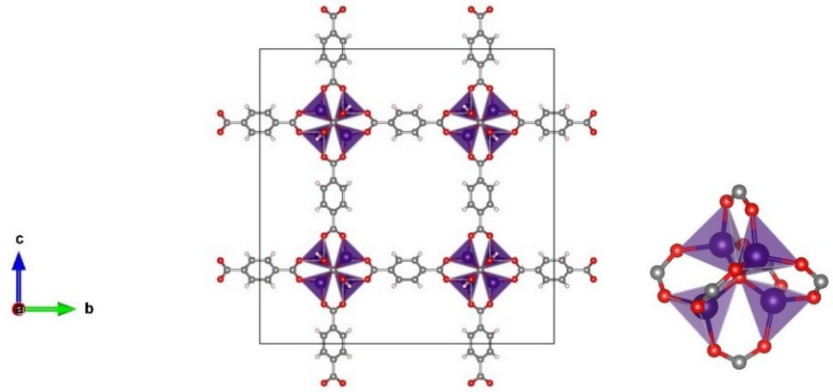

Figure 1: The cell unit of MOF-5, viewed along the crystallographic a-axis on the and the SBU. The tetrahedrally coordinated Zn atoms are indicated by the purple polyhedral, carbon atom in grey and oxygen atoms in red.[8]

Generally, the channels of the MOFs do not remain empty, but are occupied by small molecules called guests (e.g. water, synthetic solvents etc.) which theoretically can be removed from the channels through physical processes such as vacuum treatment, heating or with an exchange process with other guests. Based on these characteristics, the MOFs have been classified into three generations based on their behavior with respect to the absorption and desorption of the guest:

- First generation MOFs: they are not stable and lose the porosity once the guest is removed.

- Second generation MOFs: they are composed of a rigid structure, which remains stable upon absorption and desorption of guest molecules and the porosity is maintained during treatments.

- Third generation MOFs: they are characterized by a high flexibility of the crystal structure and can undergo to reversible changes in the shape and dimensions of the pores.

The latest generation show significant and reversible changes in the structure and consequently in the size of the pores as a function of numerous external

stimuli such as electric fields, iterations with the adsorbate or mechanical and photochemical thermal stimuli. This flexibility is allowed by the possible degrees of freedom that the organic linker possesses or distortion of the coordination angles between the metal and the linker. As a consequence, these materials have large applications in the development of an innovative class of sensors.[9]

5.1.1 Magnetism and Metal-Organic Framework

In recent years, MOFs have been used as a new chemical platform with which to create a new generation of magnets. In recent decades, the magnetic characteristics have been the preserve of inorganic solids only. Conventional magnets are typically intermetallic compounds or oxides based on rare earths and transition metals[10] in which the short bond between its components allows for an efficient long-range interaction between the spin centers[11–13].. Although these materials have a high magnetization[10] their chemical nature limits their tunability and flexibility, so the creation of new magnetic inorganic phases with targeted properties is very difficult. On the other hand, metal-organic structures have numerous advantages over inorganic materials. Such as the presence of a rigid and crystalline structure that preserves the character of porosity and allows a post-synthetic modification of the organic and inorganic components. It has been shown in several studies that some molecular-based magnets exhibit multifunctional properties[14] such as the long-range magnetic order and electrical conductivity[15–17], these characteristics combined with their low density make them ideal for using permanent and lightweight magnets for electrical devices and energy technologies. Despite these numerous advantages that molecular magnets possess over solid-state inorganic materials, most of them suffer from low operating temperatures. So, a very interesting focus for international research is the development of molecular-based magnets that work at high temperatures to be used for technological applications and metal-organic structures are an ideal and not yet fully explored chemical platform. The long-range magnetic order requires interactions along different directions[10,18] cited and the framework within the MOF is ideal for allowing interactions between

the different spin centers by exploiting the organic linkers, so as to generate an order long range.

In this new approach, the advantages provided by coordination chemistry are exploited for the synthesis of new MOFs that allow the synthesis of materials with a high magnetic anisotropy. Therefore, MOFs are materials that can combine magnetic characteristics with high porosity, which are generally hostile to each other. Because the magnetic exchange interactions require short distances between the different spin centers while the porosity is favored using extended organic linkers. However, as already mentioned, the range of usable woods is very wide and versatile, and it has already been shown that the use of the right organic binder and the right synthesis strategy allows the creation of both magnetic and porous structures. In the light of these studies, in this thesis we tried to synthesize a MOF that combines these two characteristics using a short organic linker, a new synthesis method and the presence of two different metal centers inside in the same structure to favor the interactions between the spins. Furthermore, three structures were used as a reference for the design of these two bimetallic MOFs so as to demonstrate once again the flexibility that these metal-organic structures possess.

Reference Structure	***New Bimetallic MOFs***
$[Zn_3(OH)_2(btca)_2]DMF{\cdot}4H_2O$	$[M_{10}(OH)_4(H_2O)_2(DEF)_2(btca)_8]$ with M=Co,Mn
$[Mn_3(OH)_2(btca)_2(DMF)] \cdot DMF$	$[M_{10}(OH)_4(H_2O)_2(DMF)_2(btca)_8]$ with M=Zn,Co
$[Co_3(OH)_2(btca)_2]{\cdot}3.7H_2O$	

5.2 Synthesis of MOFs

The synthesis used in this thesis is the solvothermal method, which consists in dissolving a metal salt and the organic linker in suitable solvents and applying high temperatures to the solution for a variable time interval in a sealed container. The containers used for our synthesis are made by an external stainless-steel autoclave, which contains sealed Teflon containers (polytetrafluoroethylene, PTFE) where the solution is loaded (figure 2). The autoclave is placed in an owen and is kept closed for the entire duration of the experiment. With this method it is ensured that the chemical reaction takes place at a temperature higher than the boiling temperature of the solvent and at pressures between 1 and 30 bar [29]

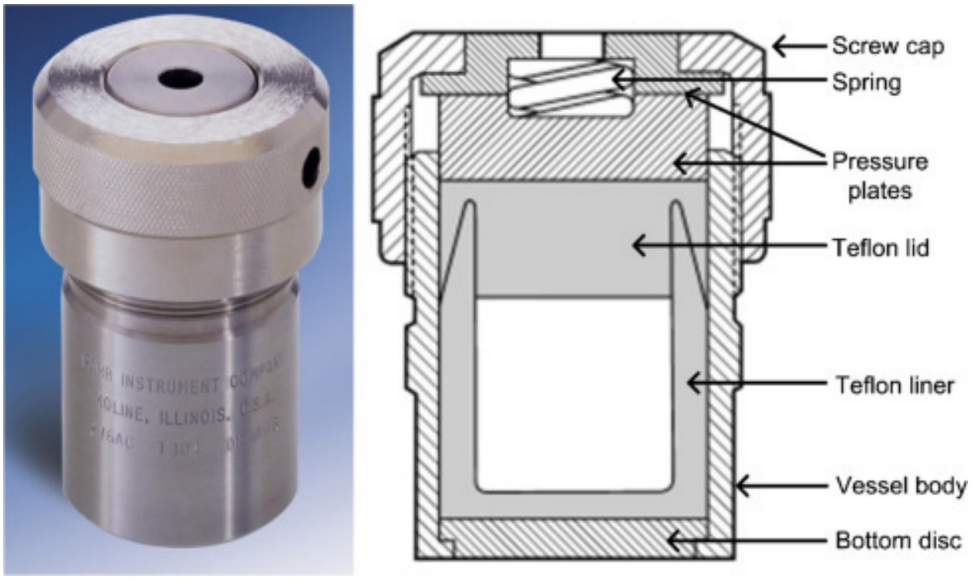

Figure 2: A stainless steel autoclave for solvothermal synthesis. On the right, a scheme reporting its components within its section[29].

5.2.1 Bimetallic MOFs

In recent years, researchers have tried to synthesized MOF with at least two different types of metals in the metallic clusters: the bimetallic MOFs. The simultaneous presence of two chemically different metals allows to improve some properties of MOFs, such as greater affinity and/or selectivity for certain molecules, a better stability, different redox activity[19,20]. The two different metal ions can be ordered in different ways in the crystal structure (Figure 3), and the corresponding MOFs can be classified in two main groups[19]:

- Solid-solution structures, where the two metal ions show a homogeneous (ordered or disordered) distribution inside the crystal.

- Core-shell structures, where the inner part and the external part of the MOF display different chemical composition.

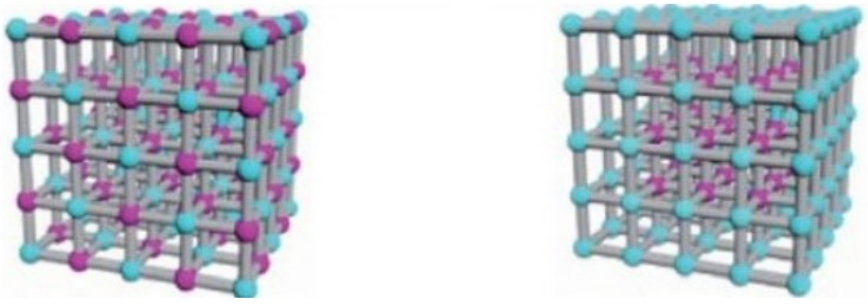

Figure 3: A representative scheme of solid-solution (on the left) and core-shell (on the right) bimetallic MOFs[19].

These new bimetallic MOFs can be synthesized in several ways. By direct synthesis, as the standard MOFs, which consists in inserting two different metal salts in the same container in the synthesis phase. This technique has been used in several cases[21,22] obtaining Zn-based MOF-5 and MOF-74 with various content of Co. To achieve this purpose different molar ratios of the two metal salts (for Co, $Co(NO_3)_2 \cdot 6H_2O$) in the synthesis phase were used.

From the chemical analysis of the obtained samples, it was deduced that the isomorphic substitution of the metal ions occurs to a maximum degree of 1Co atom/Zn4O cluster on average in the SBU[21]. The cobalt ions in the structure show octahedral coordination, completed also by oxygen atoms belonging to the solvent molecule, but once the MOF is evacuated, the cobalt cations change to a tetrahedral coordination. The cobalt content in the MOF structure has been shown to have a significant effect on the ability of the porous structure to adsorb CO_2, H_2 and CH_4. From this analysis it was proved that the Co^{2+} cation has an important role in the absorption of the gas even if they are not directly exposed to it[22]. Another emerging technique for obtaining isoreticular bimetallic MOFs is post-synthesis cation substitution, also called transmetalization. The partial exchange of the metal ionic species is carried out by soaking the monometallic MOF in a solution containing a different metal ion. This method has led to both partial and total replacements [20,23]. The successful application of this method on a metal-organic structure is dated back to 2007 and was carried out by Dica and Long[24]. In this case the Mn^{+} ion was substituted with various metal ions (Li^{+}, Cu^{+}, Fe^{2+}, Co^{2+}, Zn^{2+}, Ni^{2+}, Cu^{2+}) by dipping for one week the compound in concentrated solutions of LiCl, MCl_2 (M = Fe^{2+}, Co^{2+}, Zn^{2+}, Ni^{2+}, Cu^{2+}) or $[Cu\text{-}(CH_3CN)_4]PF_6$ and using methanol or acetonitrile as solvents, obtaining a partial substitution of the metal ions ($0.017 < M/Mn < 3.999$). The factors that may promote cation substitution are both the high temperature and the immersion time, and it can be influenced by the concentration of the solution and the solvent used[25]. Substitution of ions by immersion but also synthesis of bi-metallic MOF with a one-pot synthesis are more likely to be successful if the two metals have similar charge and ion radius[19,20]. For the complete characterization of these compounds many and numerous specific techniques are required. Indeed, it turns out that is very difficult to determine the distribution of the two metal ions in the crystalline structure. In a compound of this type, it is possible to create different crystalline domains within the bulk material, in which there may be the coexistence of the same SBU or the formation of distinct SBU. To distinguish between these two possibilities, a combinations of characterization techniques such as electron microscopy, X-ray diffraction (XRD) and energy dispersion (EDS) and others are needed.

5.2.2 Reference of bimetallic MOFs

As inspiration for the synthesis of bimetallic MOFs we took into consideration the research of Tu Pang et al.[26] who synthesized a mesoporous MOF of Zn(II)/Cu(II)-H_2PyC (4-pyrazolecarboxylic acid) called FDM-3. This structure is built from three different SBUs, with triangular, octahedral and pyramidal geometries with a square base (figure 9) and was synthesized with solvothermal methods.

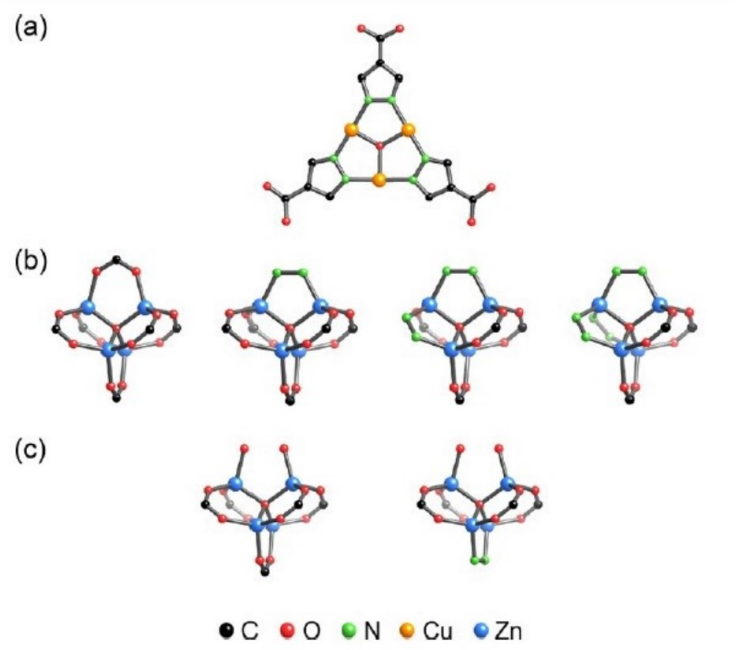

Figure 9: The SBUs geometries of the FDM-3 MOF structure. a) triangular $Cu_3(OH)(PyC)_3$ SBU, b) octahedral $Zn_4O(COO)_3R_3$ SBUs, c) square pyramidal SBUs $Zn_4O(COO)_4R$ (R = COO or NN) [26].

The SBUs are arranged in four types of polyhedral cages and constitute the basic units of the crystalline structure which has a cubic symmetry with a space group $Fm\bar{3}m$.The different SBUs of FDM-3 are shown in figure 9, and the organization of the polyhedral cages that make up the unitary cell of the MOF are shown in figure 10.

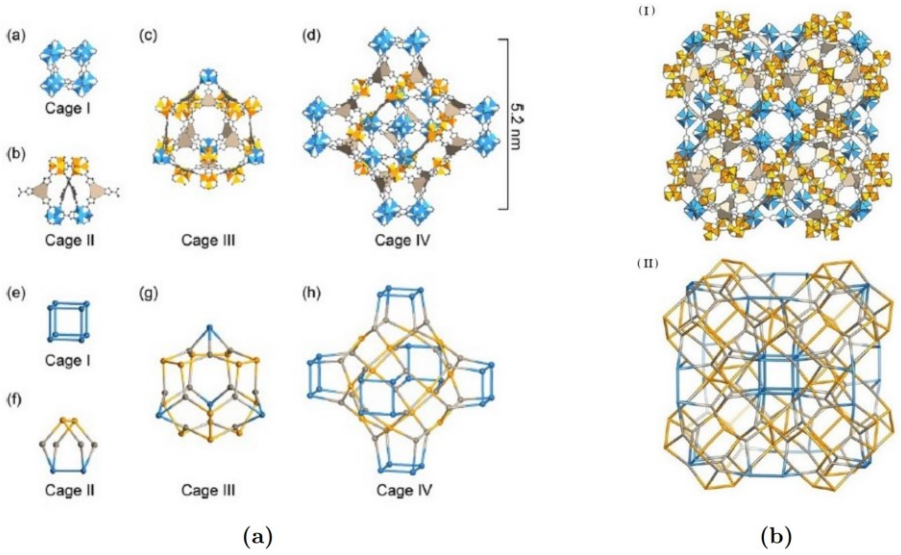

Figure 10: (a-d) Structure of cages in FDM-3 crystal structure, (e-h) ball and stick diagrams of cages a-d. (I) Unit cell of FDM-3 MOF structure, (II) ott underlying net, with light brown triangular SBU, blue octahedral SBU, orange square pyramidal SBU[26].

It was verified that the two atoms of Zn in each of the SBUs with square pyramidal geometry and all Cu ions in the SBU with triangular geometry are unsaturated active sites. Thus, it was possible to link these sites with new organic molecules [4-aminobenzoic acid (NH_2−BC), 1,8-diazanaphthalene, and pyrazole]. Moreover, this type of MOF showed catalytic properties; in fact, the FDM-3 compound was used for the synthesis of Silver nanoparticles (AgNP). A high absorption of NP of silver was observed in the first 30 minutes (16.7 wt%), which is not due to the mesoporosity of the material but to the periodic arrangement of the active atoms of zinc and copper within the structure, which facilitate the redox reactions that causes the formation of NPs.

5.2.3 Challenges in Our MOFs

In this thesis, we started from monometallic MOFs with general formula [$M^{II}_3(OH)_2(btca)_2$] (where M = Zn^{2+}, Mn^{2+} and btca = benzotriazolide-5-carboxylato) were considered because they have interesting characteristics from a structural, chemical-physical point of view and functional for pollutants gas absorption[27]. The organic linker (H_2btca) used in the synthesis is depicted in figure 4:

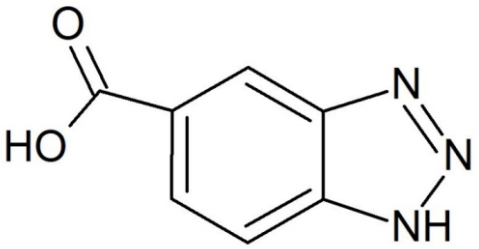

Figure 4: Chemical structure of H_2btca molecule. In the MOF the compound is found in its deprotonated state.

This molecule is planar, with the exception of the oxygen atoms that compose the carboxylic group which be located outside the plane formed by the two condensed cycles. This organic molecule, once deprotonated, acts as a divalent linker and can form five bonds using nitrogen and oxygen atoms. In this thesis we used as coordinative centers the transition metal ions Zn^{2+}, Mn^{2+} and Co^{2+}, in combination with btca linker. It has been widely demonstrated that the selected metals easily form crystalline structures with this type of ligand [28]. In order to obtain bimetallic frameworks with bcta as crosslinker we considered some established structures based on a single metallic center. The following sections describe some mono- or bimetallic known systems that we adopted as reference structures to obtain new combination in the same MOF.

5.2.4 Reference Zn-MOF

Our strategy to develop a bimetallic MOF has been to start with as reference structure, the compound synthesized by Xiao, Juan et al.[28]. They report the synthesis of a porous zinc-based MOF applying the solvothermal method. The compound was indicated with the name MOF(Zn)-1, with the formula: $[Zn_3(OH)_2\text{-}(btca)_2]DMF{\cdot}4H_2O$ (DMF = N, N-dimethylformamide, H_2btca = benzotriazole 5-carboxylic acid). In this structure, the SBUs are composed by two zinc atoms connected to three carboxylate, triazolate and hydroxyl groups, as can be seen from Figure 5.

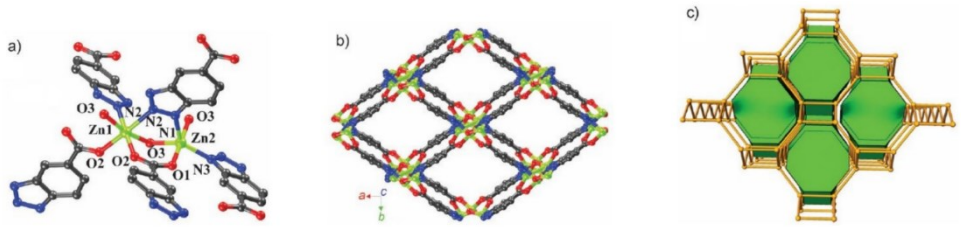

*Figure 5: a) Zn coordination environment, b) MOF(Zn)-1 porous structure, c) the **sra** rod-shaped SBU net[28].*

Overall, the structure has 1D pores with nanometric dimensions and with a zig zag packing of the SBUs, and with an underlying net with order *sra*, according to the decomposition system of the crystal structure studied by O'Keeffe and Yaghi[30] . The metal backbone is directed along the channels and consists of two independent zinc atoms in the unit cell. The first has octahedral coordination, while the other has triangular bipyramidal coordination. Therefore, this last atom presents a site accessible to the possible guest molecule (figure 5). Although this MOF is composed of rigid SBUs, it exhibits the so-called "breathing" behavior as was observed that this structure was capable of varying the coordination angles between metal-linkers. It was deduced that the SBUs therefore behave as hinges and this variation in the coordination angles causes a modification of the unit cell and consequently of the porosity. This behavior was observed by O'Keeffe, who first noted that rod-shaped MOFs exhibit a "breathing" effect[30]. As a consequence, if the solvent is removed from the channels, different forms of

the MOF with different pore sizes were obtained. The channels when empty can shrink up to 55% of the initial volume of 1084.3 $Å^3$, but all the various structures belong to the same monoclinic space group *C2/c* (figure 6). Another feature that MOF-(Zn)-1 possesses is a photoluminescent response induced by the presence of the host molecules. Hence, it was showed that dynamic respiration improves the sensitivity and selectivity of the luminescent signal, since the presence of the host causes the variation of the volume and unit cell and consequently the luminescent response. Therefore, it was thought that by varying the metallic sites and the organic linkers it's possible to synthesize an infinite series of these materials that could be applied as precise and specific sensors for the detection of pollutants or for biomedical applications[28,31,32].

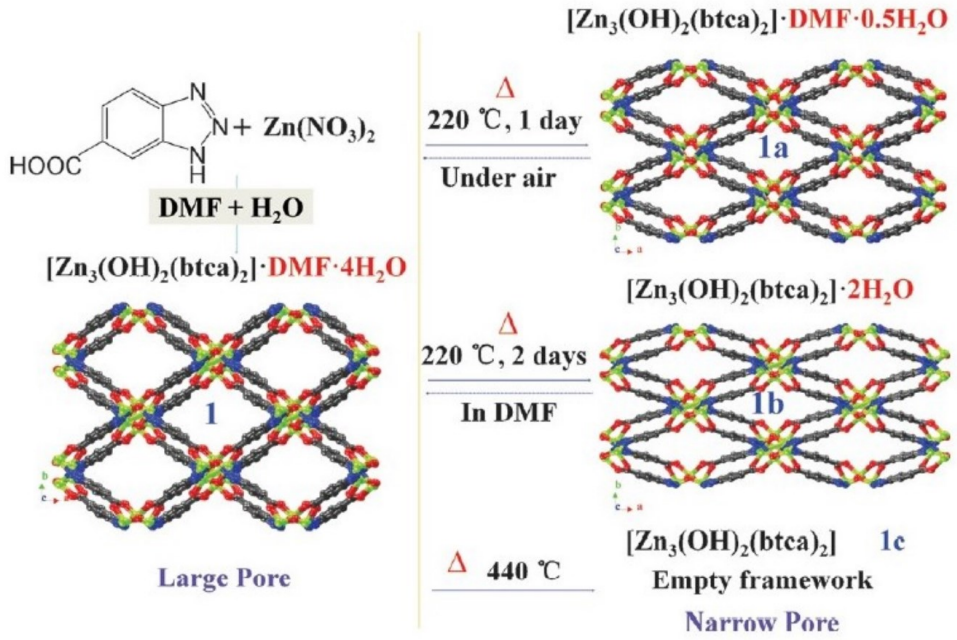

Figure 6: Structural switching of MOF(Zn)-1. On the right, the structures resulting from the different solvent removal procedures are shown. The porosity variation and the unit cell modification are visible[28].

5.2.5 Reference Mn-MOF

The previous Zn-based MOF has other isotopological structures, where the metal ion consists of cobalt or manganese called MOF(Co)-1[33] and MOF(Mn)-1[34] respectively. The latter was taken as a reference for the synthesis of the second bimetallic MOF. The structure of MOF(Mn)-1 is porous and triclinic (*P1*), and it also appears, as in the previous case, with 1D pores defined by *btca* molecules that connect the metal nodes. The asymmetric unit of this MOF consists of three symmetrically independent Mn^{2+} ions, two *btca* molecules, two hydroxyl groups and two synthesis solvent molecules (DMF - N,N dimethylformamide) as shown in figure 7.

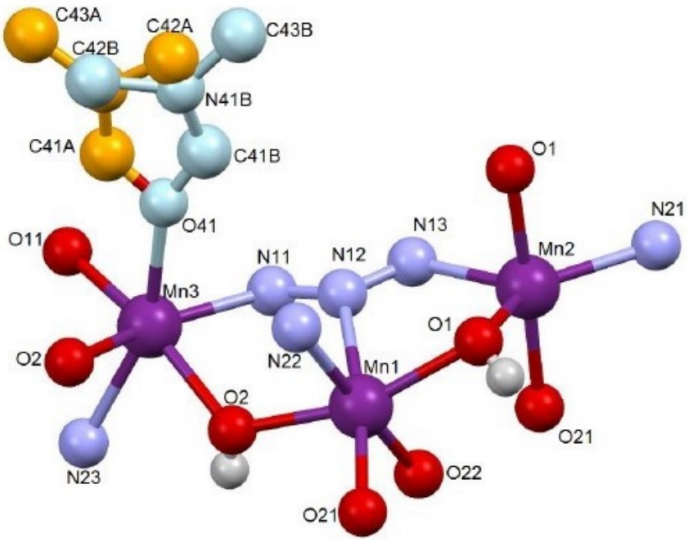

Figure 7: Metal backbone of MOF(Mn)-1 structure and coordination environment of Mn atoms. The coordinated btca molecule is displayed in both its possible orientations, in white and yellow, respectively.

One of the manganese ions is penta-coordinated with two hydroxyl groups, two nitrogen atoms and one oxygen atom belonging to the btca molecule. The other two are hexacoordinated, one is linked to two oxygen atoms belonging to two different linker molecules, to two nitrogen atoms and two hydroxyls, the other is coordinated with an oxygen atom of *btca*, two hydroxyl groups, two atoms of nitrogen and a molecule of DMF that causes a distortion of the

octahedral geometry. The solvent molecule inside the channel can assume different orientations (in figure 8 only one is represented for simplicity) with respect to the metal node.

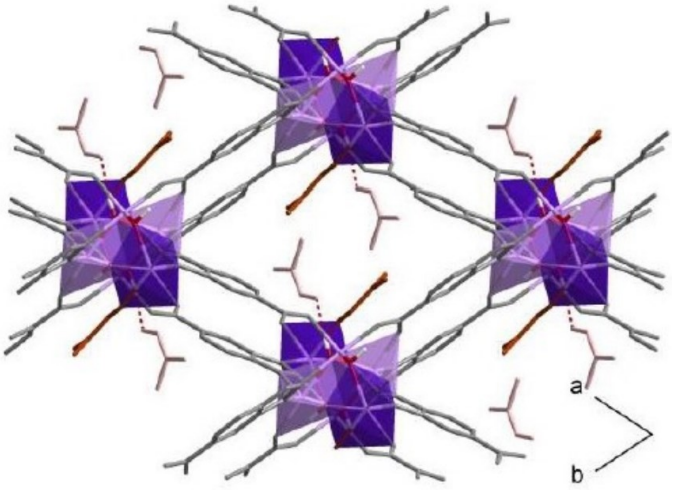

Figure 8: MOF(Mn)-1 structure, view along the c crystallographic direction. Unsaturated metal sites are indicated by light purple polyhedra, while Mn sites coordinated to DMF are represented by dark purple polyhedra[34].

The *sra* topology also allows this particular MOF to display the "breathing" feature, which occurs thanks to the sliding of the *btca* molecule with respect to the M-OH centers. Furthermore, this structure has a greater chemisorption capacity than the other two isoreticular structures (MOF(Zn)-1 and MOF(CO)-1), confirming that the metal species present in the structure plays an important role in the structural properties. This MOF based on manganese, as well as its zinc-based homologue, can have several applications such as in the field of catalysis, detection, storage and also as molecular sieves. In all these cases, the ability of these systems to form coordinative bonds with unsaturated metal sites, easily reachable through the 1D pores, is exploited.

5.3 References

1. Ishizaki, K., Komarneni, Sridhar. & Nanko, M. (Makoto). Porous materials: process technology and applications. 240 (1998).

2. Zhang, X. *et al.* A historical overview of the activation and porosity of metal–organic frameworks. *Chemical Society Reviews* **49**, 7406–7427 (2020).

3. Lowell, S., Shields, J. E., Thomas, M. A. & Thommes, M. Characterization of Porous Solids and Powders: Surface Area, Pore Size and Density. **16**, (2004).

4. M.E. Devis. Ordered porous materials for emerging applications. *Nature* **417**, 813–821 (2002).

5. Petit, C. Present and future of MOF research in the field of adsorption and molecular separation. *Current Opinion in Chemical Engineering* **20**, 132–142 (2018).

6. Kaskel. The Chemistry of Metal-Organic Frameworks: Synthesis, Characterization, and Applications (2016).

7. Griffin, S. L. & Champness, N. R. A periodic table of metal-organic frameworks. *Coordination Chemistry Reviews* **414**, (2020).

8. Li, H., Eddaoudi, M., O'Keeffe, M. & Yaghi, O. M. Design and synthesis of an exceptionally stable and highly porous metal- organic framework. *Nature* **402**, 276–279 (1999).

9. A. Schneemann *et al.* Flexible metal–organic frameworks. *Chemical Society Reviews* **43**, 6062–6096 (2014).

10. Gutfleisch, O. *et al.* Magnetic Materials and Devices for the 21st Century: Stronger, Lighter, and More Energy Efficient. *Advanced Materials* **23**, 821–842 (2011).

11. Schnack, J. & de Graaf, C. Ab Initio Modeling and Calculations of Magnetic Properties. *Molecular Magnetic Materials* 447–471 (2016).

12. Piga, F. *et al.* Magnetic properties of a novel family of ferrous cubanes. *Chemical Communications* **48**, 2430–2432 (2012).

13. Miller, J. S. Magnetically ordered molecule-based assemblies. *Dalton Transactions* 2742–2749 (2006).

14. Maspoch, D., Ruiz-Molina, D. & Veciana, J. Old materials with new tricks: multifunctional open-framework materials. *Chemical Society Reviews* **36**, 770–818 (2007).

15. Tokoro, H. & Ohkoshi, S. I. Novel magnetic functionalities of Prussian blue analogs. *Dalton Transactions* **40**, 6825–6833 (2011).

16. Clemente-León, M., Coronado, E., Martí-Gastaldo, C. & Romero, F. M. Multifunctionality in hybrid magnetic materials based on bimetallic oxalate complexes. *Chemical Society Reviews* **40**, 473–497 (2011).

17. Mínguez Espallargas, G. & Coronado, E. Magnetic functionalities in MOFs: from the framework to the pore. *Chemical Society Reviews* **47**, 533–557 (2018).

18. Domb, Cyril. & Green, M. S. *Phase transitions and critical phenomena*. (Academic Press, 1974).

19. Chen, L., Wang, H.-F., Li, C. & Xu, Q. Bimetallic metal–organic frameworks and their derivatives. *Chemical Science* **11**, 5369–5403 (2020).

20. S. Abednatanzi. *et al.* Mixed-metal metal-organic frameworks. *Chemical Society reviews* **48**, 2535–2565 (2019).

21. JA. Botas. *et al*. Cobalt doping of the MOF-5 framework and its effect on gas-adsorption properties. *Langmuir: the ACS journal of surfaces and colloids* **26**, 5300–5303 (2010).

22. Botas, J. A., Calleja, G., Sánchez-Sánchez, M. & Orcajo, M. G. Effect of Zn/Co ratio in MOF-74 type materials containing exposed metal sites on their hydrogen adsorption behaviour and on their band gap energy. *International Journal of Hydrogen Energy* **36**, 10834–10844 (2011).

23. Brozek, C. K. & Dincă, M. Cation exchange at the secondary building units of metal–organic frameworks. *Chemical Society Reviews* **43**, 5456–5467 (2014).

24. Dincă, M. *et al*. High-Enthalpy Hydrogen Adsorption in Cation-Exchanged Variants of the Microporous Metal−Organic Framework $Mn_3[(Mn_4Cl)_3(BTT)_8(CH_3OH)_{10}]_2$. *Journal of the American Chemical Society* **129**, (2007).

25. Jiao, Y. *et al.* Tuning the Kinetic Water Stability and Adsorption Interactions of Mg-MOF-74 by Partial Substitution with Co or Ni. *Industrial and Engineering Chemistry Research* **54**, 12408–12414 (2015).

26. B, Tu. *et al.* Heterogeneity within a Mesoporous Metal-Organic Framework with Three Distinct Metal-Containing Building Units. *Journal of the American Chemical Society* **137**, 13456–13459 (2015).

27. Yue, Y. *et al.* A Flexible metal-organic framework: Guest molecules controlled dynamic gas adsorption. *Journal of Physical Chemistry C* **119**, 9442–9449 (2015).

28. Xiao, J. *et al.* Crystalline structural intermediates of a breathing metal-organic framework that functions as a luminescent sensor and gas reservoir. *Chemistry - A European Journal* **19**, 1891–1895 (2013).

29. Daniela Nunes, Ana Pimentel, Lidia Santos, Pedro Barquinha, Luis Pereira, Elvira Fortunato, Rodrigo Martins - Nanostructures: Synthesis, Properties and Applications. *Metal Oxide Nanostructure*. (2019).

30. M, O. & OM, Y. Deconstructing the crystal structures of metal-organic frameworks and related materials into their underlying nets. *Chemical reviews* **112**, 675–702 (2012).

31. Cui, Y., Yue, Y., Qian, G. & Chen, B. Luminescent Functional Metal–Organic Frameworks. *Chemical Reviews* **112**, 1126–1162 (2011).

32. N, Y. *et al.* Gas detection by structural variations of fluorescent guest molecules in a flexible porous coordination polymer. *Nature materials* **10**, 787–793 (2011).

33. Zhang, X. M., Hao, Z. M., Zhang, W. X. & Chen, X. M. Dehydration-Induced Conversion from a Single-Chain Magnet into a Metamagnet in a Homometallic Nanoporous Metal–Organic Framework. *Angewandte Chemie International Edition* **46**, 3456–3459 (2007).

34. Lanza, A. Material properties, chemical bonding and reactions in metal-organic crystals at high pressure. (2016).

6. Structural study of bimetallic MOFs

6.1.1 Synthesis $[M_{10}(OH)_4(H_2O)_2(DEF)_2(btca)_8]$ with M=Co,Mn

The nitrates of Co and Mn were weighed to have a ratio of the two metals of 2:1, 46.6 mg (0.185 mmol) $Mn(NO_3)_2 \cdot 4H_2O$ and 27.01 mg (0.092 mmol) $Co(NO_3)_2 \cdot 6H_2O$ were dissolved each in 4.5 mL of H_2O MilliQ and added to 3 mL of N,N-diethylformamide (DEF) in which 35 mg (0.34 mmol) had been dissolved. The clear solution was placed in a Teflon-lined Parr reaction vessel and brought to a temperature of 200 °C for 12 hours and slowly cooled for 60 hours. The reaction product appears as needle-shaped purple crystals at the bottom of the Teflon cup in a clear purplish solution. The small purple crystals were washed three times with DEF and left to air dry for crystallographic analyses.

6.1.2 Diffraction Experiments

Precession-assisted 3D ED and energy-dispersive X-ray (EDX) spectroscopy were performed with the Zeiss Libra 120 transmission electron microscope working at 120 kV and equipped with a LaB_6 thermionic source and a Bruker EDX XFlash6T-60 detector at the National Enterprise for nanoScience and nano Technology in Pisa. For the electron diffraction data collections, the samples were ground with an agate mortar and the resulting powder was suspended and sonicated in ethanol and drop-deposited on a carbon coated copper grid. Sequential electron diffraction patterns were collected in nanodiffraction mode with a parallel beam of 150 nm, obtained by selecting a condenser aperture of 5 μm. Data were energy-filtered on the zero-loss peak with an in-column Ω-filter and a slit width of about 20eV[2]. Patterns were collected in stepwise mode with a protocol proposed by Mugnaioli et al.[3]. The precession motion of the electron beam around the optical axis was obtained by a Nanomegas Digistar P1000 device[4]. The semi-aperture of the precession cone was set to 1°. The data collection angular range was up to 120° degrees, with steps of 1°. After each tilt step, for checking the crystal movement, a STEM image was taken, and the electron beam was repositioned back in the same point of the crystal. Diffraction patterns were recorded by an ASI

Timepix single-electron detector[5]. Cell determination, diffraction indexing and intensity extraction were performed with the PETS 2.0 program on data taken from thirty different nanocrystals[6]. The X-ray diffraction measurements were performed with a STOE Stadi P diffractometer equipped with Cu-$K\alpha_1$ radiation, a STOE&Cie Johansson monochromator and a Dectris MYTHEN2 1 K detector. The X-ray analyses have been performed in transmission geometry, the sample were ground and placed between two sheets of acetate. All structure refinements were performed with the Jana2006 software[8]. The electron diffraction data has been treated within the kinematical approximation.

6.1.3 Structure of $[M_{10}(OH)_4(H_2O)_2(DEF)_2(btca)_8]$ with M=Co,Mn

To solve the structure of the first sample, stepwise 3D electron diffraction (3D ED) was collected on several nanocrystals. The 3D reconstruction of the reciprocal space (fig.1) can be indexed with a triclinic cell with parameters: *a=11.07(2)Å b=19.37(3)Å c=12.42(7)Å* and *α=84.47(0) β=101.22(8) γ=109.81(8)*.

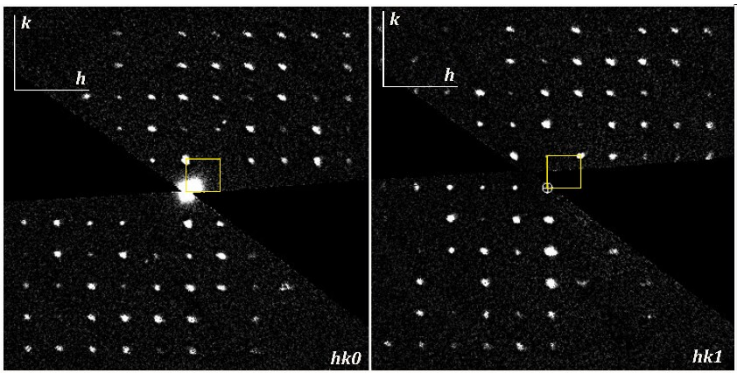

Fig.1: Sections of the reciprocal space of [Co\Mn(OH)$_2$(btca)$_2$] · DEF obtained from a 3D ED data collection. The black zones, devoid of reflections, are areas of the reciprocal space that are not integrated due to the mechanical limitations of the TEM.

From the study of the reciprocal space, no extinction rules were found, which indicates the absence of translation symmetry operations inside the unit cell, in agreement with the observed triclinic metric symmetry. The structure has been determinate with the program Superflip[25] which is part of the Jana2006[8] suite with a *P*-1 space group. The refinement of the structure against 3D ED data was carried out with the ShelxL[26] software, using the electronic atomic scattering. Moreover, the structural model was refined with Jana2006[8] against PXRD data collected in transmission geometry with a Copper source. The asymmetric unit of this structure consists of three metal sites and two btca molecules (fig.2).

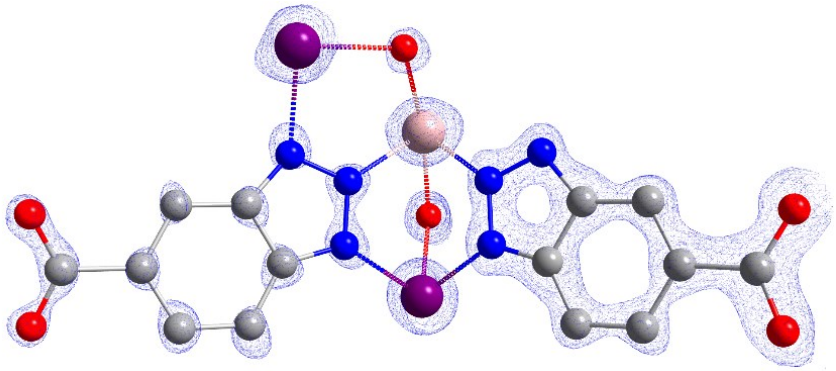

Fig. 2: Projections of the asymmetric unit with F_{obs} electrostatic potential map (blue area). The carbon in gray, the nitrogen in blue, the oxygen in red, the cobalt in purple and manganese in pink. The hydrogens have been hidden.

In particular, the two linker molecules, as seen in Figure 3, are arranged one along the direction ***a*** (btca-1, in blue) and the other along the direction ***b*** (btca-2, in red) with an angle between the two molecules of *109*°, this arrangement produces channels along the direction ***c*** the distance for two equivalent linkers are ≈10 *Å*.

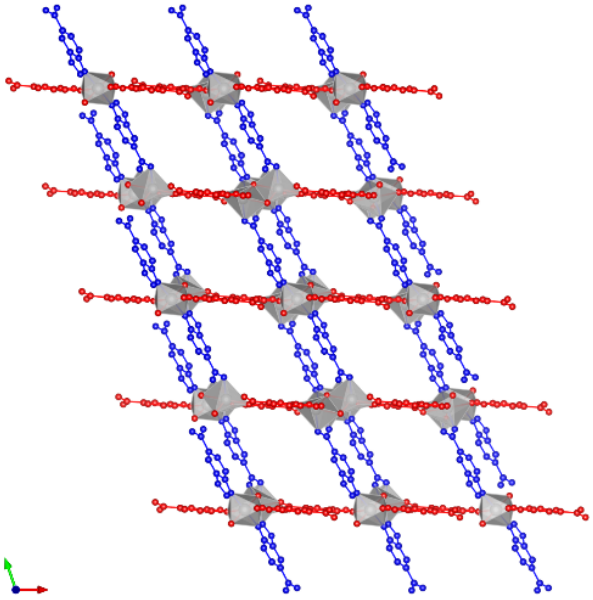

*Fig. 3: Projections of the framework along direction **c**, in red the btca along a direction and in blue the btca along the **b** direction.*

Due to the symmetry, the independent metal sites in the asymmetric unit are three but one is located on the inversion center. The application of inversion symmetry operation yields the complete formula $[M_{10}(OH)_4(H_2O)2(DEF)2(btca)_8]$. The data of the elemental chemical analyses (EDX) measure an equal quantity of the two metals, even if in the synthesis a double quantity of $Mn(NO_3)_2 \cdot 4H_2O$ with respect to $Co(NO_3)_2 \cdot 6H_2O$ was used. This represents a new crystal structure, never reported before. The XRD and 3D ED techniques are not able to perfectly distinguish the cations of Mn and Co, due to the similar atomic scattering amplitude. For graphic convenience we have assumed that the manganese atom is in the special position.

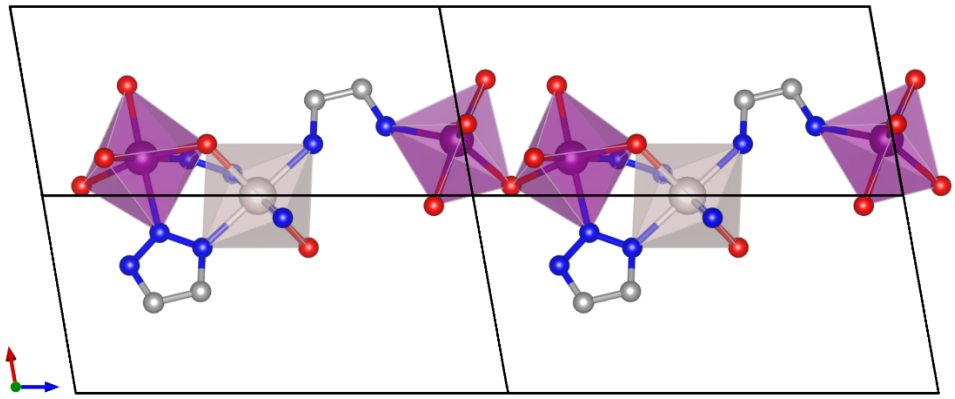

*Fig. 4: Projection of the metal sites in two cells along the **b** direction, with the carbon in gray, the nitrogen in blue, the oxygen in red, the M2 and M3 in purple and in M1 atom in special position in pink. The hydrogens have been hidden.*

One atom of cobalt *(M2)* and manganese *(M1)* have a *6*-fold coordination (distorted octahedra) while the other cobalt atom *(M3)* has a *5*-fold coordination arranged in a very distorted square. The two octahedra $M2N_2O_4$ and $M1N_4O_2$ share an equatorial oxygen *(O5)* instead the distorted $M3NO_4$ pyramid is connected to the first octahedron $M2O_6$ elonging to the next cell through a hydroxyl group *(-OH)* and to another square pyramid of another cell through another oxygen. The equatorial atoms that coordinate *M2* are three oxygens and one nitrogen, oxygen (*O1*) and nitrogen (*N2*) belong to the *btca-1* molecule (along direction ***a***) the remaining two oxygen are connecting the metal centers. The equatorial anions of the octahedron of $M1N_4O_2$ are also

two nitrogen of the *btca-1* molecule, and the rest are oxygen bridges between the metal centers. The apical anions of the two octahedra are one oxygen and one nitrogen for octahedron $M2N_2O_4$ and two nitrogen for octahedron $M1N_4O_2$ belong to *btca-2* (*btca* molecule oriented along ***b***). The third metal center consists of a cobalt atom in coordination with four oxygen atoms, one is provided by the carboxyl group of the *btca-1* molecule, the apex of the pyramid *(O3)* is provided by *btca*-2, one it is bridged with the metal center *M2*, the remaining atom is a nitrogen of the *btca-1* molecule.

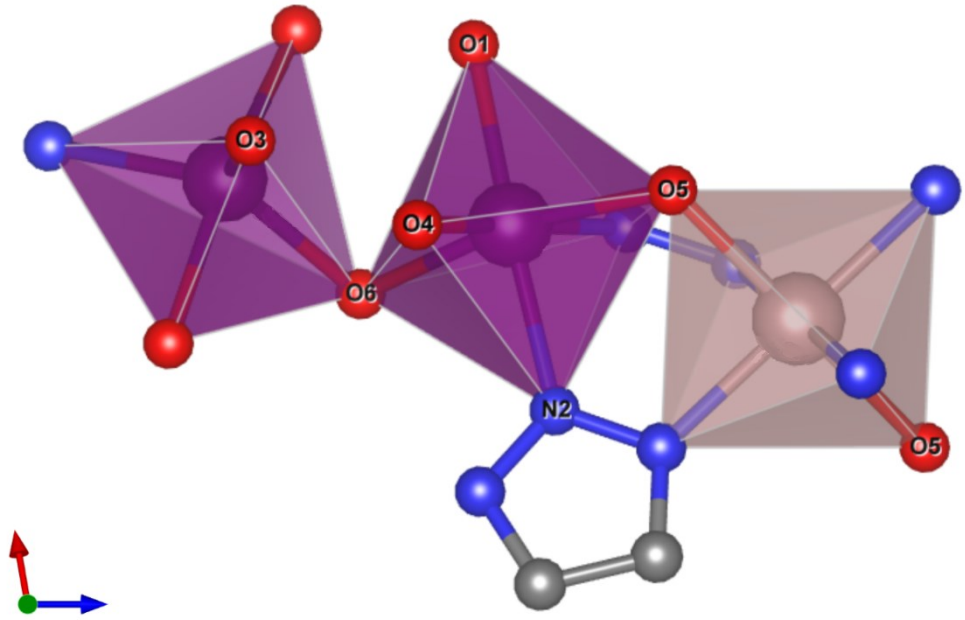

*Fig. 5: Projection of the three metal sites s along the **b** direction, with the carbon in gray, the nitrogen in blue, the oxygen in red, the cobalt in purple and in manganese in pink. The hydrogens have been hidden.*

Then the linker *btca-1*, (in blue) along ***a*** is completely deprotonated and coordinated with two nitrogen atoms, one atom is coordinated with the *M3* atom and the other with the *M2* an oxygen of its carboxyl group is instead coordinated with *M1*. Also, the linker *btca*-2 (in red) along ***b*** is completely deprotonated and is coordinated with two N atoms, one with *M1* and the other with *M2* and with both oxygens of the carboxyl group to the two cobalt atoms.

A disorder was observed and refined on the O5 site, the site is occupied for 47% by a water molecule and the remaining 53% is occupied by a DEF molecule to maintain the neutrality of the compound (Fig. 6).

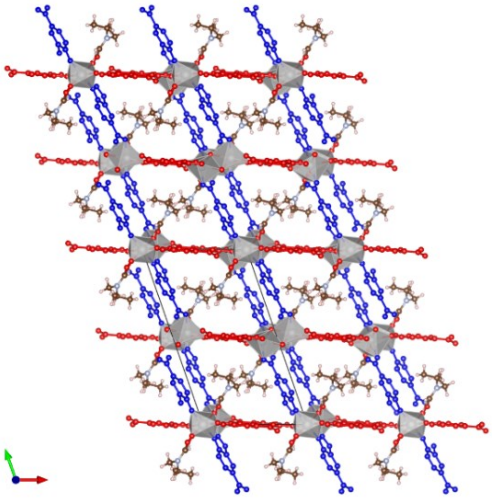

*Fig. 6: Projections of the framework along direction **c**, in red the btca along direction **a** and in blue the btca along direction **b** and DEF molecule inside the channels along **c** linked to the frameworks.*

This structure model has been refined not only on ED data with kinematic approximation but also on PXRD.

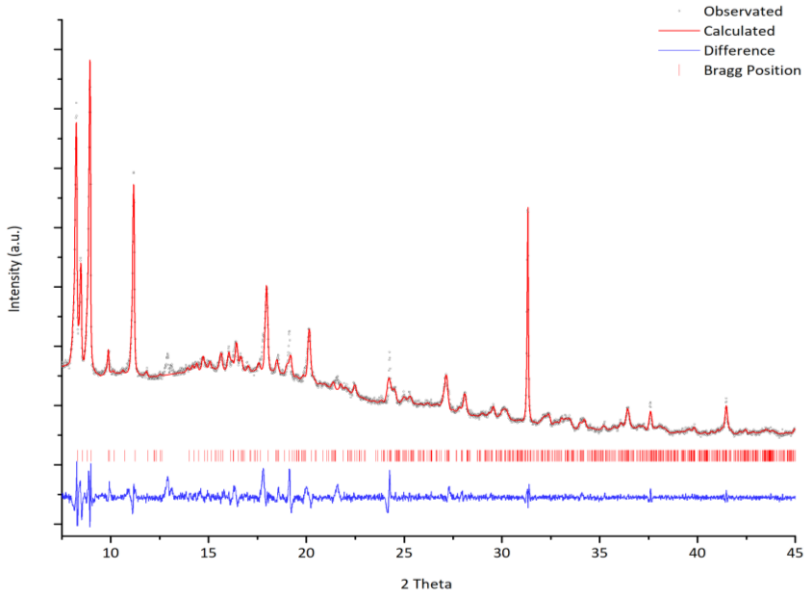

Fig.6: Plot of the Rietveld refinement of the P-1 structure of $[M_{10}(OH)_4(H_2O)_2(DEF)_2(btca)_8]$ against X-Ray diffraction data. Observed data (black point), calculated pattern (red line) and difference (blue line).

the refinement and structural parameters are summarized in table 1:

Table1.Structural parameters of the structure from the refinement of the X-ray and 3D ED data at room temperature.

Crystallographic information	
Asymmetric unit content	$Co_2MnC_{14}N_6O_5$
Z	4
Space group	*P*-1
Unit cell (from PXRD data)	
a (Å)	11.25(2)
b (Å)	18.97(6)
c (Å)	12.23(3)
α (deg)	84.56(9)
β (deg)	102.08(4)
γ (deg)	110.43(2)
Volume ($Å^3$)	2392.564

Structure solution parameters (SuperFlip on ED data)	
Data resolution (Å)	1.12
No. of sampled reflections	1298
No. of independent reflections	865
Global thermal factor U_{iso} (Å^2)	0.1093
$R_{int}(F)$ (%)	35.05
Structure refinement parameters (SHELXL on ED data)	
Data resolution (Å)	1.12
$R_{int}(F^2)$ (%)	33.15
No. of reflections (all)	2373
No. of reflections (>4σ)	1298
R1 (all) (%)	30.69
R1 (>4σ) (%)	26.81
Goodness-of-fit	1.078
Rietveld refinement parameters (on PXRD data)	
2θ range measured / step (°)	2.900 – 70.115 / 0.015
2θ range used (°)	7.000 – 70.115
Data resolution (Å)	1.5
No. of points	4202
R_{wp} (%)	2.50
Goodness-of-fit	1.530

6.1.4 Magnetic Properties

Magnetic measurements were made on this bimetallic MOF, performed with a MPMS XL SQUID magnetometer (Quantum Design). With parameters:

- Temperature range: 2-200 K.
- Magnetic field range: 0-5 T.

And for AC susceptibility measurements performed in the frequency range 1-1000 Hz, with an AC magnetic field of 4 Oe. These measurements were carried out on a sample quantity equal to 0.0218 g and it was assumed that the ratio between the metals of cobalt and manganese is 2:1. We began with studying the molar magnetization and magnetic susceptibility as a function of temperature, measuring at different magnetic fields, and simultaneously cooling the sample.

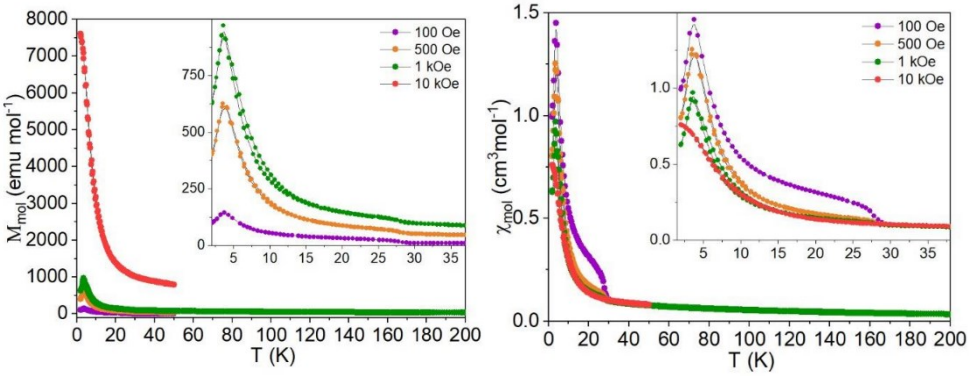

Fig. 7: Temperature dependence of the molar magnetization (a) and magnetic susceptibility (b) of MnCo-btca sample, measured on cooling at different applied magnetic fields. Insets: enlargement of the low-temperature region.

From these measures we can establish that the molar magnetization *M(T)* (Figure 6.a) and molar magnetic susceptibility *χ(T)* (Figure 6.b) show magnetic transitions. The molar magnetization and magnetic susceptibility show transition at about 28 K with an increase of magnetization by lowering temperature.

The magnetic arrangement at low temperature probably results from competing intra-chain ferromagnetic (FM) and antiferromagnetic (AFM) interactions between the Co and Mn ions in the "chain" configuration $\{Co_2Mn(OH)_2\}$ (through super-exchange coupling mediated by O atoms), which was already observed in other $\{Co_3(OH)_2\}$-based MOFs[27–31]. Instead, the weak inter-chains AFM interaction, mediated by the aromatic *btca* groups, is highlighted by the changes in the M(T) or χ(T) curves only at very low temperatures < 4 K. These two different metamagnetic transitions are probably due to the presence of some water molecules trapped in the sample or to the presence of the guest or both (In the following we will refer to H_2O molecules, but the same explanation could be based on the guest).[27] It has been established in studies on similar systems that the presence of H_2O molecules suppresses the weak AFM interaction between the chains and thus single-chain magnet like behavior is observed as a result of the large inter-chain. Therefore, we can try to give an explanation of these data, as a function of the crystalline structure of the sample:

- At about 28 K the chains of the framework undergo a magnetic transition to a magnetically ordered state with an overall ferrimagnetic-like character.

- The chains that are far from H_2O molecules organize themselves in an AFM state for T < 5 K, thanks to the weak inter-chain AFM coupling (the AFM transition is highlighted by the cusp in the χ(T) at low field). The cusp is more evident for H=500 Oe and 1 kOe, quite in agreement with data reported in bibliography[27].

- At this contribution is superimposed that of chains near H_2O molecules or guest. These molecules increase the interchain distances, thus suppressing the interchain AFM interaction and resulting in a single-chain ferrimagnetic behavior (at which corresponds the increase of M(T) and χ(T) for T < 5 K). At 5 K the interchain AFM coupling becomes not negligible also for the H_2O-chains, causing the decrease of the M(T) and χ(T) (Another possible explanation of the transition at 5 K is a change in the magnetic configuration inside the chains). Something similar was observed for a $Mn_3(btca)_2$-(HCOO)(μ_3-OH)$(H_2O)_2] \cdot 2DMF$[32], but no explanation are given.

This transition is more evident if the total magnetic susceptibility χT is plotted as a function of temperature, where a smaller variation in susceptibility is clearly seen by increasing the applied magnetic field. And if we plot the $1/\chi$ as a function of the temperature (T) we clearly see a linear behavior for a T > 28 K, which allows us to establish the presence of a paramagnetic behavior.

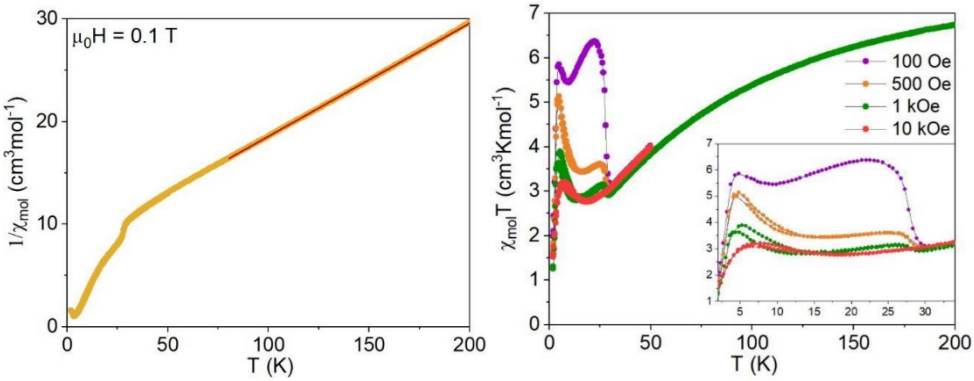

Fig. 8: (a) Inverse of the susceptibility measured at H=1 kOe. (b) Magnetic susceptibility plotted as χT vs T at different applied magnetic fields.

From a linear fit of the high-temperature 1/ χ(T) (T > 80K), we obtain the parameters C = 9.104 ± 0.005 cm^3Kmol^{-1}, θ= − 69.1 ± 0.1 K. The value of θ is larger than the corresponding values of the $Mn_3(btca)_2$-(HCOO)(μ_3-OH)(H_2O)$_2$]·2DMF[32] (θ = − 48.09, C = 11.47 cm^3Kmol^{-1}) and of the [Mn_3(L)(μ_3-OH)$_2$(H_2O)$_4$][29] (θ = − 59.6, C = 14.3 cm^3Kmol^{-1}).

Instead, it is lower than the θ reported for a Mn-btac MOF[33] (− 95 K). The average effective magnetic moment per magnetic ions is 4.9 μb, mainly due the larger moment of Mn^{2+} ion (S=5/2). At about 10 K it is evident that the magnetization starts to increase. Even the ac susceptibility (Figures 9 and 10) starts to increase at about 10 K.

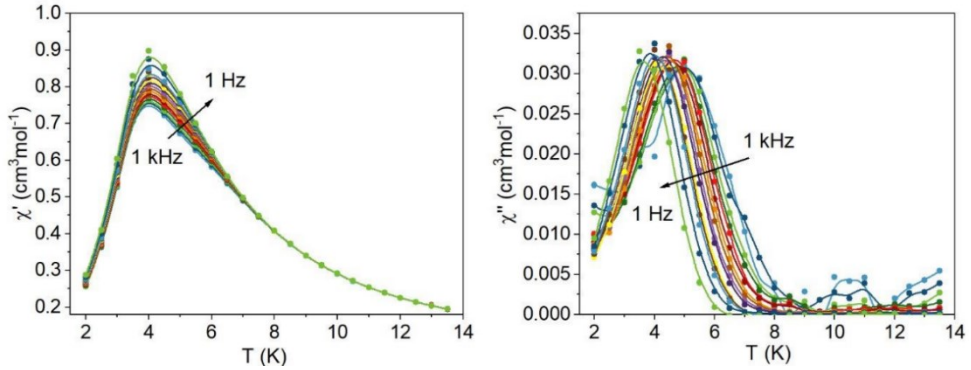

Fig. 9: Real (a) and imaginary (b) part of the AC magnetic susceptibility measured at low temperature at different frequencies with a driving AC field of 4 Oe under zero DC field.

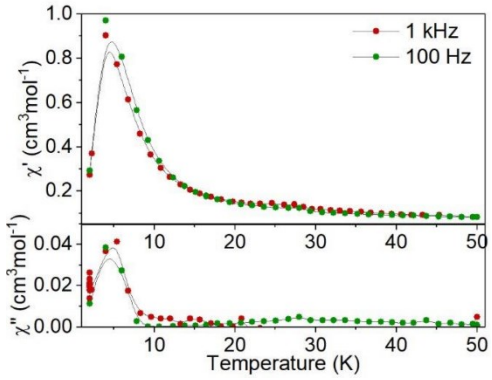

Fig. 10: Real and imaginary part of the AC magnetic susceptibility measured at 1 kHz and 100 Hz

The cusp around a temperature of 4 K suggests an AFM transition, probably due to the interchain AFM coupling. It disappears with an applied field of 10 kOe due to the weak interchain interaction.

This transition is highlighted also in the ac susceptibility measurements (Figure 9): the χ' shows a frequency-independent peak at which a very small χ'' signal is associated. The same behavior at about 4 K was observed in $Mn_5(btac)_4(\mu_3\text{-}OH)_2(EtOH)_2 \cdot DMF \cdot 3EtOH \cdot 3H_2O$[33] and $[Mn_3(L)(\mu_3\text{-}OH)_2(H_2O)_4]$[29]. The isothermal M(H) measurement (Figure 11), performed at 2 K, shows a behavior similar to that of Co-sample. The linear increase of magnetization at low applied field (H < 2 kOe) is related to the interchain AFM coupling. By increasing the field, the weak interchain AFM interaction becomes negligible and the single-chain ferrimagnetic behavior appears. A first sharp increase of magnetization is followed by a slow linear increase with the field, due to the canting of AFM coupled moments. If we subtract this linear behavior, we obtain a first "saturation" magnetization of about 1.26 μB.

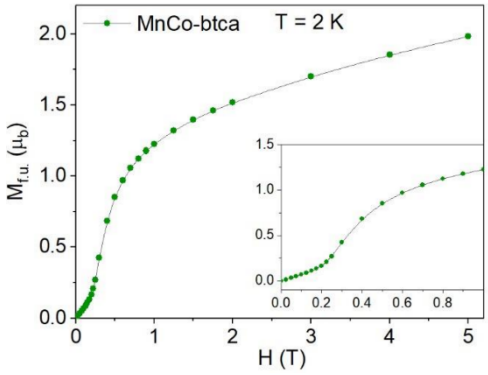

Fig. 11: Field-dependence of magnetization of the MnCo-btca sample measured at 2 K.

6.1.5 Synthesis $[M_3(OH)_2(btca)_2] \cdot (DMF)_2$ with M=Zn,Co

41 mg $Zn(NO_3)_2 \cdot 6H_2O$ and 38 mg $Co(NO_3)_2 \cdot 6H_2O$ were dissolved in 4.5 mL H_2O MilliQ and 23.1 mg H_2btca was dissolved in 8 ml dimethylformamide (DMF). The solutions were mixed, and the resulting clear solution was sealed in a 23 mL Teflon-lined Parr reaction vessel. The solution was heated to 150 °C during 1 hour, kept at this temperature for 3 hours and cooled down to RT for 3 hours. The reaction produced a pale beige suspension (which resulted to be amorphous) and a purple microcrystalline thin film deposited on the inner surface of the teflon cup. The purple product could be isolated easily from the suspension and was washed 3 times with clean DMF before being dried in the air for ED and PXRD analyses.

6.1.6 Structure of $[M_3(OH)_2(btca)_2] \cdot (DMF)_2$ with M=Zn,Co

To solve the structure of the second sample, stepwise 3D electron diffraction (3D-ED) was collected on several nanocrystals. From the indexing of the main reflections in the reconstructions of the reciprocal space, a monoclinic cell was found with cell parameters: *a=17.78(2)Å b=12.83(5)Å c=11.14(3)Å* e *β=93.79(6)°*.

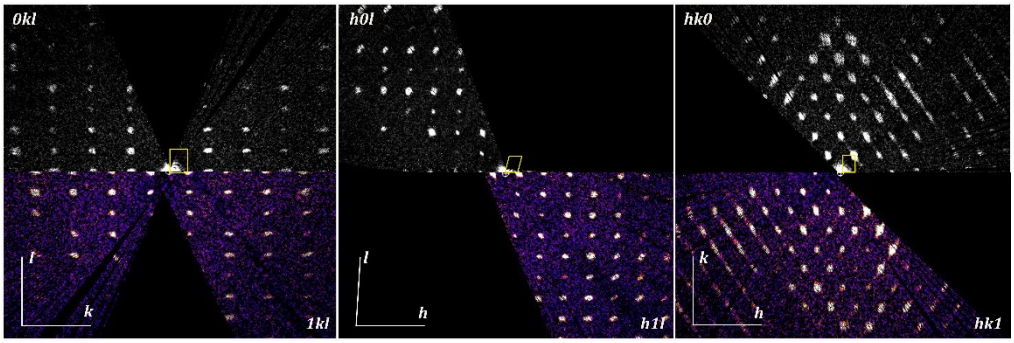

Fig.11: Sections of the reciprocal space of [Co\Zn(OH)$_2$(btca)$_2$] · DMF obtained from a 3D ED data collection. The black zones, devoid of reflections, are areas of the reciprocal space that are not integrated due to the mechanical limitations of the TEM.

From the study of the reconstructed reciprocal space sections (fig. 11) extinctions compatible with a C-centering (*h+k=2n* for *hkl* reflections) can be observed. Furthermore, in the plane *h0l* the rows with l odd are much weaker (almost invisible) suggesting the presence of a *c*-glide normal to *b*. For these reasons we tentatively assigned as possible space groups *C2/c* and *Cc*. The structure was determinate with 3D ED data and the centrosymmetric space group *C2/c* using the superflip[1] algorithms part of Jana2006[2] suite. For the refinement the software ShelxL[7,8] was used. In addition, the structural model was refined against PXRD data collected in transmission geometry with a copper source. The asymmetric unit of this MOF consists of two metal sites and a *btca* molecule (Fig. 12).

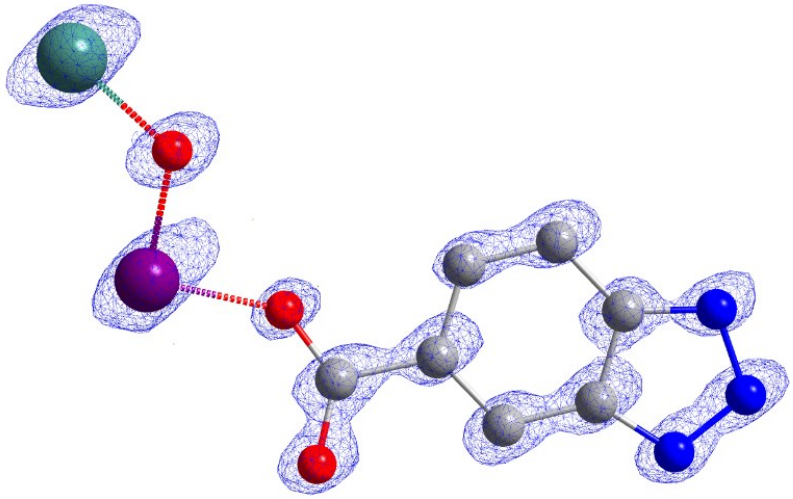

Fig.12: Projections of the asymmetric unit with electrostatic potential (blue area). The carbon in gray, the nitrogen in blue, the oxygen in red, the metal center one (M1) in purple and metal center two (M2) in green. The hydrogens have been hidden.

From the data of the elementary analyzes (EDX) carried out on different crystals, a greater quantity of *Zn* than *Co* is measured even if the independent metal sites are two. Since the electron diffraction data and the X-ray diffraction data are unable to distinguish the two cations inside the asymmetric unit (fig.13) we could not determine if there is a cation ordering on the two metal sites, identified in the following as *M1* and *M2*.

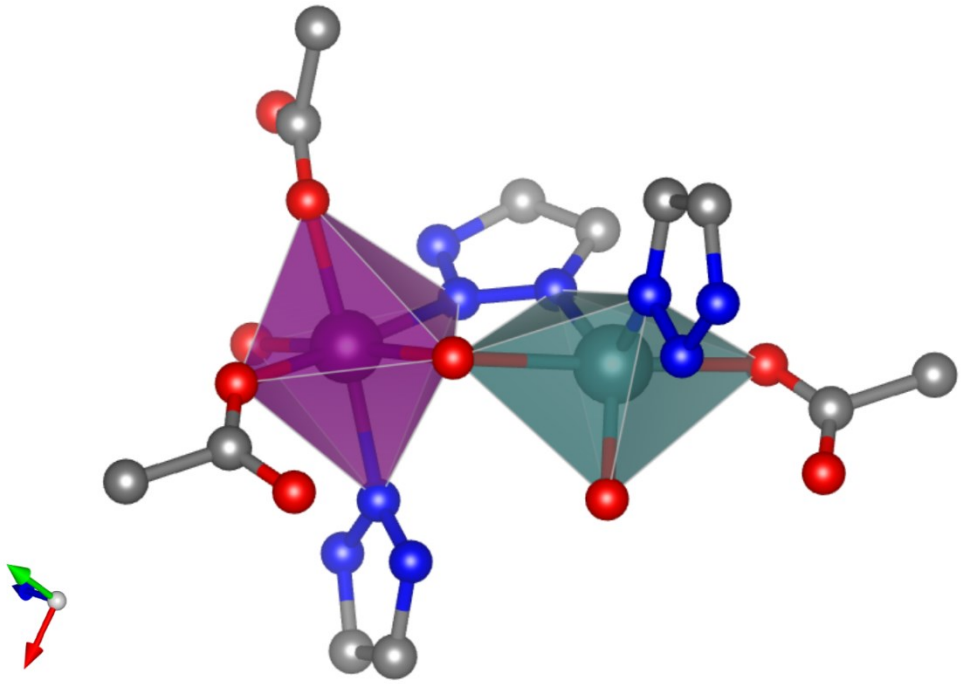

Fig. 13: Projection of the metal sites, with the carbon in gray, the nitrogen in blue, the oxygen in red, the metal center one (M1) in purple and metal center two (M2) in green. The hydrogens have been hidden.

The two metal sites have two different coordination, the metal one has a *6*-fold coordination (distorted octahedra), while metal two has a *5*-fold coordination (distorted square pyramid). The $M1N_2O_4$ octahedra have an oxygen (O3) and a nitrogen as apical atoms and one nitrogen and three oxygen as equatorial anions. The base of the square pyramid $M2N_2O_3$ is formed by three oxygens and two nitrogen, one oxygen (O1) is shared with the *M1* octahedra while the remaining anions including the apical nitrogen are provided by the organic linker.

The resulting framework of this MOF is shown Figure 14:

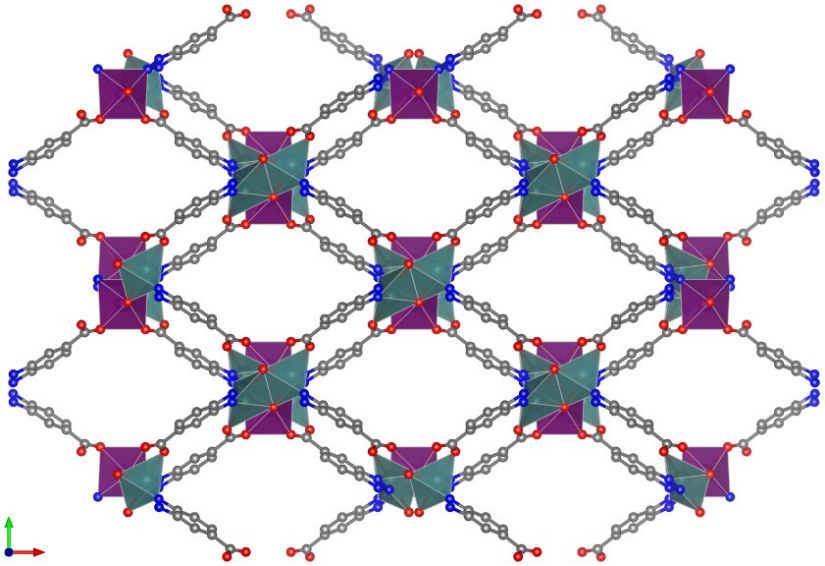

Fig. 14: Projections of the framework along direction c, in green the octahedra of M2 in purple the octahedra of M1, in red oxygen, blue nitrogen and gray carbon.

Difference Fourier analysis on 3D ED data revels the presence of a guest molecule inside the channels. The guest can be identified as a DMF molecule the solvent used for *btca* in the synthesis of this MOF (figure 15).

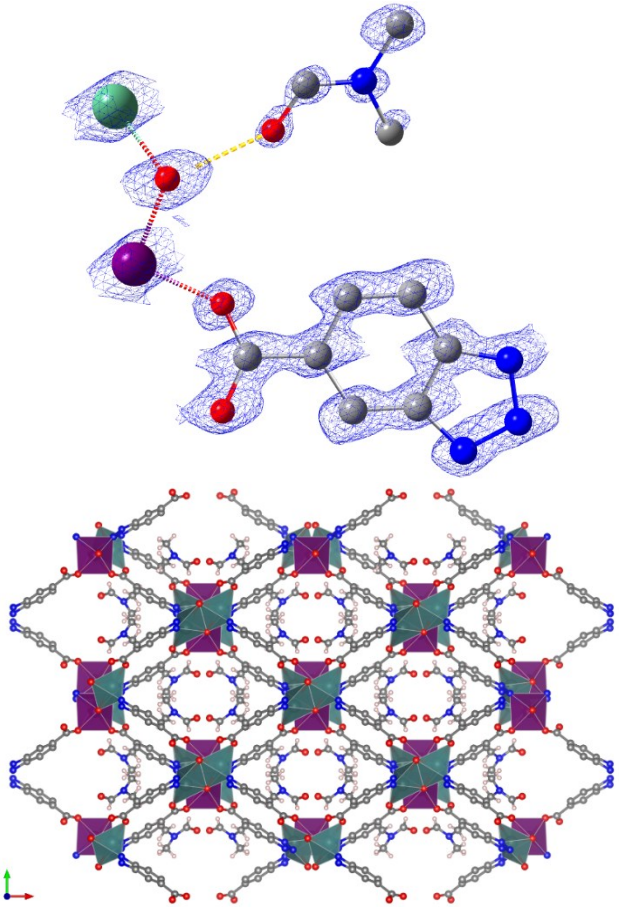

Fig.15: Top: Projections of the asymmetric unit and DMF coordinate with electrostatic potential (blue area). The carbon in gray, the nitrogen in blue, the oxygen in red, the metal center one (M1) in purple and metal center two (M2) in green. The hydrogens have been hidden. Bottom: Projections of the framework along the c direction.

This structure model has been refined not only on electronic diffraction data but also on X-ray data with copper source in Debye-Scherrer mode. This crystal structure is isostructural to the MOF synthesized by Xiao, Juan et al.[36]

but which has only one metal as a bridge between organic molecules unlike our compound which has two.

This structure model has been refined not only on ED data with kinematic approximation but also on PXRD.

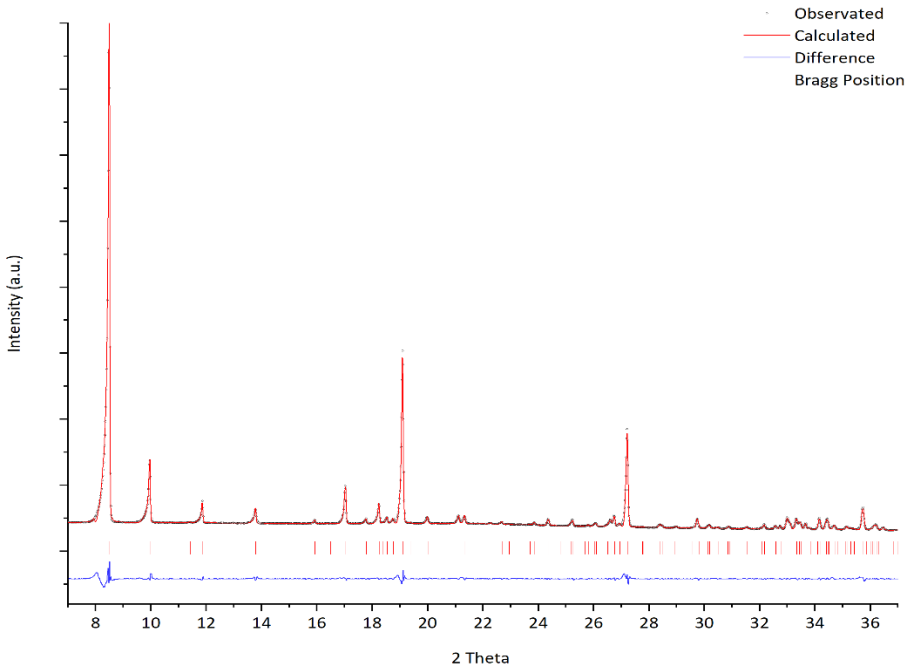

Fig.16: Plot of the Rietveld refinement of the C2/c structure of $[M_3(OH)_2(btca)_2] \cdot (DMF)$ against X-Ray diffraction data. Observed data (black point), calculated pattern (red line) and difference (blue line).

The refinement and structural parameters are summarized in table 1.

Table1: Structural parameters of the structure from the refinement of the X-ray and 3D ED data at room temperature.

Crystallographic information	
Asymmetric unit content	$ZnCoC_{10}N_4O_3$
Z	4
Space group	*C2/c*
Unit cell (from PXRD data)	
a (Å)	17.78(2)
b (Å)	12.83(6)
c (Å)	11.14(3)
α (deg)	90
β (deg)	93.79(6)
γ (deg)	90
Volume (Å^3)	2537.80
Structure solution parameters (SuperFlip on ED data)	
Data resolution (Å)	1.12
No. of sampled reflections	3340
No. of independent reflection	1603
Global thermal factor U_{iso} (Å^2)	0.2667
$R_{int}(F)$ (%)	45.03
Structure refinement parameters (SHELXL on ED data)	
Data resolution (Å)	1.12
$R_{int}(F^2)$ (%)	33.15
No. of reflections (all)	2373
No. of reflections (>4σ)	1298
R1 (all) (%)	26.81
R1 (>4σ) (%)	30.69
Goodness-of-fit	1.078
Rietveld refinement parameters (on PXRD data)	
2θ range measured / step (°)	*7.000 – 69.685 / 0.015*
2θ range used (°)	7.000 – 60.000
Data resolution (Å)	1.53
No. of points	3527
R_{wp} (%)	1.15
Goodness-of-fit	2.86

6.2 References

1. Gemmi, M. & Lanza, A. E. 3D electron diffraction techniques. *Acta Crystallographica Section B: Structural Science, Crystal Engineering and Materials* **75**, 495–504 (2019).

2. Mugnaioli, E. *et al.* Ab initio structure determination of vaterite by automated electron diffraction. *Angewandte Chemie - International Edition* **51**, 7041–7045 (2012).

3. Steciuk, G., Palatinus, L., Rohlíček, J., Ouhenia, S. & Chateigner, D. Stacking sequence variations in vaterite resolved by precession electron diffraction tomography using a unified superspace model. *Scientific Reports* **9**, (2019).

4. Nederlof, I., van Genderen, E., Li, Y. W. & Abrahams, J. P. A Medipix quantum area detector allows rotation electron diffraction data collection from submicrometre three-dimensional protein crystals. *Acta Crystallographica Section D: Biological Crystallography* **69**, 1223–1230 (2013).

5. Vincent, R. & Midgley, P. A. Double conical beam-rocking system for measurement of integrated electron diffraction intensities. *Ultramicroscopy* **53**, 271–282 (1994).

6. Petříček, V., Dušek, M. & Palatinus, L. Crystallographic Computing System JANA2006: General features. *Zeitschrift für Kristallographie - Crystalline Materials* **229**, 345–352 (2014).

7. Palatinus, L. & Chapuis, G. SUPERFLIP - A computer program for the solution of crystal structures by charge flipping in arbitrary dimensions. *Journal of Applied Crystallography* **40**, 786–790 (2007).

8. Sheldrick, G. M. Crystal structure refinement with SHELXL. *Acta Crystallographica Section C: Structural Chemistry* **71**, 3–8 (2015).

9. Zhang, X.-M., Hao, Z.-M., Zhang, W.-X. & Chen, X.-M. Dehydration-Induced Conversion from a Single-Chain Magnet into a Metamagnet in a Homometallic Nanoporous Metal–Organic Framework. *Angewandte Chemie International Edition* **46**, 3456–3459 (2007).

10. Yang, F. *et al.* Two Metal–Organic Frameworks Constructed from One-Dimensional Cobalt(II) Ferrimagnetic Chains with Alternating Antiferromagnetic/Ferromagnetic and AF/AF/FM Interaction: Synthesis, Structures, and Magnetic Properties. *Inorganic Chemistry* **51**, 6813–6820 (2012).

11. YL Wu *et al.* Two Isostructural Metal–Organic Frameworks Directed by the Different Center Metal Ions, Exhibiting the Ferrimagnetic Behavior and Slow Magnetic Relaxation. *Inorganic Chemistry*. (2016)

12. Xiao-Ju Li, Xin-Yi Wang, Song Gao, Rong Cao. Two Three-Dimensional Metal−Organic Frameworks Containing One-Dimensional Hydroxyl/Carboxylate Mixed Bridged Metal Chains: Syntheses, Crystal Structures, and Magnetic Properties. *Inorganic Chemistry* **45**, 1508–1516 (2006).

13. Carine Livage *et al.* Effect of Mixing of Metal Cations on the Topology of Metal Oxide Networks. *Angewandte Chemie* (2007)

14. Liu, J. *et al.* Coexistence of long-range ferromagnetic ordering and spin-glass behavior observed in the first inorganic–organic hybrid 1-D oxalate-bridging nona-MnII sandwiched tungstoantimonate chain. *Journal of Materials Chemistry C* **5**, 2043–2055 (2017).

15. Han, Z.-B. *et al.* Mn(II)-Based Porous Metal−Organic Framework Showing Metamagnetic Properties and High Hydrogen Adsorption at Low Pressure. *Inorg. Chem* **51**, 679 (2012).

16. Petrícek, V., Dušek, M. & Palatinus, L. Crystallographic computing system JANA2006: General features. *Zeitschrift fur Kristallographie* 345–352 (2014).

17. Thorn, A. & Sheldrick, G. M. Extending molecular-replacement solutions with SHELXE. *Acta Crystallographica Section D: Biological Crystallography* **69**, 2251–2256 (2013).

18. Xiao, J. *et al.* Crystalline structural intermediates of a breathing metal-organic framework that functions as a luminescent sensor and gas reservoir. *Chemistry - A European Journal* **19**, 1891–1895 (2013).

7. Conclusion and Outlook

In this thesis it has been demonstrated that 3D electron diffraction and its development in the last decade has led to a reliable diffraction technique that is suitable for the resolution of crystalline structures of different nature. As we have illustrated in previous chapters, this new technique and its developments are able not only to resolve crystalline structures but allow us to know details and/or defects thanks to its great resolution. In the case of the inorganic phase $NaLaCoWO_6$ it was possible to completely resolve the incommensurate modulated structure by the definition of the modulation vector and of the supersymmetry, extrapolated from the 3D-ED data. We were able to demonstrate and solve the order of tilt of the octahedra thanks to the application and knowledge of the theory of superspace. This approach is a powerful tool for the investigation of complex structures in materials science, and is fruitfully applied to different materials, giving important elements for scientific discussion. Furthermore, this study allowed to unequivocally define that the modulation present in this material has a displacive nature rather than compositional as hypothesized in literature. The complex structural distortions likely generate electric polarization which couples with the magnetic ordering at low temperature giving rise to a new form of multiferroism. The resolution of both the average structure and the modulated structures of the $Na_{1\pm x}La_{1\pm x}MgWO_6$ series shows that standard crystallographic investigations and morphological analyzes alone can lead to misleading results. In fact, we have shown that the modulation of this phase is not linked to a difference of local composition but by a different octahedral tilting pathway featuring the crystalline structure. Such structural results were achieved by the use of the 3D ED technique.

The robustness and flexibility of the 3D-ED was also demonstrated in the resolution of the two metal-organic structures, for which both the frameworks and the molecules within the channels were defined. The knowledge of the crystal structures allowed us the detailed study of the magnetic characteristics. In fact, having determinated the bi-metallic MOF's structures, the SQUID measurements were explained by defining the magnetic

interactions occurring in the framework. In this case, in addition to the definition of the crystalline structure and magnetic characteristics, we also demonstrated the goodness of our method for the synthesis of bimetallic MOFs. This could pave the way for a new generation of MOFs in which absorption characteristics can be combined with the response to external mechanical or magnetic stimuli. By concluding 3D-ED allowed to disclose complex crystallographic problems. We demonstrated the robustness and reliability of the 3D-ED technique, and we opened the way to a new generation of materials, providing a reliable and eco-sustainable synthesis method. The 3D-ED is an innovative technique able to satisfy the growing requests for crystallographic analysis on nanomaterials. The main experimental drawbacks that still affecting this technique can be solved with the increase of academic and private interest in this revolutionary application. In fact, several private companies such as Rikagu or Eldico Scientific are working to create an instrument that solves the problems related to the mechanical part of the transmission electron microscope. In particular, Rikagu in collaboration with JOEL in the last year has developed the first electron diffractometer which is able to solve the instability of the goniometer and make the collection of 3D-ED data reliable and reproducible.